

High Frequency Effects of Impedances and Coatings in the CLIC Damping Rings

THÈSE N° 6661 (2015)

PRÉSENTÉE LE 25 SEPTEMBRE 2015
À LA FACULTÉ DES SCIENCES DE BASE
LABORATOIRE DE PHYSIQUE DES ACCÉLÉRATEURS DE PARTICULES
PROGRAMME DOCTORAL EN PHYSIQUE

ÉCOLE POLYTECHNIQUE FÉDÉRALE DE LAUSANNE

POUR L'OBTENTION DU GRADE DE DOCTEUR ÈS SCIENCES

PAR

Eirini KOUKOVINI PLATIA

acceptée sur proposition du jury:

Prof. V. Savona, président du jury
Prof. L. Rivkin, Dr G. Rumolo, directeurs de thèse
Dr R. Nagaoka, rapporteur
Dr S. Calatroni, rapporteur
Dr M. Dehler, rapporteur



ÉCOLE POLYTECHNIQUE
FÉDÉRALE DE LAUSANNE

Suisse
2015

A command within me: "Dig! What do you see?"
"Men and birds, water and stones!"
"Dig deeper! What do you see?"
"Ideas and dreams, lightnings and ghosts."
"Dig deeper! What do you see?"
"I see nothing! A mute night, as thick as death. It must be death."
"Dig deeper!"
"Ah! I cannot penetrate the dark partition wall! Voices and weeping, flutter of wings on the
other shore!"
"Don't cry! Don't cry! They are not on the other shore! The voices, the weeping and the wings
are your own heart."
— Nikos Kazantzakis

To my family and friends

Acknowledgments

I feel extremely lucky to have done my PhD at CERN and EPFL, collaborating with an amazing team. I would like to express my deepest gratitude to my CERN supervisor, Giovanni Rumolo, for introducing me to and traveling with me in the fascinating field of accelerator physics and collective effects. Thank you for your support all these years, for always finding time for my questions and brainstorming, for giving me opportunities and for making these years such an enjoyable experience.

I would also like to deeply thank my university supervisor, Prof. Leonid Rivkin, for his continuous support, his monitoring and important advice over the PhD progress and for the great experience of tutoring with him at EPFL. I would also like to particularly thank Yannis Papaphilippou for all his support throughout the years, his great advice and for making the Low Emittance Rings community feel like a family.

I feel indebted to Carlo Zannini for his help and important contribution to this work. It has been a lot of fun collaborating with him. Making interesting discussions and observations as well as creating new words was almost a daily routine. I cannot thank you enough for your support and friendship.

I would also like to thank my colleagues Benoit Salvant, Kevin Li, Nicolas Mounet, Nicolo Biancacci and Giovanni De Michele for their help whenever it was needed, for sharing so willingly their knowledge and time during my first steps (and not only). It was a pleasure to work with them.

I am grateful to my section leader Roberto Corsini for always supporting my ideas and projects, as well as, Elias Métral and the HSC group colleagues for several useful discussions.

All the studies and results presented in this dissertation on the material characterization, would not have been possible without the expertise and help of our colleagues in the TE/VSC group, Mauro Taborelli, Pedro Costa Pinto, Wil Vollenberg and Paul Garritty. I had also fruitful discussions with Sergio Calatroni. I would like to thank Marina Malabaila, Ana Teresa Perez Fontenla and Floriane Leaux for the material profile analysis. I wish to thank Alex Arsenovic and Jeffrey Hesler from Virginia Diodes for the excellent collaboration. I would also like to express my gratitude to Alexej Grudiev for numerous helpful discussions.

Special thanks to our ALBA colleagues, Ubaldo Iriso and Thomas Günzel, for the very interesting and fruitful collaboration. It was a great experience for me to participate in a set of measurements in the light synchrotron. I am also thankful to the SLS colleagues, Andreas Streun, Masamitsu Aiba and Micha Dehler for the interesting work on SLS and SLS2 upgrade. Last but not least, I am grateful and lucky for all the interesting people I have met those

Acknowledgments

years, colleagues and more than that, friends: my office mates Yngve Levinsen (a Python problem-solver) and Serena Persichelli, Hannes Bartosik, Gianni Iadarola, my good friends Christos Lazaridis, Fanouria Antoniou, Stefania Papadopoulou, Leuteris Fadakis, Alessandro Danisi, Panos Zisopoulos and Andriy Nosych. Thanks a million to my friend Nadia, for her sincere friendship, for dragging me out of the physics world when necessary and for all the fun moments we shared together. There are no words to thank enough for the love and continuous support of my family, my parents and my brother Yannis. Without them, none of this would have been possible.

Lausanne, April 2015

E. K. P.

Abstract

The Compact Linear Collider (CLIC) is a 3 TeV e^+e^- machine, currently under design at CERN, that targets to explore the terascale particle physics regime. The experiment requires a high luminosity of $2 \times 10^{34} \text{ cm}^2 \text{ s}^{-1}$, which can be achieved with ultra low emittances delivered from the Damping Rings (DRs) complex. The high bunch brightness of the DRs gives rise to several collective effects that can limit the machine performance.

Impedance studies during the design stage of the DR are of great importance to ensure safe operation under nominal parameters. As a first step, the transverse impedance model of the DR is built, accounting for the whole machine. Beam dynamics simulations are performed with HEADTAIL to investigate the effect on beam dynamics. For the correct impedance modeling of the machine elements, knowledge of the material properties is essential up to hundreds of GHz, where the bunch spectrum extends. Specifically, Non Evaporable Getter (NEG) is a commonly used coating for good vacuum but its properties up to high frequencies were still widely unexplored. A new method using rectangular waveguides is proposed, benchmarked and applied for the first time to characterize NEG up to hundreds of GHz.

The numerical tools used for the DR studies are applied and benchmarked with measurements in other light sources. In particular, single bunch measurements were performed in the ALBA light source and compared to the model prediction using HEADTAIL. The impedance budget of ALBA was estimated before and after the installation of a pinger magnet. Furthermore, studies were also carried out for the Swiss Light Source (SLS) upgrade to investigate the machine performance in terms of single bunch instabilities for lattices with negative momentum compaction factor.

Key words: ALBA, CLIC, CST Particle Studio, collective effects, damping rings, dipolar/quadrupolar impedance, HEADTAIL macro-particle simulations, head-tail modes, NEG, single-bunch instabilities, impedance budget, SLS, TMCI, wake field, waveguides

Résumé

Le projet de Collisionneur linéaire compact (CLIC - Compact Linear Collider), actuellement en cours de conception au CERN, est un collisionneur e^+e^- à une énergie de 3 TeV, visant à explorer la physique des particules aux ultra-hautes énergies. L'expérience requiert une haute luminosité, de $2 \times 10^{34} \text{ cm}^2 \text{ s}^{-1}$, rendue possible par les émittances très basses atteintes dans les anneaux d'amortissement (DR - Damping rings). Cependant, la haute brillance dans les DR donne lieu à des effets collectifs pouvant limiter la performance de la machine.

Les études d'impédance conduites durant la phase de conception des DR, sont d'une importance critique pour assurer une opération nominale sécurisée de la machine. Tout d'abord, un modèle d'impédance transverse du DR dans sa globalité est construit. L'impact de l'impédance sur le faisceau est ensuite évalué par le biais du logiciel HEADTAIL. La connaissance des propriétés des matériaux est essentielle pour une modélisation correcte des éléments de la machine à des fréquences allant jusqu'au GHz, fréquence jusqu'où s'étend le spectre des paquets. En particulier, l'absorbant non évaporable (NEG - Non Evaporable Getter) est un matériau de revêtement en couche mince utilisé pour atteindre des vides très poussés, mais ses propriétés électromagnétiques à haute fréquence sont encore très peu connues. Une méthode nouvelle, faisant usage de guides d'ondes rectangulaires, est proposée, validée et appliquée pour la première fois à la caractérisation du NEG à des fréquences allant jusqu'à des centaines de GHz.

Les outils numériques utilisés pour ces études ont été appliqués et comparés aux résultats de mesures faites dans d'autres synchrotrons. En particulier, des mesures avec un seul paquet ont été réalisées à la source de lumière ALBA et comparées aux prédictions du modèle dans HEADTAIL. Le budget d'impédance d'ALBA a été estimé avant et après l'installation d'un aimant *pinger*. En outre, une étude a été conduite pour analyser les instabilités des paquets individuels dans le cadre de l'amélioration SLS2 de la Swiss Light Source.

Mots clefs : ALBA, anneaux d'amortissement, budget d'impédance, champ de sillage, CLIC, CST Particle Studio, effets collectifs, impédance, instabilités d'un seul paquet, modes head-tail, NEG, simulations HEADTAIL, SLS, TMCI, guides d'ondes

Contents

Acknowledgments	v
Abstract	vii
List of figures	xviii
List of tables	xix
1 Introduction	1
1.1 Physics prospects for a future Linear Collider	1
1.2 CLIC overview	2
1.3 The CLIC Damping Rings	4
1.4 Scope of the thesis	6
2 Beam dynamics and collective effects	7
2.1 Linear beam optics	7
2.1.1 Transverse betatron motion	8
2.1.2 Longitudinal synchrotron motion	13
2.2 Synchrotron radiation damping and quantum excitation	14
2.3 Wake fields and impedances	16
2.3.1 Longitudinal plane	18
2.3.2 Transverse plane	19
2.3.3 Effective impedance	20
2.4 Electromagnetic simulation tools of wakefields and impedances	21
2.4.1 CST Studio Suite	21
2.4.2 ImpedanceWake2D	21
3 Transverse impedance budget of the CLIC DR	23
3.1 Introduction	23
3.2 The HEADTAIL code	24
3.3 Transverse impedance budget	25
3.3.1 Impedance model with a broad-band resonator	25
3.3.2 Impedance model with a broad-band resonator and resistive wall	31
3.4 Effect of coating thickness and properties at high frequencies	37
3.5 Injection and extraction kickers	40

Contents

4	Electromagnetic properties of NEG at high frequencies	43
4.1	Motivation	43
4.2	Waveguide method and CST simulation	43
4.2.1	Method	43
4.2.2	Benchmark with known materials	45
4.2.3	S parameters	46
4.2.4	Network analyzer	47
4.3	Measurements with a stainless steel waveguide in X-band	47
4.4	Measurements with a copper waveguide in X-band	51
4.5	Measurements of NEG on a copper waveguide in X-band	54
4.5.1	NEG coating process	54
4.5.2	NEG-coated Cu waveguide measurement results	54
4.5.3	Error analysis for CST simulations	57
4.5.4	Conclusions about the NEG conductivity in X-band	63
4.6	NEG properties characterization above 200 GHz	64
4.6.1	220-330 GHz: WR-3.4 waveguides	64
4.6.2	500-750 GHz: WR-1.5 waveguides	70
4.7	Effect of the non-uniform coating profile	73
4.8	Effect on the transverse impedance budget of the DRs	80
5	Studies on existing and future light sources	83
5.1	Single bunch measurements in the ALBA storage ring	83
5.1.1	TMCI measurements at 0 chromaticity and HEADTAIL simulations	84
5.1.2	Study of the injection kickers	90
5.1.3	TMCI measurements at 0 chromaticity to study the effect of the pinger magnet	98
5.2	Impedance studies for the SLS2 upgrade	101
5.2.1	Motivation	101
5.2.2	Transverse resistive wall impedance and instability thresholds at zero chromaticity	102
5.2.3	Transverse resistive wall impedance and instability thresholds at positive and negative chromaticity	103
5.2.4	Comparative study with higher negative momentum compaction factor lattice (ca05q)	109
5.2.5	Transverse resistive wall impedance and instability thresholds at zero chromaticity for the ca05q lattice	109
	Conclusions	113
A	HEADTAIL simulations parameters for the CLIC DR	115
A.1	Broad-band resonator model with 0 chromaticity	115
A.2	Broad-band resonator model with positive chromaticity	117

B ImpedanceWake2D parameters	119
B.1 Wigglers: 2 μm NEG coating on StSt chamber	119
B.2 Arcs: 2 μm NEG coating on StSt chamber	120
B.3 Rest: 2 μm NEG coating on StSt chamber	120
B.4 Wigglers: 1 μm or 2 μm NEG coating on StSt chamber	121
B.5 Wigglers: 0.5 μm or 1 μm aC coating on StSt chamber	122
C CST and ImpedanceWake2D comparison	123
C.1 Compare coating feature for a lossy substrate	123
D Simulations parameters for SLS2	124
D.1 Resistive wall impedance calculation of SLS2 with ImpedanceWake2D	124
Curriculum Vitae	131

List of Figures

1.1	CLIC layout	3
1.2	DRs layout	5
1.3	Modern light sources emittances target	5
2.1	Frenet-Serret coordinate system	8
2.2	Elliptical trajectory in the horizontal phase space of a particle at location s . . .	11
2.3	CST model for the ALBA kicker	17
2.4	Transverse fields in the kicker	17
2.5	Source (q_1) and test (q) particles in an accelerator component with an arbitrary geometry.	18
3.1	Coherent horizontal motion with a BBR and 0 chromaticity	27
3.2	Coherent vertical motion with a BBR and 0 chromaticity	28
3.3	Mode spectrum for 0 chromaticity and a BBR	28
3.4	Mode spectrum for positive and negative chromaticity for a BBR	29
3.5	Rise time in x and y plane for positive chromaticity	30
3.6	Optics functions of the CLIC DR	32
3.7	Damping ring layout	33
3.8	Wake function model of the EDR	34
3.9	Mode spectrum for 0 chromaticity, a BBR and RRW contribution	34
3.10	Mode spectrum for positive chromaticity, a BBR and RRW contribution	35
3.11	Rise time in x and y plane for positive chromaticity for BB and RRW	35
3.12	Wake function model of the PDR	36
3.13	TMCI thresholds for the positron damping rings	37
3.14	Thresholds for the positron damping rings with positive chromaticity	37
3.15	Generalized vertical impedance of the wigglers for various coating thicknesses and materials	38
3.16	Generalized vertical impedance of the wigglers for NEG or aC of various thicknesses and materials	38
3.17	Imaginary vertical impedance for aC coating of 0.5 or 1 μm thickness	39
3.18	Imaginary vertical impedance for 2 μm NEG coating for different conductivities	39
3.19	CLIC stripline kicker prototype	41
3.20	Simplified kicker 3D model with CST	41

List of Figures

3.21 CST convergence study on the number of lines per wavelength	42
4.1 S_{21} for StSt and Cu waveguide	44
4.2 S_{21} for various conductivities with CST. Intersection with measured data.	45
4.3 Experimental setup for VNA measurements	46
4.4 Scattering parameters	47
4.5 X-band StSt waveguide	48
4.6 S_{21} for a StSt waveguide: experiment (blue) and CST simulation (magenta) comparison.	49
4.7 3D model of a rectangular X-band StSt waveguide	49
4.8 Roughness measurement on a StSt waveguide	50
4.9 Extracted conductivity of StSt from measurements and CST simulations for a waveguide with smooth surface. The expected DC conductivity for this type of StSt is added for reference (blue).	51
4.10 S_{21} for Cu	52
4.11 Effective conductivity of Cu as extrapolated from waveguide measurements and CST simulations for a waveguide with smooth surface.	52
4.12 Roughness measurements on a Cu waveguide	53
4.13 NEG coating	54
4.14 S_{21} measurements for NEG-coated waveguide	55
4.15 Example of intersection of simulated S_{21} with the measured value	55
4.16 Effective conductivity of NEG	56
4.17 S_{21} results obtained from CST MWS for different values of NEG thickness in μm	57
4.18 Comparison of CST S_{21} results for 100 μm NEG-coated waveguide and a bulk waveguide with NEG properties	58
4.19 NEG layer profile with XRF	58
4.20 NEG thickness profile with SEM	59
4.21 SEM	59
4.22 Comparison of SEM and XRF	59
4.23 S_{21} for different NEG coating thickness	60
4.24 SOLT and TRL calibration	61
4.25 Intersection of simulated S_{21} as a function of conductivity with the measured value at 10 GHz	62
4.26 Effective conductivity of NEG from the second waveguide	62
4.27 NEG thickness profile with x-ray	63
4.28 WR3.4 (left) and WR1.5 (right) waveguides from VDI made of Aluminum with a thin gold plating.	64
4.29 NEG coating of WR3.4 and WR1.5 waveguides	65
4.30 WR3.4 after NEG sputtering	65
4.31 Measurement setup at VDI	66
4.32 Transmission measurements along the WR3.4 waveguides	66
4.33 CST 3D model of WR3.4	67

4.34	S_{21} comparison between CST and measurements	68
4.35	NEG effective conductivity between 220-330 GHz	68
4.36	S_{21} comparison for different VNA	69
4.37	NEG effective conductivity between 220-330 GHz	70
4.38	SEM pictures after NEG coating of WR1.5	71
4.39	S_{21} measurements of NEG-coated WR1.5 waveguides	72
4.40	Comparison of S_{21} CST prediction with measurements along the WR1.5 waveguides	72
4.41	NEG effective conductivity at 500-750 GHz	73
4.42	WR3.4 waveguide separated in various blocks to apply NEG coating with different thickness	74
4.43	Effective conductivity between 220 and 330 GHz for a non-uniform profile . . .	74
4.44	Effective conductivity between 220 and 330 GHz for a non-uniform profile, with 1.5 μm and 1.8 μm the side walls	75
4.45	WR3.4 waveguide separated in various blocks to apply NEG coating with different thickness	75
4.46	Effective conductivity between 220 and 330 GHz for a non-uniform profile also on the side walls	76
4.47	Effective conductivity between 220 and 330 GHz for a non-uniform profile also on the side walls and compared with measured DC and roughness effects . . .	76
4.48	S_{21} comparison for measurements and the extracted conductivity for a non-uniform profile	77
4.49	WR1.5 waveguide separated in various blocks to apply NEG coating with different thickness	78
4.50	Effective conductivity between 500 and 750 GHz for a non-uniform profile also on the side walls and compared with measured DC and roughness effects . . .	78
4.51	Comparison of S_{21} CST prediction for the extracted conductivity with measurements along the WR1.5 waveguides	79
4.52	Mode spectrum of the horizontal coherent motion for zero chromaticity, as a function of transverse shunt impedance. The TMCI threshold is at 15 $\text{M}\Omega/\text{m}$. .	80
4.53	Mode spectrum of the vertical coherent motion for zero chromaticity, as a function of transverse shunt impedance. The TMCI threshold is at 3 $\text{M}\Omega/\text{m}$	81
5.1	The ALBA storage ring	83
5.2	Tune monitor for closed IVUs	85
5.3	Tune monitor for open IVUs	85
5.4	Bunch lengthening due to potential well distortion	86
5.5	Synchrotron tune shift as a function of current	87
5.6	Transverse wake function model in HEADTAIL	88
5.7	Normalized tune shift as predicted with HEADTAIL simulation based on current impedance model and as measured	88
5.8	HEADTAIL tune shift with extra BBR	89

List of Figures

5.9	Cross section of the injection kicker	90
5.10	3D model of the injection kicker with CST	91
5.11	CST 3D model of round multilayer structure	92
5.12	CST and ImpedanceWake2D impedance comparison for round multilayer structure	92
5.13	CST 3D model of a flat multilayer structure with a gap of 11.5 mm. The inner layer is ceramic of 6.5 mm thickness (yellow), the middle layer is air of 1 mm and the outer layer is Fe of 55 mm thickness (blue).	93
5.14	CST and ImpedanceWake2D impedance comparison for multilayer flat structure	94
5.15	CST and ImpedanceWake2D impedance comparison for multilayer flat structure	95
5.16	Comparison of the coating features with CST	95
5.17	Real kicker comparison with other models and IW2D	96
5.18	Vertical impedance of the ALBA kicker with ImpedanceWake2D	96
5.19	Normalized tune shift as predicted with HEADTAIL based on the impedance model with kickers and as measured	97
5.20	Pinger magnet installed in ALBA	98
5.21	Vertical tune shift before and after the pinger magnet	99
5.22	Vertical normalized tune shift before and after the pinger magnet	99
5.23	SLS light synchrotron at PSI	101
5.24	Y centroid at zero chromaticity for SLS2	102
5.25	Y centroid at zero chromaticity for SLS2 with 3HC	103
5.26	Y centroid at various positive chromaticities for SLS2	104
5.27	Y centroid at various negative chromaticities for SLS2	105
5.28	Y centroid for various R_s values and $Q'_y=-1$	106
5.29	Y centroid for 500 MHz RF and 0 chromaticity	108
5.30	Y centroid for 500 MHz and a 3HC	108
5.31	Y centroid for various bunch populations at zero chromaticity- lattice ca05q . .	110
5.32	Y centroid at various negative chromaticities for ca05q	111
5.33	Y centroid at 0 chromaticity for ca05q and 500 MHz	112
5.34	Y centroid at 0 chromaticity for ca05q and 500 MHz for RW and BBR model . .	112

List of Tables

1.1	CLIC main parameters	2
3.1	CLIC DR parameters	25
3.2	Thresholds for different chromaticity values	30
3.3	DR kicker parameters	40
4.1	SEM and XRF results on NEG thickness	60
5.1	Comparison of the CLIC DR and ALBA parameters	84
5.2	BBR parameters in the ALBA impedance model	87
5.3	RRW in the ALBA impedance model	87
5.4	Material properties in the multilayer round structure, simulated with Impedance-Wake2D	92
5.5	ImpedanceWake2D layers for flat multilayer structure	93
5.6	SLS2 parameters	101
5.7	Rise time for various positive chromaticities	104
5.8	Rise time for various negative chromaticities	105
5.9	Rise time for various negative chromaticities and $R_s=500$ k Ω /m	107
5.10	SLS2 parameters	107
5.11	Rise time for various negative chromaticities and $R_s=500$ k Ω /m for 500 MHz	108
5.12	SLS2 parameters	109
5.13	Rise time for various negative chromaticities and $R_s=500$ k Ω /m	110
5.14	SLS2 parameters	111

1 Introduction

1.1 Physics prospects for a future Linear Collider

The Standard Model (SM) [1-3] of particle physics is a successful theory providing the understanding of all interactions of subatomic particles and has been tested in many experiments over the last four decades. The latest triumph of the SM was the discovery of the SM Higgs boson with mass close to 126 GeV [4] in July 2012 from the two high luminosity LHC experiments ATLAS and CMS. The news of the Higgs boson discovery, the only elementary particle in the SM that was not yet observed and the experimental verification of the mechanism of electroweak symmetry breaking, which gives mass to elementary particles, caused a lot of excitement in the physics community.

Despite the fact that terascale physics is a reality with LHC, it is expected that high energy e^+e^- colliders will be needed to complement LHC studies with discovery and/or precision measurements. The prospect and physics motivation of an e^+e^- Linear Collider (LC) has been under scrutiny for several years. A LC will allow the exploration of SM physics, precise measurements of Higgs, as well as potential for new physics discovery. The exact requirements of this future collider will be defined from the pending further LHC results at 13 TeV, once it reaches operation at full energy and substantial integrated luminosity.

The Compact Linear Collider (CLIC) and the International Linear Collider (ILC) [5] are the two candidates for a future linear collider. CLIC (from 0.5 TeV to 3 TeV center-of-mass energy) uses the innovative idea of a separate driving beam to provide the accelerating power in the normal conducting Radio-Frequency (RF) cavities, while ILC (from 500 GeV to 1 TeV) relies on superconducting cavities.

Future linear colliders are the best known option for the post-LHC future but not the only one. Design studies are ongoing concerning Future Circular Colliders (FCC) with an emphasis on a hadron collider of 100 TeV and 80-100 km circumference. Potential for a lepton collider, TLEP, is also investigated and a lepton-hadron collider, VLHeC.

1.2 CLIC overview

The CLIC study focuses on the design of an e^+e^- linear collider operated at 3 TeV center-of-mass energy, necessary for investigation of new physics phenomena. In order to explore the full physics potential of such a collider, a broad range of center-of-mass energies is required. Therefore, stages of 500 GeV and 1.5 TeV are also being considered. It is still early to predict the final CLIC staging scenario, where future LHC operation at 13 TeV will give more insight, so this thesis is concentrated on the 3 TeV design. Figure 1.1 illustrates the CLIC accelerator complex layout at 3 TeV [6].

The polarized electrons for the main beam are obtained from a laser-driven DC gun and the primary electrons for production of positrons from a laser-driven RF gun. The electron and positron beams are accelerated to 2.86 GeV in the injector linacs and later deflected to the Damping Rings (DR) complex in order to reduce beam emittances to 500 nm horizontal and 5 nm vertical, normalized to the beam energy. After the DR, the beams are compressed longitudinally and accelerated to 9 GeV in a common booster linac before being transported through transfer lines to the turnarounds. The main linac uses 100 MV/m 12 GHz accelerating structures to achieve the final beam energy. A novel idea of generating high-current, low-energy drive beam to extract the necessary RF power is used for the main linac. The drive beam is generated in the main linacs of the top part of Figure 1.1, with 1 GHz fundamental RF frequency and then compressed in the Delay Loops and Combiner Rings (CR1 and CR2). The drive beam is parallel to the main beam and is decelerated in Power-Extraction Transfer Structures (PETS). In these structures, the drive beam generates RF power transferred into the main linac through waveguides. The beams collide in one Interaction Point (IP) after going through the Beam Delivery Section (BDS) for collimation and final focusing. The CLIC parameters at 3 TeV are presented in Table 1.1 for luminosity of $2 \times 10^{34} \text{cm}^{-2} \text{s}^{-1}$. Some margin exists for emittance blow-up in the linac [7], compared to the extracted DR emittances (including intra-beam scattering).

Table 1.1: CLIC main parameters at 3 TeV.

Description [units]	3 TeV
Total (peak 1%) luminosity	$5.9 (2.0) \times 10^{34}$
Total site length [km]	48.4
Accelerating gradient [MV/m]	100
Main Linac RF frequency [GHz]	12
Beam power/beam [MW]	14
Bunch charge [10^9]	3.72
Bunch separation [ns]	0.5
Bunch length [μm]	44
Beam pulse duration [ns]	156
Repetition rate [Hz]	50
Hor./vert. norm. emitt. [$10^{-6}/10^{-9}$ m]	0.66/20
Hor./vert. IP beam size [nm]	40/1

1.3 The CLIC Damping Rings

The novel scheme of the two beam acceleration was proposed to achieve the high luminosity required for the experiments at a high energy with the lowest possible cost. The CLIC DRs are responsible for producing the necessary ultra-low emittances of 500 nm.rad and 5 nm.rad normalized at 2.86 GeV with high bunch current in order to reach the desirable luminosity of the experiments which can be written as

$$\mathcal{L} = H_D \frac{N^2}{4\pi\sigma_x\sigma_y} n_b f_r, \quad (1.1)$$

where H_D is a factor describing the increase of luminosity due to beam-beam interaction, N the number of particles per bunch, $\sigma_{x,y}$ are the horizontal and vertical rms beam sizes at the IP, n_b the number of bunches per beam and f_r the repetition frequency of the beam pulses. The design of the DRs is guided by the main parameters of the collider. Four rings, shown in Figure 3.7 are necessary for the beam damping, two Pre-Damping Rings (PDR) and two DRs for the electron and positron beams due to the large input emittance from the positron source and the high repetition rate of 50 Hz.

The target emittances of the DRs in the horizontal and vertical plane are unprecedented, though rapidly approached by modern light sources, as shown in Figure 1.3. However, in the case of the CLIC DRs, also the normalized longitudinal beam emittance at extraction is very small, 6 keV.m [8].

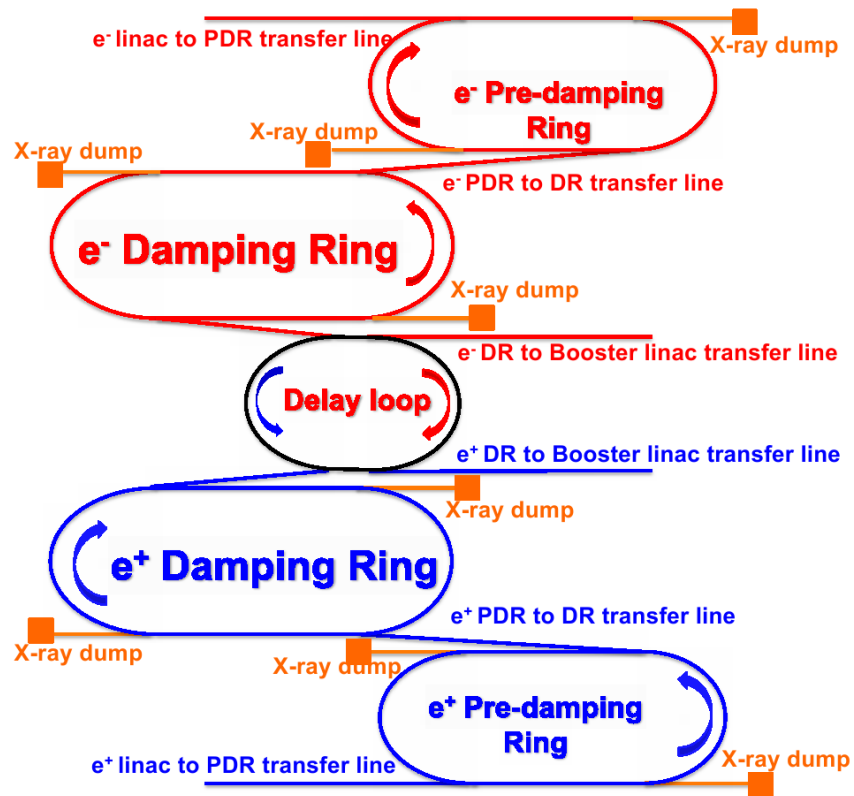


Figure 1.2: Schematic view of the DRs complex.

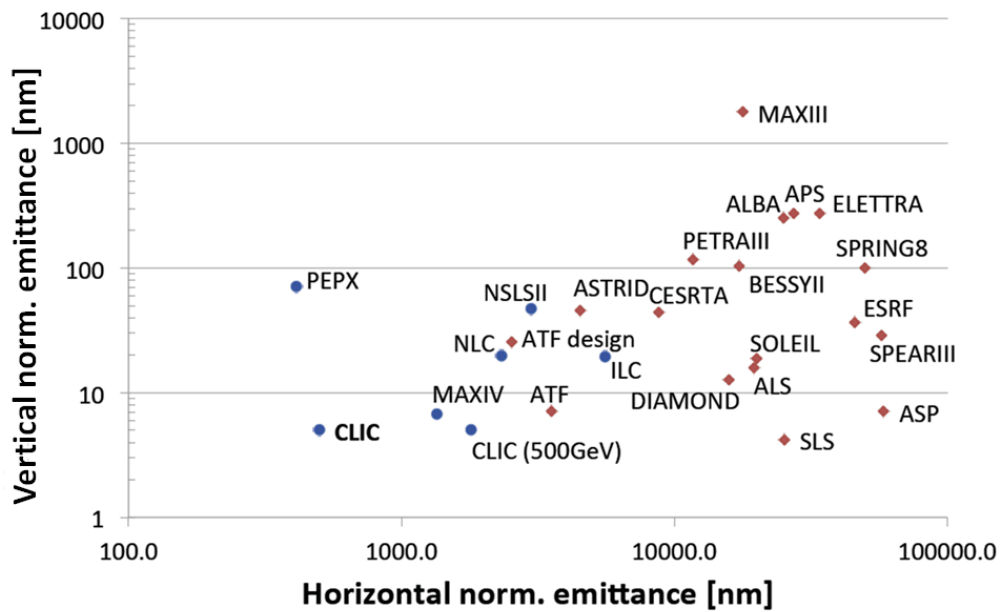


Figure 1.3: Modern light sources emittances target.

1.4 Scope of the thesis

The thesis is aiming to study the effect of coatings on beam coupling impedance, with emphasis at high frequencies. The first part concerns the CLIC DRs but the studies were extended to other light sources, like ALBA and SLS.

Chapter 2 contains the basic theory of beam dynamics of e^+e^- rings. Linear optics and single particle motion are introduced. Radiation damping and quantum excitation are briefly described. Wake fields and impedances are discussed and the concepts of effective impedance and tune shift are also introduced. In addition, the semi-analytical and numerical simulation tools used in this thesis are described.

Chapter 3 is dedicated to the impedance studies for the CLIC DRs. The transverse impedance model accounting for the whole ring is built with a broad-band resonator and several resistive wall contributors. For the resistive wall impedance, multilayer round and flat structures are considered using the electromagnetic material properties of each layer. Using the impedance model, single bunch simulations are performed with HEADTAIL to study the effect on beam dynamics and estimate the available impedance budget. Zero and positive chromaticities are considered as possible operational scenarios to define the budget. The effect of the coating thickness and material properties, especially at high frequencies, is studied and presented in this chapter. To further complete the impedance model, the injection kickers were studied. Numerical codes, like CST, reach their performance limit due to the extremely high number of mesh-cells required.

Chapter 4 contains all the studies realized for the electromagnetic characterization of NEG properties at high frequencies. The proposed method, based on the use of rectangular waveguides coated with the material under study, is described. In parallel, CST is extensively used for the simulation of the transmission coefficient parameters of the exact geometry waveguides. The benchmark of the method was realized in X-band (10-11 GHz) with waveguides made from known materials like stainless steel and copper, and later with the NEG coating. Chapter 4 also includes the measurements and analysis at few hundreds of GHz. The NEG conductivity is characterized between 220-330 GHz using WR3.4 [9] waveguides and between 500-750 GHz with WR1.5 [9] waveguides.

Chapter 5 focuses on studies on existing light sources, ALBA, as well as on future synchrotrons like SLS2. A set of single bunch measurements were performed in the ALBA synchrotron to study transverse mode coupling instabilities, the effect of open in-vacuum undulators and the effect of a pinger magnet recently installed in the ring. Measurements were compared to simulated results with HEADTAIL and ImpedanceWake2D codes. The same tools were applied to study the performance of the SLS upgrade (SLS2). For the latter study, the lattices considered have a low negative momentum compaction factor, as a result of the optics required to achieve the desired emittance reduction. The simulations' results for a resistive wall model are discussed at zero, positive and negative chromaticity operation. A first order estimate of the impedance budget is also presented.

Finally, in Chapter 6, the conclusions of the thesis are drawn and summarized.

2 Beam dynamics and collective effects

2.1 Linear beam optics

Electromagnetic forces are required to accelerate, bend and focus the charged particle beam inside a circular accelerator for the beam to stably remain on a closed orbit. Those forces, known as Lorentz forces, are derived from electric and magnetic fields through the Lorentz equation

$$\mathbf{F} = e[\mathbf{E} + (\boldsymbol{\nu} \times \mathbf{B})], \quad (2.1)$$

where e is the basic unit of the electrical charge, \mathbf{E} and \mathbf{B} are the electrical and magnetic field vectors and $\boldsymbol{\nu}$ is the velocity vector of the particle. A particle trajectory may follow a path described by

$$\begin{aligned} \mathbf{r}(s) &= \mathbf{r}_0(s) + \delta \mathbf{r}(s) \\ &= \mathbf{r}_0(s) + \delta x(s) \mathbf{u}_x(s) + \delta y(s) \mathbf{u}_y(s) + \delta z(s) \mathbf{u}_z(s), \end{aligned} \quad (2.2)$$

where $\mathbf{r}_0(s)$ is the reference orbit and three vectors $\mathbf{u}_x(s)$, $\mathbf{u}_y(s)$, $\mathbf{u}_z(s)$ form an orthogonal system, the Frenet-Serret coordinate system shown in Figure 2.1 [10], which moves along the trajectory with a reference particle at $\mathbf{r}_0(s)$. The plane defined by vectors $\mathbf{u}_x(s)$ and $\mathbf{u}_z(s)$, is referred to as horizontal plane and the plane perpendicular to it as vertical.

It is assumed that the magnetic field vector \mathbf{B} is perpendicular to the velocity vector, therefore transverse field components are considered, while the longitudinal magnetic field B_s can usually be neglected for studies on beam dynamics. The total velocity can be expressed as $v = \sqrt{v_x^2 + v_y^2 + v_s^2} \approx v_s$, since the transverse components of relativistic beams velocity are small compared to the longitudinal one (paraxial approximation). From the equilibrium of centrifugal and Lorentz force, the bending radius ρ of a particle under the influence of a homogeneous magnetic field B and relativistic factor β , is calculated by [11]

$$\frac{1}{\rho} [\text{m}^{-1}] = 0.2998 \frac{|B[\text{T}]|}{\beta E[\text{GeV}]} \quad (2.3)$$

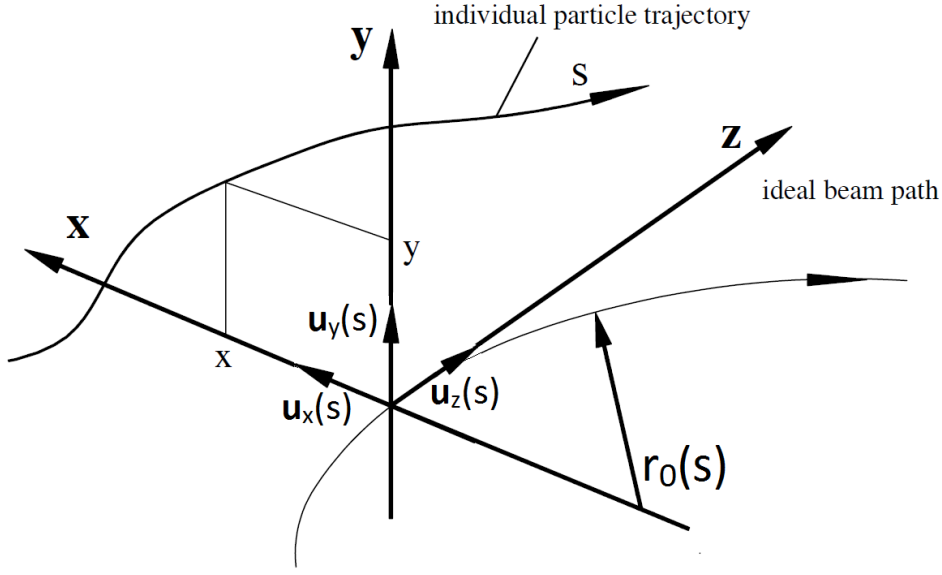


Figure 2.1: Frenet-Serret coordinate system.

The deflection angle in a magnetic field is

$$\theta = \int \frac{ds}{\rho}, \quad (2.4)$$

or for a uniform field like in a dipole magnet of arc length l , the deflection angle is $\theta = l/\rho$. Focusing or defocusing forces are created with the use of quadrupole magnets, whose field increases linearly with the distance and is zero on the s axis

$$B_x = gy, \quad B_y = -gx \quad \text{where} \quad g = \frac{\partial B_x}{\partial y} = -\frac{\partial B_y}{\partial x}. \quad (2.5)$$

A focusing quadrupole in the horizontal plane is also a defocusing quadrupole in the vertical plane.

2.1.1 Transverse betatron motion

Transverse particle motion around the reference orbit (i.e. the trajectory of the particle with nominal momentum which crosses all magnets on axis) is known as betatron motion. The linearized Hill's equation [13] describes the motion of particles in a circular machine since the amplitude of betatron motion is usually small

$$x''(s) + \left(\frac{1}{\rho^2(s)} - K_x(s) \right) x(s) = \frac{1}{\rho(s)} \frac{\Delta p}{p_0}, \quad (2.6)$$

$$y''(s) + K_y(s)y = 0, \quad (2.7)$$

where $K_{x,y}(s)$ is the effective focusing function with dimension $[\text{m}^{-2}]$, $\rho(s)$ is the bending radius of an element with position s and $\Delta p/p_0$ is the fractional momentum deviation of an off-momentum particle compared to the synchronous particle with momentum p_0 .

Using the general solutions of the homogeneous equations (for $\Delta p/p_0 = 0$), the transport of the particle's coordinates from point s_0 to point s , can be expressed in matrix formulation for linear elements as

$$\begin{pmatrix} u(s) \\ u'(s) \end{pmatrix} = M(s|s_0) \begin{pmatrix} u(s_0) \\ u'(s_0) \end{pmatrix}, \quad (2.8)$$

where $u(s)$, $u'(s)$ represent either horizontal or vertical phase-space coordinates.

For an off-momentum particle with $\Delta p/p_0 \neq 0$ oscillating around a dispersive closed orbit, the solution of the linearized inhomogeneous Eq.(2.6) can be expressed as a linear superposition of the particular solution and the solution of the homogeneous equation

$$x = x_\beta(s) + D(s)(\Delta p/p_0), \quad (2.9)$$

where the solution $D(s)$ of the inhomogeneous equation is called the dispersion function and $r_0(s) + D(s)(\Delta p/p_0)$ represents the off-momentum closed orbit.

The transfer matrices for a constant focusing function K are

$$M(s|s_0) = \begin{cases} \begin{pmatrix} \cos(\sqrt{K}l) & \frac{1}{\sqrt{K}} \sin(\sqrt{K}l) \\ -\sqrt{K} \sin(\sqrt{K}l) & \cos(\sqrt{K}l) \end{pmatrix} & K > 0: \text{focusing quad} \\ \begin{pmatrix} 1 & l \\ 0 & 1 \end{pmatrix} & K = 0: \text{drift space} \\ \begin{pmatrix} \cosh(\sqrt{|K|}l) & \frac{1}{\sqrt{|K|}} \sinh(\sqrt{|K|}l) \\ \sqrt{|K|} \sinh(\sqrt{|K|}l) & \cosh(\sqrt{|K|}l) \end{pmatrix} & K < 0: \text{defocusing quad} \end{cases} \quad (2.10)$$

where $l = s - s_0$. The transfer matrix for a quadrupole can be reduced within the thin-lens approximation where the quadrupole length $l \rightarrow 0$ to

$$M_{\text{focusing}}^{\text{quad}} = \begin{pmatrix} 1 & 0 \\ -1/f & 1 \end{pmatrix}, \quad M_{\text{defocusing}}^{\text{quad}} = \begin{pmatrix} 1 & 0 \\ 1/f & 1 \end{pmatrix}, \quad (2.11)$$

where the focal length f is given by $f = \lim_{l \rightarrow 0} \frac{1}{|K|l}$.

The transfer matrix of a sector dipole, for which the particle trajectories enter and exit with

perpendicular entrance and exit angles to the edge of the dipole field, is given by

$$M_{\text{dip}} = \begin{pmatrix} \cos\theta & \rho \sin\theta \\ -\frac{1}{\rho} \sin\theta & \cos\theta \end{pmatrix}, \quad (2.12)$$

where $\theta = l/\rho$ is the orbiting angle, ρ is the bending radius and l is the dipole length. In small-angle approximation, the transfer matrix reduces to that of a drift space

$$M_{\text{dip}} = \begin{pmatrix} 1 & l \\ 0 & 1 \end{pmatrix}. \quad (2.13)$$

The transfer matrix for any intervals, made up of sub-intervals, is the product of the transfer matrices of the sub-intervals

$$M(s_2|s_0) = M(s_2|s_1)M(s_1|s_0). \quad (2.14)$$

Using the Floquet transformation, the solutions to the homogeneous Hill's equations can be written in the form

$$u(s) = Aw(s) \cos(\phi(s) + \phi_0), \quad (2.15)$$

where A describes the amplitude dependence on the initial conditions and $w(s)$ the amplitude dependence on the machine lattice, $w(s) = \sqrt{\beta_{x,y}(s)}$. Thus, the beta function $\beta(s)$, also known as the amplitude function, is introduced. Functions $w(s) = w(s+C)$ and $\phi(s) = \phi(s+C)$ are periodic with period equal to the machine circumference C , and $u(s)$ can be a horizontal or vertical coordinate. The initial conditions determine the phase ϕ_0 . Substituting Eq.(2.15) in (2.6) and (2.7), the Courant-Snyder (also known as betatron or Twiss) parameters $\alpha(s)$, $\beta(s)$ and $\gamma(s)$, as well as the betatron phase advance $\phi(s)$ can be defined

$$\begin{aligned} \alpha(s) &\equiv -\frac{1}{2} \frac{d\beta(s)}{ds}, \\ \gamma(s) &\equiv \frac{1 + \alpha^2(s)}{\beta(s)}, \\ \phi(s) &\equiv \int_0^s \frac{ds'}{\beta(s')}. \end{aligned} \quad (2.16)$$

The Twiss functions are periodic, with a periodicity equal to the machine circumference C . One betatron oscillation is performed when the phase advance is equal to 2π . The number of betatron oscillations in one revolution period is called the betatron tune, defined in the horizontal or vertical plane as

$$Q_{x,y} = \frac{1}{2\pi} \int_0^C \frac{ds}{\beta_{x,y}(s)}. \quad (2.17)$$

Single particle emittance

Let's assume in Eq.(2.6) that $1/\rho = 0$ and $\Delta p/p_0 = 0$. The motion of an on-momentum particle at any point of the lattice is described by the Floquet solutions of Eq.(2.15), which can be written in the form [13] in the horizontal plane

$$\begin{aligned} x(s) &= \sqrt{\varepsilon_x} \sqrt{\beta_x(s)} \cos(\phi_x(s) + \phi_0) \\ x'(s) &= -\frac{\sqrt{\varepsilon_x}}{\sqrt{\beta_x(s)}} \left[\sin(\phi_x(s) + \phi_0) + \alpha_x(s) \cos(\phi_x(s) + \phi_0) \right], \end{aligned} \quad (2.18)$$

by replacing the amplitude factor A in Eq.(2.15) with $\sqrt{\varepsilon_x}$.

The solutions $x(s)$ and $x'(s)$ satisfy the equation of an ellipse in the $x - x'$ plane given by

$$\gamma_x(s)x^2(s) + 2\alpha_x(s)x(s)x'(s) + \beta_x(s)x'^2(s) \equiv \varepsilon_x. \quad (2.19)$$

This invariant expression is called the Courant-Snyder invariant and describes an ellipse (shown in Figure 2.2) with constant phase space area $\pi\varepsilon_x$ in (x, x') , where ε_x is called the geometrical emittance. The Courant-Snyder invariant describes the single particle emittance.

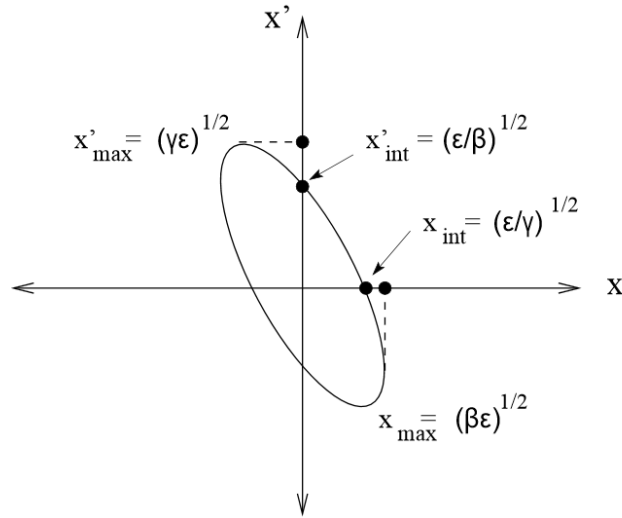


Figure 2.2: Elliptical trajectory in horizontal phase space of a particle at location s .

The shape of the ellipse depends on the Twiss parameters around the ring as can be seen from Eq.(2.19), therefore it has a different shape and orientation at different positions along the ring, but always a constant area. It is useful to introduce the normalized emittance, $\beta\gamma\varepsilon_x$, which is the quantity kept constant when the particle's energy changes.

Generally the transfer matrix M in one period, can then be expressed as

$$M_{0 \rightarrow s} = \begin{pmatrix} \sqrt{\frac{\beta(s)}{\beta_0}} (\cos \phi + \alpha_0 \sin \phi) & \sqrt{\beta(s)\beta_0} \sin \phi \\ \frac{(\alpha_0 - \alpha(s)) \cos \phi - (1 + \alpha_0 \alpha(s)) \sin \phi}{\sqrt{\beta(s)\beta_0}} & \sqrt{\frac{\beta_0}{\beta(s)}} (\cos \phi - \alpha_0 \sin \phi) \end{pmatrix}, \quad (2.20)$$

where α , β and γ are the Twiss parameters and $\phi = \int_0^s \frac{ds'}{\beta(s')}$ is the phase advance between points 0 and s . The evolution of Twiss functions is expressed through

$$\begin{pmatrix} \beta_s \\ \alpha_s \\ \gamma_s \end{pmatrix} = \begin{pmatrix} M_{11}^2 & -2M_{11}M_{12} & M_{12}^2 \\ -M_{11}M_{21} & M_{11}M_{22} + M_{12}M_{21} & -M_{12}M_{22} \\ M_{21}^2 & -2M_{21}M_{22} & M_{22}^2 \end{pmatrix} \begin{pmatrix} \beta_{s0} \\ \alpha_{s0} \\ \gamma_{s0} \end{pmatrix}, \quad (2.21)$$

where M_{ij} represents the transfer elements of $M(s_1|s_0)$. Similar expressions as the ones described above, are valid for the vertical plane too. In the ideal case, where the three planes are fully decoupled, three independent two-dimensional emittances are defined.

Beam emittance

The solution of the linear equations of motion describes the single particle trajectory through an array of magnetic elements. In reality, there is a beam of many particles and the beam emittance is the physical quantity used to describe collective motion. Therefore, a definition of beam emittance based on the distribution of particles in the phase space is often more practical and a statistical definition for emittance is used.

The beam emittance is the area of the ellipse in (x, x') space that contains the motion of a given fraction of particles. The rms emittance, ε_{rms} , usually used in electron machines, is defined as the area (divided by π) of the ellipse containing 39% of the particles. In proton machines, the area (divided by π) that contains 95% of the particles is used, the $\varepsilon_{95\%}$.

According to Liouville's theorem, under the influence of conservative forces, the phase space area enclosed by all particles with a given emittance is constant [10] as they move around the machine. Since the number of particles is also constant, the local phase space density is constant.

Chromaticity

Particles with different momentum feel a different transverse focusing strength when they pass through a quadrupole. This different focusing results into a different number of oscillations per turn for off-momentum particles, therefore a tune shift ΔQ with respect to the main tune Q_0 of the synchronous particle. A tune shift introduced due to momentum spread is a

parameter characterized from what is defined as chromaticity ξ

$$\frac{\Delta Q}{Q_0} = \xi \frac{\Delta p}{p_0}. \quad (2.22)$$

This is only the natural chromaticity. Also sextupoles in dispersive regions are a source of chromaticity or are used to correct the normal chromaticity.

2.1.2 Longitudinal synchrotron motion

Acceleration of particles and longitudinal focusing is achieved with Radio Frequency (RF) longitudinal electric fields obtained with a system of RF cavities. The longitudinal RF electric field E_s applied to particles with phase ϕ_s with respect to the phase of the RF cavity voltage $\phi_{\text{rf}}(t) = \omega_{\text{rf}}t$, can be expressed [11] as

$$E_s(t) = E_0 \sin(\omega_{\text{rf}}t + \phi_s), \quad (2.23)$$

where E_0 is the field amplitude and ω_{rf} is the RF frequency. As the electric field is time dependent, a particle needs to be synchronized with the RF cavity in order to experience the desired longitudinal kick. This particle with a revolution period $T_0 = C/(\beta c)$ and momentum p_0 is called the synchronous particle and will always reach the cavity on the same phase for the electric field. This phase corresponds to a zero electric field if the RF is only focusing, or to a constant non-zero value if the RF is accelerating the bunch. Therefore, the RF frequency ω_{rf} needs to be an integer multiple h of the angular revolution frequency of a synchronous particle ω_0

$$\omega_{\text{rf}} = h\omega_0, \quad (2.24)$$

where h is also known as the harmonic number and ultimately indicates the maximum number of bunches that can be accelerated in the machine. The energy gain per turn ΔE_s of a synchronous particle passing through the RF cavity is given by

$$\Delta E_s = eV_0 \sin(\phi_s), \quad (2.25)$$

where e is the charge and V_0 the RF voltage amplitude.

Momentum compaction factor and slip factor

Non synchronous particles with momentum deviation $\Delta p/p_0$ cause a change of the shape and length L of the closed orbit, $\Delta L = L - L_0$. The momentum compaction factor is defined as

the ratio of the fractional change of the orbit for a given fractional change in the momentum

$$\alpha_p = \frac{\Delta L/L_0}{\Delta p/p_0}. \quad (2.26)$$

It can be demonstrated that the phase slip factor η , defined as

$$\eta = \alpha_p - \frac{1}{\gamma^2}, \quad (2.27)$$

represents $\frac{\Delta\omega/\omega_0}{\Delta p/p_0}$, i.e. the fractional revolution frequency change for a given fraction momentum change.

The slip factor can be either positive or negative (or equal to 0) depending whether the synchrotron operates above or below transition respectively. In fact, η changes sign at $\gamma_t = \sqrt{\frac{1}{\alpha_p}}$.

The CLIC DRs operate well above transition, being $\gamma = 5597$ and $\gamma_t = \sqrt{\frac{1}{\alpha_p}} = \sqrt{\frac{1}{1.3 \times 10^{-4}}} = 88$ [14].

2.2 Synchrotron radiation damping and quantum excitation

When charged particles are accelerated in an electromagnetic field according to classical electrodynamics, they radiate energy in the form of electromagnetic waves. The total radiated power of an accelerated particle with charge e moving with momentum $\mathbf{p} = m_0\mathbf{u}$ (assuming that particle's velocity is not relativistic), is given by Larmor's formula [13]

$$P_s = \frac{e^2}{6\pi\epsilon_0 m_0^2 c^3} \left(\frac{d\mathbf{p}}{dt} \right)^2, \quad (2.28)$$

where $\epsilon_0 = 8.85419 \times 10^{-12} \text{AsV}^{-1}\text{m}^{-1}$ is the permittivity of free space, m_0 the particle's rest mass and c the speed of light. This formula shows that the electromagnetic energy is emitted when there is a change in particle's momentum as a result of an applied force, i.e. $d\mathbf{p}/dt \neq 0$. In the case of non-relativistic particles, the emitted radiation is described by classical electrodynamics and may be neglected since it is very weak. For relativistic particles, the radiation power can be written as

$$P_s = \frac{e^2 c}{6\pi\epsilon_0 (m_0 c^2)^2} \left[\left(\frac{d\mathbf{p}}{d\tau} \right)^2 - \frac{1}{c^2} \left(\frac{dE}{d\tau} \right)^2 \right], \quad (2.29)$$

by using the Lorentz-invariant form of Eq.(2.28) and by transforming dt to $d\tau = \frac{1}{\gamma} dt$.

In the case of circular acceleration where particles are bent perpendicular to their direction of motion, such as in the case of the CLIC DR, and the particle's energy remains constant, the

2.2. Synchrotron radiation damping and quantum excitation

general radiation formula (2.29) is reduced to

$$P_s = \frac{e^2 c \gamma^2}{6\pi \epsilon_0 (m_0 c^2)^2} \left(\frac{d\mathbf{p}}{dt} \right)^2. \quad (2.30)$$

The change of particle's momentum in a circular path with bending radius ρ , can be expressed as

$$\frac{dp}{dt} = p \frac{v}{\rho}. \quad (2.31)$$

By inserting the relation (2.31) into (2.30) and for $v \simeq c$, the instantaneous radiation power from circular motion, or else the synchrotron radiation, is then given by Liénard's relation

$$P_s = \frac{e^2 c}{6\pi \epsilon_0 (m_0 c^2)^4} \frac{E^4}{\rho^2}. \quad (2.32)$$

For particles of a given energy E , the radiated power is inversely proportional to the fourth power of the rest mass m_0 , therefore it is important for electrons or positrons, while for protons it becomes significant only at energies of several hundreds or thousands of GeV.

An important concept is that of the energy radiated by a particle with energy E per revolution period in a circular machine, which is given by

$$U_0 = \oint P_s dt = \frac{C_\gamma}{2\pi} E^4 \oint \frac{1}{\rho^2} ds \equiv \frac{C_\gamma}{2\pi} E^4 I_2, \quad (2.33)$$

where C_γ is a physical constant given by $C_\gamma = \frac{4\pi}{3} \frac{r_0}{(m_0 c^2)^3} = 8.846 \times 10^{-5} \text{m/GeV}^3$ for electrons and I_2 is the second radiation integral.

The energy lost due to synchrotron radiation results in a particle's momentum reduction in all three planes. With the RF field, the energy loss is only compensated in the longitudinal plane, leading to a net reduction of the transverse betatron oscillation amplitude (or else damping). Betatron and synchrotron oscillations are damped exponentially with damping times defined as

$$\begin{aligned} \tau_x &= \frac{2E_0 T_0}{j_x U_0} = \frac{2E_0 T_0}{(1 - I_4/I_2) U_0}, \\ \tau_y &= \frac{2E_0 T_0}{j_y U_0} = \frac{2E_0 T_0}{U_0}, \\ \tau_z &= \frac{2E_0 T_0}{j_z U_0} = \frac{2E_0 T_0}{(2 + I_4/I_2) U_0}, \end{aligned} \quad (2.34)$$

where T_0 is the revolution period, $j_x = 1 - I_4/I_2$, $j_y = 1$ and $j_z = 2 + I_4/I_2$ the damping partition numbers, $I_4 = \oint \frac{\eta_x}{\rho} \left(\frac{1}{\rho^2} + 2k_1 \right)$ the fourth synchrotron radiation integral, η_x the horizontal

dispersion and $k_1 = \frac{e}{p_0} \frac{\partial B_y}{\partial x}$. The damping partition numbers j_x , j_y and j_z satisfy the Robinson theorem [11]

$$j_x + j_y + j_z = 4. \quad (2.35)$$

If radiation damping was the only effect, then after a while, the amplitude of oscillations would be close to zero and the beam would have a negligibly small emittance. However, there is another effect balancing the radiation damping, known as quantum excitation. Photons are emitted with a distribution with an angular width $1/\gamma$, about the direction of motion of electrons. This leads to some vertical recoil that excites vertical betatron motion, resulting in a non-zero vertical emittance. Furthermore, if a particle emits a photon at a place with non-zero dispersion, it loses energy and instantly starts performing betatron oscillations around a different equilibrium orbit. This statistical nature of the emission of photons leads to a continuous increase of the betatron amplitudes and of the beam size. The balance between synchrotron radiation damping and quantum excitation, defines an equilibrium state of the beam distribution. Synchrotron radiation also causes damping of the longitudinal particle oscillations. While a particle executes a synchrotron oscillation, it loses more (less) energy while it has a higher (lower) energy than the synchronous particle so that in phase space it tends to spiral towards the center, a process called longitudinal radiation damping.

2.3 Wake fields and impedances

A charged particle beam while traveling along an accelerator feels the external electromagnetic (EM) fields necessary for guidance but also interacts electromagnetically with its vacuum chamber surroundings. The EM fields induced by the beam itself are known as wake fields since they stay behind the traveling source in the case of ultra-relativistic beams. Wake fields can affect the beam dynamics by acting back on it. This perturbation is a collective effect and can limit the performance of an accelerator. For frequencies above the cutoff frequency of the beam pipe, wake fields propagate away while for lower frequencies, they remain inside the structure in which they were excited.

In frequency domain, vacuum chamber components are represented as frequency dependent complex impedances. The coupling impedance for a particular component can be narrow band with quality factor $Q \gg 1$, like in a cavity, or broad band with $Q \approx 1$, e.g. due to change in the cross section of the vacuum chamber. Narrow band resonators can ring inside a structure for a long time, affecting subsequent bunches or the same bunch after one or more revolutions, and can cause multi-bunch instabilities. Broad band resonators last short and are mainly responsible for single bunch instabilities. In the design stage of an accelerator, it is necessary to budget a total impedance that is consistent with the designed beam intensity requirements. Transverse and longitudinal collective effects are usually studied separately.

The longitudinal wake potential is the voltage gain of a trailing particle due to fields created from a leading particle. The transverse wake potential is a transverse momentum kick expe-

rienced by a trailing particle due to the wake fields from a leading particle. Turn after turn, this transverse force can excite the motion of trailing particles leading to coherent oscillations with growing amplitude. Wake functions or potentials are used for beam dynamics studies in the time domain, whereas the Fourier transform of the wake function, the impedance, is used for frequency domain analysis.

An example of the wake fields, the results of the transverse electric field generated with 3D CST Particle Studio [12] as an ultra-relativistic bunch passes through the injection kicker of the ALBA light source (illustrated in Figure 2.3), are shown in Figure 2.4.

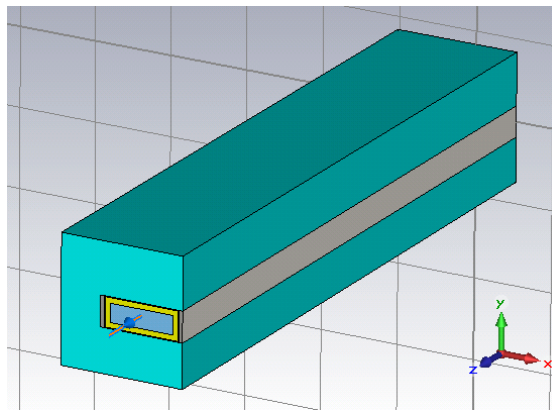


Figure 2.3: CST model of the ALBA kicker magnet: ceramic in yellow and coated with a thin Titanium (Ti) layer, C-shaped Ferrite (Fe) yoke in blue and Perfect Electric Conductor (PEC) in grey.

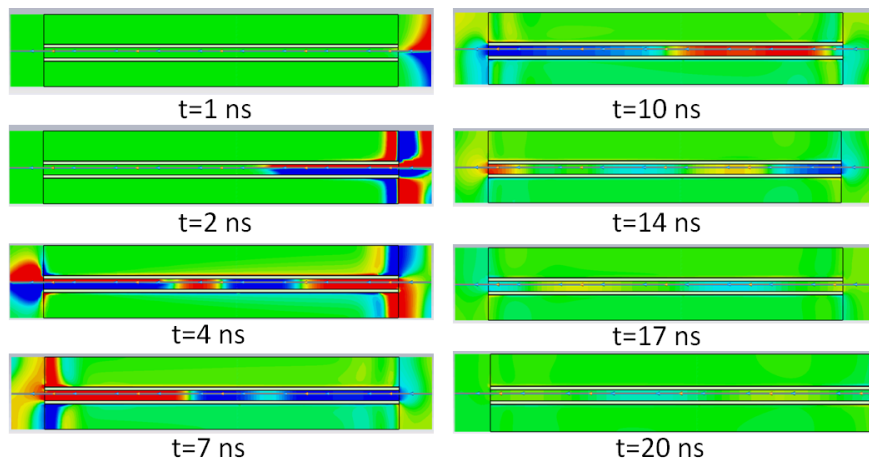


Figure 2.4: Vertical electric wake field simulated with CST at various times t in the $x = 0$ plane. At $t=1$ ns, the vertical electric fields, created by the bunch, can be seen radiating from the beam location on the right side of the structure. At $t=2$ ns, the bunch passes through the kicker and its electric fields get distorted, while reflections are also observed. At 4 ns, the bunch exits the kicker on the left and wake fields start to weaken till 20 ns.

2.3.1 Longitudinal plane

A relativistic particle q_1 (source particle) going through a structure of arbitrary cross section and length L will leave behind an oscillating field and the trailing particle q (test particle) at distance z from the source will feel the effect of the Lorentz force (Figure. 2.5).

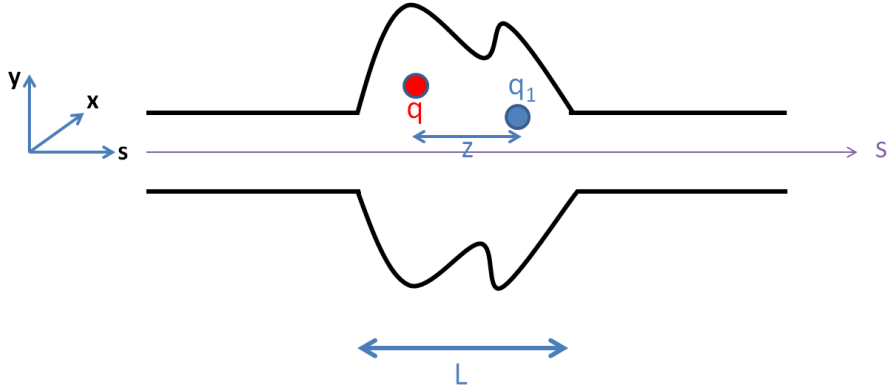


Figure 2.5: Source (q_1) and test (q) particles in an accelerator component with an arbitrary geometry.

Each charge traveling down an accelerator chamber (source) creates a wake field on the trailing particle (test), situated at a distance z from it. The longitudinal wake function is defined by integrating the Lorentz force felt by the test particle q along the length L of the component in which the wake field is created from the source particle q_1 as

$$W_{\parallel}(x, y, x_1, y_1, z)[V/C] = -\frac{1}{q_1 q} \int_0^L F_{\parallel}(x, y, s, x_1, y_1, z) ds, \quad (2.36)$$

where $F_{\parallel} = qE_s$ is the longitudinal Lorentz force and E_s the longitudinal electric field induced by the source q_1 . The transverse offset from the center of the component of the source and test particle are described by (x_1, y_1) and (x, y) . The zero-order longitudinal wake, $W_{\parallel}^{(0)}(z)$, is calculated when both source and test are on axis, i.e. when $x_1 = y_1 = x = y = 0$ in an axisymmetric structure.

The longitudinal beam coupling impedance for relativistic particles is defined as

$$Z_{\parallel}(\omega)[\Omega] = \frac{1}{c} \int_{-\infty}^{\infty} W_{\parallel}^{(0)}(z) e^{-\frac{i\omega z}{c}} dz, \quad (2.37)$$

where i is the imaginary unit and $\omega = 2\pi f$ the angular frequency.

2.3.2 Transverse plane

Transverse wake fields appear when a particle travels in an asymmetric vacuum chamber, or off-centered in a symmetric chamber, and the wake functions can be defined as

$$W_{x,y}(x, y, x_1, y_1, z) [\text{V/C/m}] = -\frac{1}{q_1 q} \int_0^L F_{x,y}(x, y, s, x_1, y_1, z) ds. \quad (2.38)$$

The transverse wake functions can be expanded in first order as series of the source's and test's offset as [15]

$$\begin{aligned} W_x(x, x_1, z) &= W_x^{\text{dip}}(z)x_1 + W_x^{\text{quad}}(z)x, \\ W_y(y, y_1, z) &= W_y^{\text{dip}}(z)y_1 + W_y^{\text{quad}}(z)y, \end{aligned} \quad (2.39)$$

where $W_{x,y}^{\text{dip}}$, in units of $\left(\frac{\text{V}}{\text{Cm}}\right)$, is the horizontal and vertical dipolar wake functions respectively (often called driving) and $W_{x,y}^{\text{quad}}$ is the horizontal and vertical quadrupolar (often called detuning) wake functions. The sum of dipolar and quadrupolar terms define the generalized wake, $W_{x,y}^{\text{gen}}$. For small source and test offset, Eq.(2.39) represents a very good approximation of the transverse wakes.

As a consequence, also the transverse beam coupling impedance of an element can be decomposed in dipolar and quadrupolar terms, since it is defined as the Fourier transform of the corresponding wake function

$$Z_{x,y}^{\text{dip}}(\omega) [\Omega/\text{m}] = \frac{i}{c} \int_{-\infty}^{\infty} W_{x,y}^{\text{dip}}(z) e^{-\frac{i\omega z}{c}} dz, \quad (2.40)$$

$$Z_{x,y}^{\text{quad}}(\omega) [\Omega/\text{m}] = \frac{i}{c} \int_{-\infty}^{\infty} W_{x,y}^{\text{quad}}(z) e^{-\frac{i\omega z}{c}} dz, \quad (2.41)$$

and can also be expanded into a power series of source's and test's offset similar to the wake functions in the time domain

$$\begin{aligned} Z_x(\omega) &= Z_x^{\text{dip}}(\omega)x_1 + Z_x^{\text{quad}}(\omega)x, \\ Z_y(\omega) &= Z_y^{\text{dip}}(\omega)y_1 + Z_y^{\text{quad}}(\omega)y. \end{aligned} \quad (2.42)$$

Eq.(2.39) and (2.42) are valid for structures with left/right and top/bottom symmetry and a beam traveling on axis. In different cases, the above equations should be rewritten taking into account the presence of a constant term [16].

2.3.3 Effective impedance

The effective coupling impedance is defined as the sum for an infinite number of frequencies of the product of the coupling impedance and the normalized spectral density [17–19]

$$\left(\frac{Z_{\parallel}}{\omega}\right)_{\text{eff}} = \frac{\sum_{p=-\infty}^{+\infty} \frac{Z_{\parallel}(\omega')}{\omega'} h_l(\omega')}{\sum_{p=-\infty}^{+\infty} h_l(\omega')}, \quad (2.43)$$

$$(Z_{\perp})_{\text{eff}} = \frac{\sum_{p=-\infty}^{+\infty} Z_{\perp}(\omega') h_l(\omega' - \omega_{\xi})}{\sum_{p=-\infty}^{+\infty} h_l(\omega' - \omega_{\xi})}.$$

In the above equations, $h_l(\omega)$ is the power spectral density of the mode l , ω_{ξ} the chromaticity frequency shift, defined as $\omega_{\xi} = \frac{\xi\omega_{\beta}}{\eta}$, and $\omega' = p\omega_0 + \omega_{\beta} + l\omega_s$, where ω_0 is the revolution angular frequency, ω_{β} the betatron angular frequency, ω_s the synchrotron frequency and l the azimuthal mode number. In the case of a Gaussian beam as in the CLIC damping rings, the spectral density can be written as [19]

$$h_l(\omega) = \left(\frac{\omega\sigma}{c}\right)^{2l} e^{-\frac{\omega^2\sigma^2}{c^2}}, \quad (2.44)$$

where σ is the root mean square (rms) bunch length.

The effective impedance describes the effect of impedance on beam dynamics and depends on the beam properties. It can be seen that the real part of $(Z_0^{\parallel}/\omega)_{\text{eff}}$ is related to the growth or damping rate, while the imaginary part to the frequency shift of the particular mode under consideration. Whether this mode will be driven significantly or not, depends on the overlap of the impedance with the mode spectrum.

Tune shift in the transverse plane

Assuming a Gaussian beam, the complex frequency shift in betatron frequency is expressed by the formula [19]

$$\Omega^{(l)} - \omega_{\beta} - l\omega_s \approx -\frac{1}{4\pi} \frac{\Gamma(l + \frac{1}{2})}{2^l l!} \frac{Nr_0 c^2}{\gamma T_0 \omega_{\beta} \sigma} i (Z_{\perp})_{\text{eff}}, \quad (2.45)$$

where N is the number of particles in the bunch, T_0 the revolution time and σ the bunch length. The above equation indicates that the imaginary component of the effective transverse impedance contributes to a real coherent tune shift, and the real component to an imaginary tune shift, visible as a growth or decay in the oscillation.

2.4 Electromagnetic simulation tools of wakefields and impedances

2.4.1 CST Studio Suite

CST Particle Studio is a commercial 3D Computer Aided Design (CAD) software that allows the computation of EM fields of a modeled bunch inside a structure. The structure is subdivided into homogeneous mesh cells where Maxwell's equations can then be solved numerically. A Gaussian particle bunch is the excitation of the structure under study, or else the source, and a trailing particle that feels the EM force of the source. The Wakefield Solver can be used for the calculation of wake potentials as a function of the time delay τ with respect to the passage of the source in time domain and, in frequency domain, the beam coupling impedance, i.e. the Fourier transform normalized to the bunch spectrum.

Simulation of the driving and detuning terms of the transverse wake potentials is also possible since CST allows the separate definition of transverse position of the source and test. The total number of mesh cells that can be simulated, limited by CPU memory, can affect the achieved resolution of the results. Therefore, convergence studies are necessary. Other parameters of the CST simulation setup should also be chosen carefully, as they contribute essentially to the accuracy of the results such as the simulated wake length (distance from the source for the wake calculation), the integration method as well as the boundary and symmetry conditions [16].

2.4.2 ImpedanceWake2D

Beam-coupling impedances can be distinguished into two main categories: one being the geometric impedance, such as contribution from tapering, cavities and step transitions around the accelerator and the second part being the resistive-wall impedance. The geometric contribution can be short-range in time domain, if it concerns a broad-band impedance source such as tapering, or a long-range effect if the source is a cavity-like object.

One of the most important contributions in terms of impedance is due to the material properties surrounding the beam, therefore due to the material resistivity. Resistive-wall impedance is harder to be cured and therefore essential to be studied during the design or operation of a machine. Solutions to fight against resistive-wall impedance are to increase the beam pipe radius, which necessarily increases the cost of the ring and might be not compatible with the magnet apertures, or choose materials with the minimum effect of impedance.

In order to compute the resistive-wall impedance of long beam chambers, a common approximation is to assume a two-dimensional geometry with an infinite length and calculate the fields of a beam close to the center of the structure. The ImpedanceWake2D [20] (IW2D) code is used to compute the transverse beam coupling impedances and wake functions of infinitely long multilayer structures with a round or flat geometry. The computation of the beam-coupling impedances and wake functions of an axisymmetric multilayer structure is based on Zotter's formalism [21–26] but further extended to the general nonlinear beam coupling impedances [27]. Detailed information can be found in [27].

3 Transverse impedance budget of the CLIC DR

3.1 Introduction

The interaction of charged particle beams with the surroundings, and the related energy loss and transverse kick due to a particular machine element or the vacuum chamber, are expressed in terms of beam coupling impedance in the frequency domain. The concepts of impedance and wake fields were already introduced in Chapter 2. These interactions need to be evaluated in order to estimate the thresholds of coherent instabilities, which may limit the achievable beam current.

For this reason, early in the design stage of the CLIC DRs, these interactions have to be taken into account, as they define a total impedance budget for the various elements that will be installed and limit the choice of materials and shapes of the components required for its operation. The total impedance budget needs to be consistent with the design intensity requirements.

When the details of the machine elements are still unknown and their design is not yet available, the full ring is usually modeled with a total impedance made of three main components: resistive wall, several narrow-band resonators and one broad-band resonator. A narrow-band resonator models cavity-like objects. Its wake field is long range and mainly affects many bunches, therefore, it mainly impacts on multi-bunch instabilities. A broadband resonator models the global effect of all discontinuities of the beam pipe and all devices exhibiting short-lived wakes. It replaces the effect of the actual impedance consisting of many small short range contributions and is responsible for single bunch instabilities.

In this Chapter, we will discuss the impact of transverse impedance for single bunch instabilities focusing on the transverse plane by considering two contributions. First, only a broad-band resonator is considered to model the entire ring. As a second step, a resistive wall is added to the model representing the contribution of the wigglers with their tiny apertures of 6 mm, the arcs and the rest of the FODO cells.

3.2 The HEADTAIL code

The HEADTAIL code [28] is the program used for the simulation of transverse single bunch phenomena associated with impedance. Given a model of short-range wakefields, the study of the single-bunch beam dynamics is done using macro-particles, where each macro-particle is tracked through the ring subdivided into kick sections. The beam and the machine parameters are given as input in the code.

One of the outputs of the code which reveals the onset of coherent instabilities is, for example, the bunch centroid motion as a function of time. The interaction between bunch and wake (or impedance) is modeled by one or more kicks given at each turn to each of the macro-particles. At each kick location, every bunch (equally populated with particles) is sliced to the input number of slices and the average transverse positions offsets from the reference orbit are computed. The slicing stops at a given number of σ_z^{rms} , predefined in the input file (usually from $-2\sigma_z$ to $+2\sigma_z$). Each macro-particle receives a kick in all three directions, $x'_i + \Delta x'_i$, $y'_i + \Delta y'_i$, $\delta_i + \Delta\delta_i$, due to the wake fields generated by the preceding slices, assumed to be wake sources, where

$$\begin{aligned}\Delta x'_i &= \frac{e^2}{E_0} \sum_{z_s > z_{s_i}} n_s \left[W_x^{\text{dip}}(z_s - z_{s_i}) x_s + W_x^{\text{quad}}(z_s - z_{s_i}) x_i \right], \\ \Delta y'_i &= \frac{e^2}{E_0} \sum_{z_s > z_{s_i}} n_s \left[W_y^{\text{dip}}(z_s - z_{s_i}) y_s + W_y^{\text{quad}}(z_s - z_{s_i}) y_i \right], \\ \Delta\delta_i &= -\frac{e^2}{E_0} \sum_{z_s \geq z_{s_i}} n_s W_{||}(z_s - z_{s_i}).\end{aligned}\tag{3.1}$$

In the above expressions, e is the elementary charge, E_0 the beam energy, s_i the slice containing the macro-particle i , z_s the longitudinal position of each slice, (x_s, y_s) the average offsets from the beam orbit and n_s the number of particles in each slice s . The transverse wake functions W_x and W_y are expressed as the sum of dipolar and quadrupolar components, and are provided in the input in the form of a table.

Once the transverse kick is given to a macro-particle, the code transports the macro-particle to the next interaction point using linear optics and including effects like chromaticity and amplitude detuning.

The goal of this study is to assess a transverse impedance budget for the high frequency part of the impedance, generally modeled as a broad-band resonator and responsible for single bunch effects. Since the bunches have low transverse emittances and are much shorter than the buckets, it is legitimate to assume in the HEADTAIL simulations no amplitude detuning and a linearized RF bucket. The effect of space charge is neglected.

3.3 Transverse impedance budget

3.3.1 Impedance model with a broad-band resonator

Zero chromaticity

The accuracy of the instability thresholds depends on that of the impedance modeling of the DR. For that purpose, a detailed design of the most significant machine components would be required. However, as only a conceptual design of these components is available [6], approximate instability threshold estimates would be desirable.

The first step is to assume that the whole ring is modeled as a broad-band resonator (BBR). The transverse broad-band impedances and wake functions are given by the following expressions [29, 30]

$$Z_{\perp}(\omega) = Z_x(\omega) = Z_y(\omega) = \frac{\omega_r}{\omega} \frac{R_s}{1 - iQ \left(\frac{\omega_r}{\omega} - \frac{\omega}{\omega_r} \right)}, \quad (3.2)$$

$$W_{\perp}(\tau) = W_x(\tau) = W_y(\tau) = \frac{\omega_r^2 R_s}{Q \omega_r} e^{-\frac{\omega_r}{2Q} \tau} \sin(\bar{\omega}_r \tau),$$

where R_s is the transverse shunt impedance in units of (Ω/m), $\omega_r = 2\pi f_r$ the cut-off angular frequency of the beam chamber and $\bar{\omega}_r = \omega_r \sqrt{1 - \frac{1}{4Q^2}}$. For the DR study, we assume $f_r = 5$ GHz and $Q = 1$, while R_s is the parameter scanned in HEADTAIL simulations.

Table 3.1: CLIC DR parameters used in simulation.

Energy [GeV]	2.86
Norm. trans. emitt.(x,y)[nm]	500, 5
Bunch length [mm]	1.8
Momentum spread	1.07×10^{-3}
Bunch spacing [ns]	1
Bunch population	4.1×10^9
Circumference [m]	427.5
Mom. compact. factor	1.3×10^{-4}
Tunes (x,y,z)	48.35, 10.4, 0.0057
Energy loss per turn [MeV]	3.98
Damping times (x,y,z)[ms]	2, 2, 1
RF frequency [GHz]	1
RF voltage [MV]	5.1
Wiggler length [m]	2
Wiggler field [T]	2.5
Number of wigglers	52
Wiggler half gap [mm]	6
Average beta functions (x,y) [m]	3.475, 9.233

The value of the single bunch current is assumed to be the designed one [31]. This study allows

Chapter 3. Transverse impedance budget of the CLIC DR

the calculation of the available transverse impedance budget that ensures safe operation with the designed bunch current. The parameters of the CLIC DRs that were used in HEADTAIL simulations are summarized in Table 3.1 above, assuming one scenario for the RF frequency, the one of 1 GHz [32–34].

In the transverse plane, a strong head-tail instability or Transverse Mode Coupling Instability (TMCI) can occur and cause rapid beam loss. In the case of a round beam and axisymmetric geometry for a short bunch, i.e. when $\frac{\sigma_z \omega_r}{c} \ll 1$, there is a criterion to find the threshold of TMCI [35, 36]

$$\frac{R_s [k\Omega/m] f_r^2 [\text{GHz}]}{Q} \leq 0.6 \frac{E [\text{GeV}] Q_s}{\langle \beta_{x,y} \rangle [\text{m}] Q_b [\text{C}] \sigma_t [\text{ps}]}, \quad (3.3)$$

where R_s is the transverse shunt impedance, $f_r = \omega_r / 2\pi$ the resonant frequency and ω_r the resonant angular frequency of the resonator assumed to be the cut-off frequency of the beam pipe, Q is the quality factor, $\langle \beta_{x,y} \rangle$ the average beta values in the transverse plane, $Q_b = Ne$ the bunch charge and $\sigma_t = \sigma_z / \beta c$ is the rms bunch length. Using the parameters of Table 3.1, Eq.(3.3) translates into a threshold of 10.7 M Ω /m in the vertical plane, assuming a BBR with $Q = 1$, $f_r = 5$ GHz, $\sigma_t = 6$ ps, $Q_b = 6.56 \times 10^{-10}$ C and $\langle \beta_y \rangle = 9.233$ m. The prediction for the x plane using Eq.(3.3) with $\langle \beta_x \rangle = 3.475$ m is 28 M Ω /m.

HEADTAIL code gives the evolution of the bunch centroid over several turns for different transverse shunt impedance values. The values are swept during simulations from 0 up to 20 M Ω /m with a step of 1 M Ω /m. In Figure 3.1, the centroid horizontal position is plotted as a function of time for different values of the transverse shunt impedance $R_s = 10, 15, 16, 17, 18$ and 19 M Ω /m. It can be seen that for $R_s = 18$ M Ω /m the beam is unstable. The vertical centroid for $R_s = 5, 6, 7$ and 8 M Ω /m is plotted in Figure 3.2. In the vertical plane, the beam becomes unstable at 7 M Ω /m.

The behavior of the transverse modes is also analyzed in the frequency domain by applying the Sussix algorithm [37–39] on the coherent bunch motion for each value of the transverse shunt impedance. By applying this frequency analysis to the bunch coherent oscillations, the spectrum of the bunch modes can be obtained. The relative tune shift $(Q - Q_{x,y}) / Q_s$ with respect to the zero-current tune $Q_{x,y}$ is normalized to the synchrotron tune Q_s to identify each of the bunch azimuthal modes. The lines in the bunch centroid spectrum represent the natural coherent oscillation frequencies of the bunch, i.e. its oscillation modes.

The tune shift is plotted, for zero chromaticity, as a function of the transverse shunt impedance in Figure 3.3 for both planes. Modes 0 and -1 are observed to shift with increased R_s and couple for impedance values of about 18 M Ω /m and 7 M Ω /m in the horizontal and vertical plane respectively, causing a TMCI. Both values in the transverse plane are about 34% lower than that naively calculated with the analytical formula (3.3). The difference in the impedance thresholds in the two planes is explained by the difference in the average beta values over the DR used in the simulation for the BBR. In fact, $\langle \beta_x \rangle = 3.475$ m and $\langle \beta_y \rangle = 9.233$ m. The effect of the impedance, simulated by kicks at a certain point of the ring, is proportional to the macro-particles offset and therefore to the $\langle \beta_{x,y} \rangle$. The effect on the tune of a kick at a certain

3.3. Transverse impedance budget

point with $\langle \beta_{x,y} \rangle$ is proportional to the $\langle \beta_{x,y} \rangle$ from $\Delta Q = \frac{1}{4\pi} \oint \beta_{x,y}(s) \Delta K(s) ds$. Therefore in the vertical plane, the impedance has an effect higher by a factor of 2.7 compared to the horizontal plane and the TMCI threshold is smaller by almost the same fraction, 2.6.

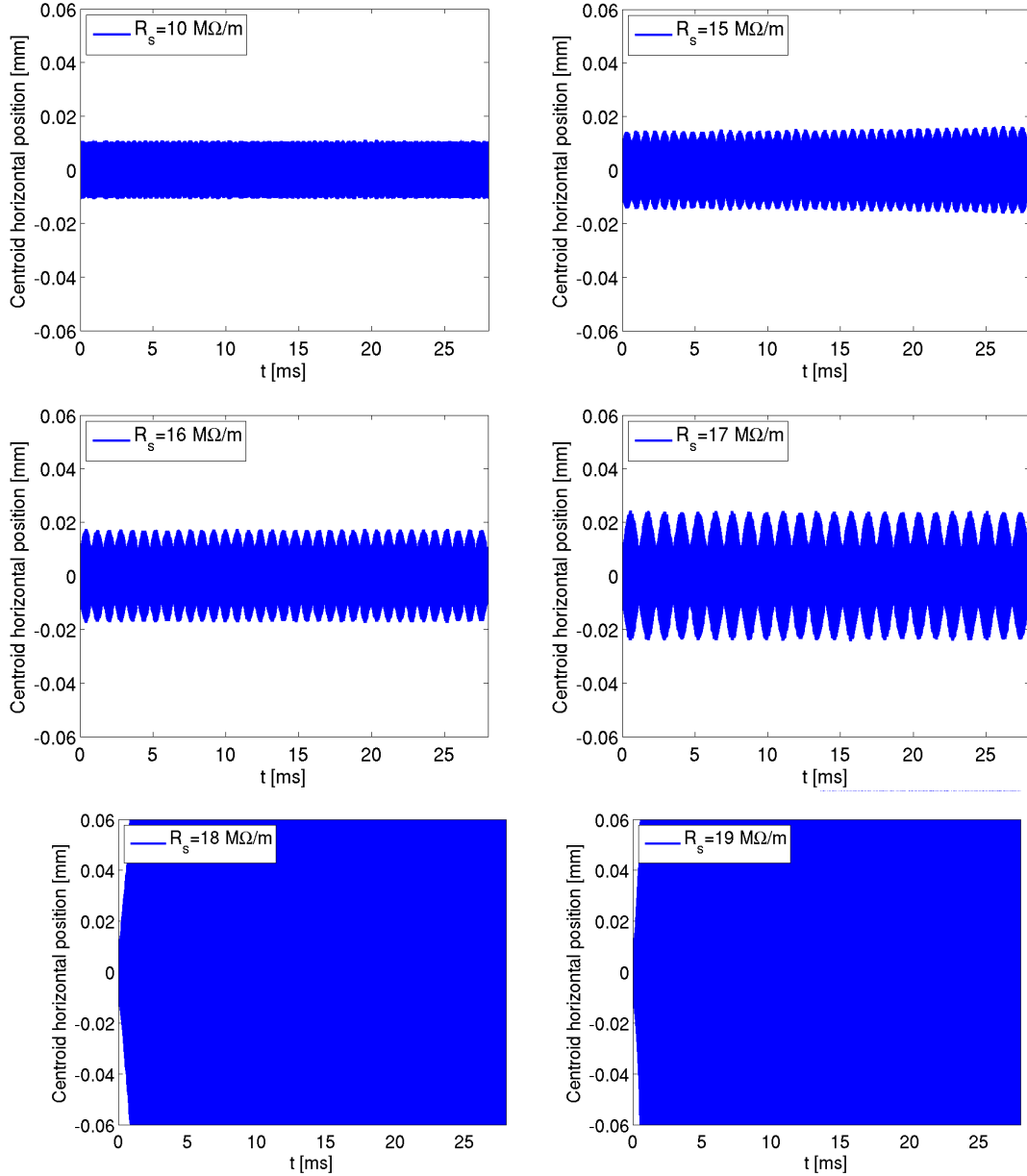


Figure 3.1: Coherent horizontal motion of the bunch centroid as a function of time simulated with HEADTAIL (see parameters in Appendix A.1). The value of the transverse shunt impedance is increased from left to right to identify the instability threshold which was estimated between 17 and 18 MΩ/m.

Chapter 3. Transverse impedance budget of the CLIC DR

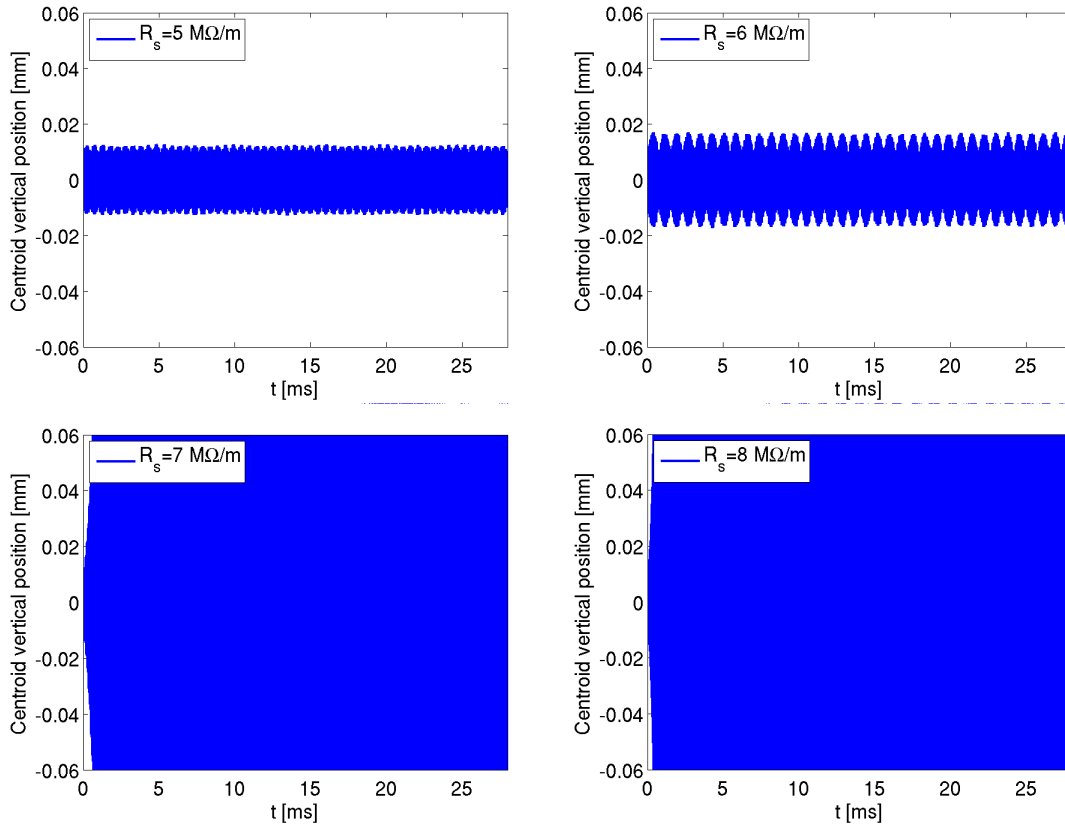


Figure 3.2: Coherent vertical motion of the bunch centroid as a function of time simulated with HEADTAIL (parameters in Appendix A.1). The value of the transverse shunt impedance is increased from left to right to identify the instability threshold which was found between 6 and 7 MΩ/m.

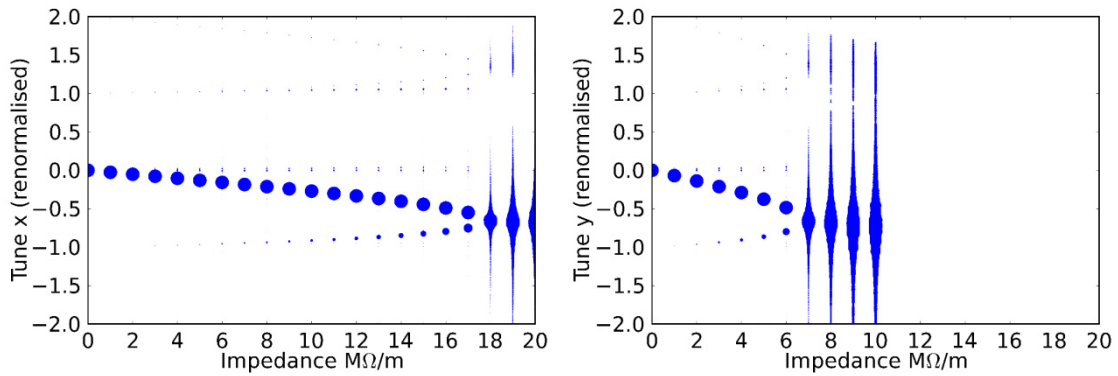


Figure 3.3: Mode spectrum of the horizontal (left) and vertical (right) coherent motion at zero chromaticity, as a function of the transverse shunt impedance. A TMCI is observed at 18 MΩ/m and 7 MΩ/m respectively.

Positive and negative chromaticity

Chromaticity is believed to raise the TMCI threshold due to the tune spread that it causes and because it locks the coherent modes to their low intensity values, making mode coupling potentially appear at higher impedance values. Simulations were done for different positive and negative values of chromaticity to study this effect as shown in Figure 3.4.

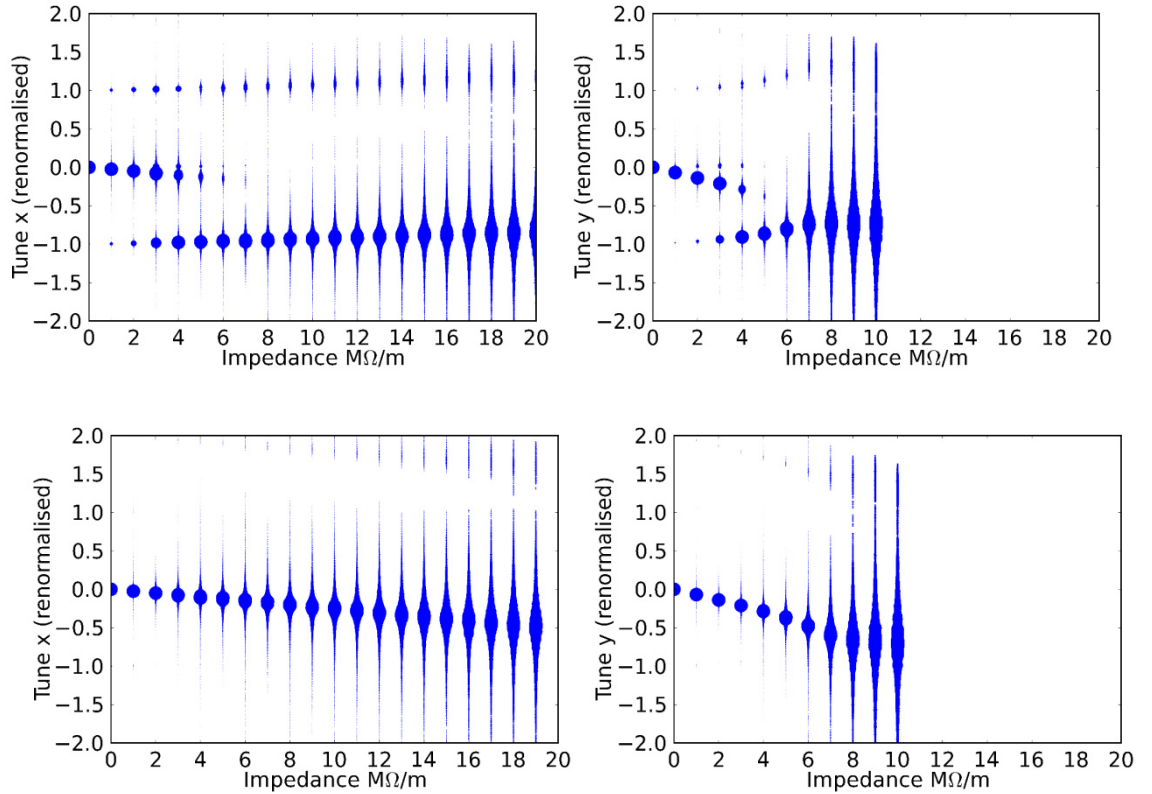


Figure 3.4: Mode spectrum of the horizontal (left) and vertical (right) coherent motion as a function of the transverse shunt impedance, for chromaticity $\xi = 0.02$ (top) and $\xi = -0.02$ (bottom). The parameters of the simulation can be found in Appendix A.2.

As expected, the presence of chromaticity causes the modes to move less and not to merge and consequently to avoid a TMCI, but another type of instability, the head-tail instability, occurs. In Figure 3.4, it is observed that in the case of positive chromaticity, modes $m = \pm 1$ get excited whereas $m = 0$ is damped, showing that while a TMCI can be avoided, a head-tail instability develops on a single mode. For negative chromaticity, mode $m = 0$ becomes unstable. This was expected, as the DR is operating above transition.

A TMCI quickly becomes very fast above the threshold for instability, and therefore the natural damping mechanism will not change the threshold significantly. Meanwhile, in the case of head-tail instability the calculation of its rise time is needed along with the comparison to the damping time (given in Table 3.1). If the rise time is lower than the damping time of

Chapter 3. Transverse impedance budget of the CLIC DR

2 ms, the instability is faster than the damping mechanism. Therefore, it is necessary to find for which maximum value of the shunt impedance the rise time is higher than 2 ms, so that the damping mechanism can suppress the instability. Plotting the rise time of the instability for each value of the transverse shunt impedance in Figure 3.5, the instability threshold is estimated at 6.5 M Ω /m and 6 M Ω /m in the horizontal and vertical plane respectively.

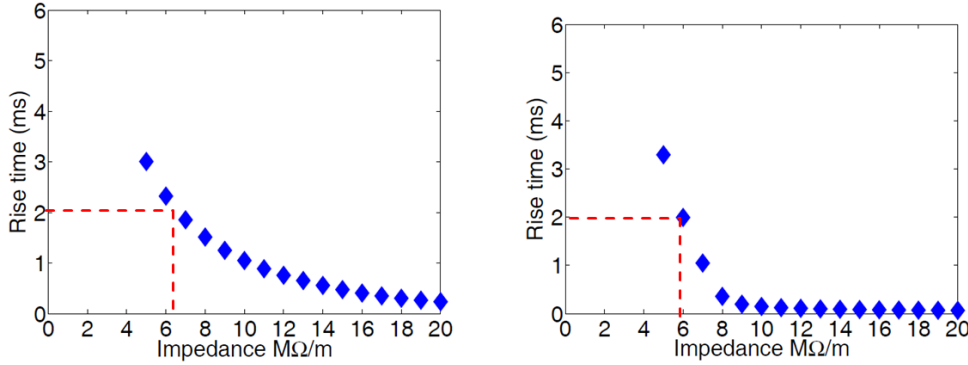


Figure 3.5: Rise time in the horizontal (left) and vertical (right) plane for positive chromaticity $\xi_{x,y} = 0.02$. Damping time is 2 ms in both planes, therefore the remaining budget is below 6.5 M Ω /m in x and 6 M Ω /m in the y plane.

Following the same procedure, various values of chromaticity were simulated, both positive and negative. The results for the available impedance budget can be found in Table 3.2.

Table 3.2: Available impedance budget for various positive and negative chromaticity values.

$\xi_{x,y}$	Q'_x/Q'_y	Threshold in x [M Ω /m]	Threshold in y [M Ω /m]
0.02	0.8/0.2	6	5
0.05	2.7/0.6	4	4
0.09	4.4/0.9	2	2
0.3	14.5/3.12	$\gg y$	1
0.6	29/6.24	$\gg y$	2
0.9	43.5/9.36	$\gg y$	5
-0.02	-0.8/-0.2	4	5
-0.05	-2.7/-0.6	2	2
-0.09	-4.4/-0.9	2	2

The instability thresholds are even lower for slightly positive or negative chromaticity compared to 18 M Ω /m and 7 M Ω /m for zero chromaticity. Lower instability thresholds translate into a lower impedance budget for the DR. The goal, therefore, would be to operate at zero chromaticity which has also the advantage to allow for a larger impedance budget. However, since chromaticity will be certainly slightly positive, lower impedance budget than that given by TMCI has to be considered. Therefore, the impedance budget is estimated to be not more than 4 M Ω /m in both transverse planes.

3.3.2 Impedance model with a broad-band resonator and resistive wall

Resistive wall contributions

A dominant contributor in the CLIC DR impedance model will be given by the resistive wall impedance of the machine vacuum chambers. The classic thick wall formula for the transverse dipolar impedance of an axisymmetric infinitely long structure is given by the expression [40, 41]

$$Z_x^{dip} \approx (1 + j) \frac{L Z_0 \delta_s}{2\pi b^3}, \quad (3.4)$$

where L is the length of the element, $\delta_s = \sqrt{\frac{2}{\mu_0 \mu_r \sigma_{DC} \omega}}$ [42] is the skin depth of the material of the inner layer and b the beam pipe radius. It is evident from Eq.(3.4) that the main parameters affecting the impedance are the radius b , the length L and the resistivity $\rho_{DC} = \frac{1}{\sigma_{DC}}$ of the inner material.

In the DRs, the resistive wall in the wiggler sections with 6 mm vertical half gap is expected to be a strong impedance source. Because of the small aperture, compared to 9 mm for other parts of the ring, the contribution of the wigglers is expected to take a significant fraction of the available impedance budget [31]. Moreover, layers of coating materials, which are necessary for e-cloud mitigation or good vacuum, can significantly increase the resistive wall impedance especially in the high frequency regime. The materials considered are stainless steel (StSt) and copper (Cu) for the vacuum pipe. As coating materials, amorphous carbon (aC) used for electron cloud mitigation [43–45], and Non-Evaporated Getter (NEG) used for good vacuum [46], were chosen. It is common strategy to use coating materials in accelerators to suppress some undesired collective effects. However, the use of coating does not come for free and its impact on the impedance budget should be investigated.

DR lattice

The transverse wake functions for the resistive wall contributions are calculated with the ImpedanceWake2D package used for multilayer axisymmetric or flat structures. But first the different contributions had to be singled out from the DR lattice design.

The role of the CLIC DR is to provide the final stage of damping, in order to produce the required ultra-low emittances at a high bunch intensity, following the luminosity requirements of the collider. The high bunch density and the large brightness of the beam, trigger a number of collective effects, with intrabeam scattering being the main limitation to the ultra-low emittance. An optimized lattice with reduced intrabeam scattering emittance blow up and space charge tune shift was designed, achieving the requirements of the collider and an adequate dynamic aperture [47].

The lattice has a racetrack shape with 2 arcs, consisting of low-emittance Theoretical Minimum Emittance (TME) cells and two long straight sections with FODO structure, to accommodate

Chapter 3. Transverse impedance budget of the CLIC DR

the damping wigglers, RF cavities, as well as, injection and extraction equipment. There are 13 FODO cells per straight section with two wigglers per cell, thus 52 wigglers of 2.5 T peak field, 6 mm half gap, flat geometry [48] and $\langle \beta_x \rangle = 4.200$ m, $\langle \beta_y \rangle = 9.839$ m. Wigglers occupy 1/4 of the total circumference and are expected to be an important impedance contribution due to the very small radius. The total length of the arcs is 270.2 m with 9 mm radius beam pipe, round geometry and $\langle \beta_x \rangle = 2.976$ m, $\langle \beta_y \rangle = 8.829$ m. Last, the rest of the FODO cell is considered a separate contribution from the wigglers due to the different chamber geometry (round) and radius of 9 mm but also different beta functions compared to the arcs ($\langle \beta_x \rangle = 5.665$ m, $\langle \beta_y \rangle = 8.582$ m). The full ring optics is shown in Figure 3.6, while the DR layout is sketched in Figure 3.7.

The chamber along the whole ring is simulated as a two-layer structure made of StSt ($\sigma_{DC} = 1.45 \times 10^6$ S/m) and coated with $2 \mu\text{m}$ of NEG ($\sigma_{DC} = 1 \times 10^6$ S/m) or $1 \mu\text{m}$ of aC ($\sigma_{DC} = 1 \times 10^3$ S/m). Chapter 4 is devoted to the characterization of NEG properties at high frequencies.

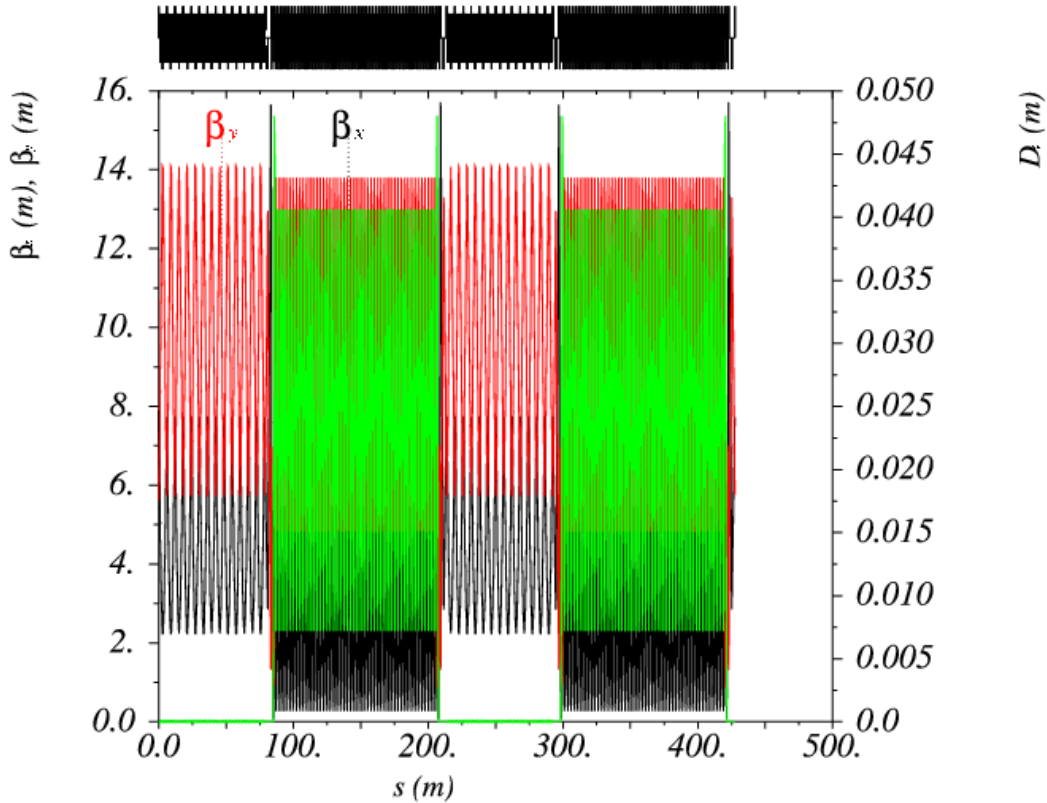


Figure 3.6: Optics functions of the CLIC DR.

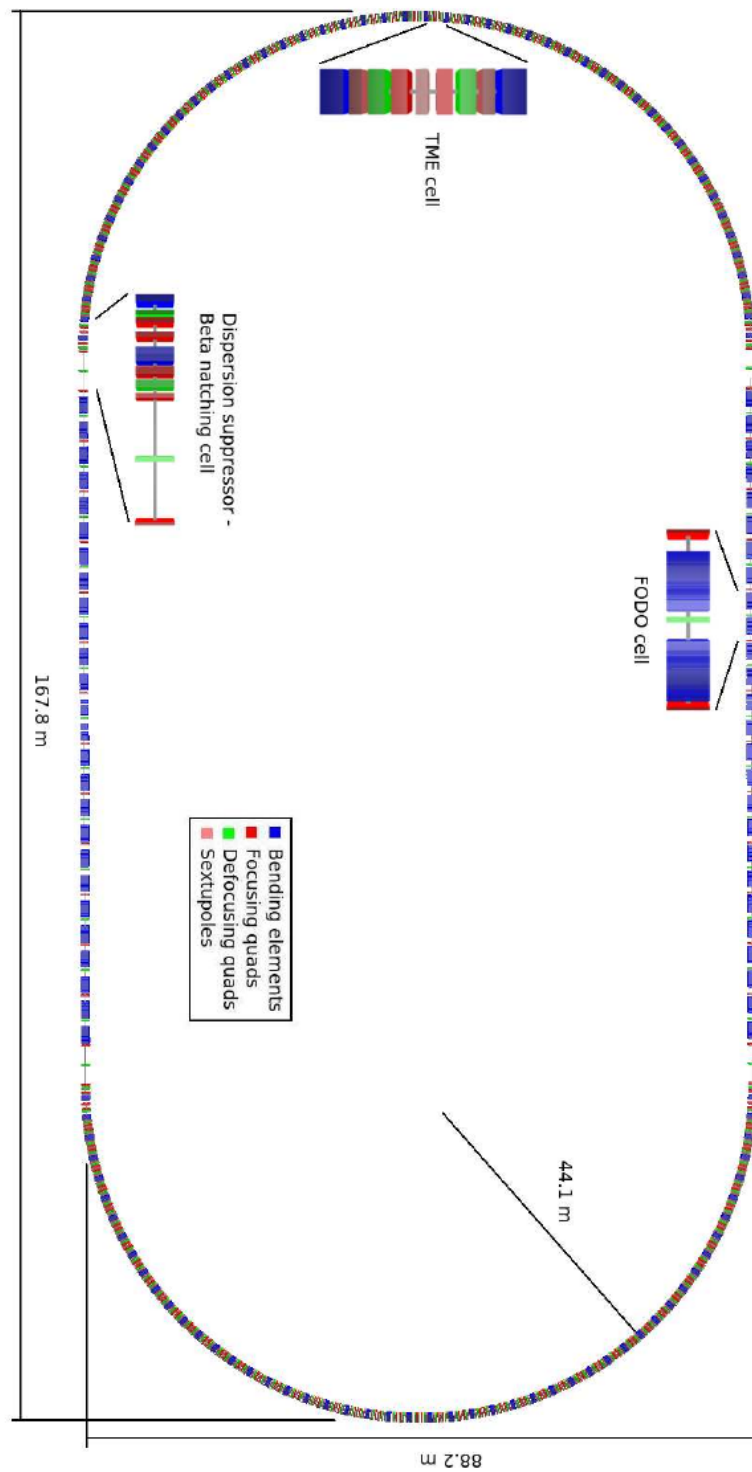


Figure 3.7: Damping ring layout.

NEG coating

The total transverse wake model summing the three wall contributions (dipolar and quadrupolar terms) of the arcs, wigglers and the rest of the FODO cell weighted by the average beta functions $\left(\frac{1}{\langle \beta_{x,y} \rangle} \sum \langle \beta_{x,y} \rangle_i Z_i^{\text{dip or quad}}(\omega)\right)$, plus the dipolar broad-band model (for a transverse shunt impedance of 5 MΩ/m and weighted also by the average beta functions) is shown in Figure 3.8 for the NEG coating case (ImpedanceWake2D parameters are listed in Appendices B.1, B.2, B.3).

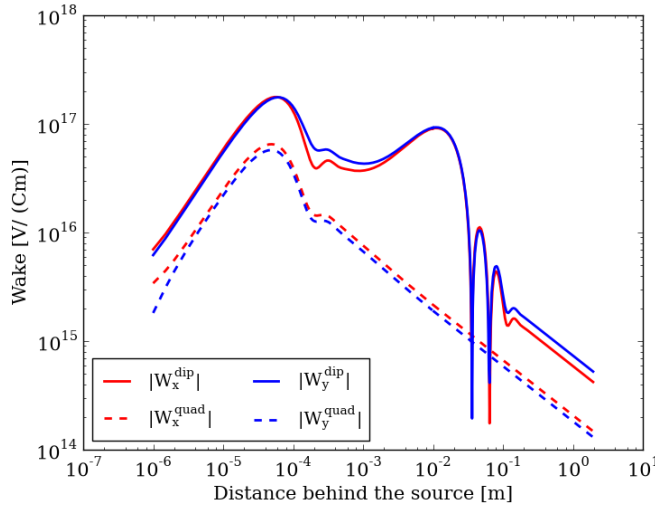


Figure 3.8: Transverse wake function model of the electron DR with 2 μm NEG coating.

For 0 chromaticity, the relative tune shift with respect to the zero-current tune and normalized to the synchrotron tune Q_s is plotted as a function of the transverse shunt impedance in Figure 3.9.

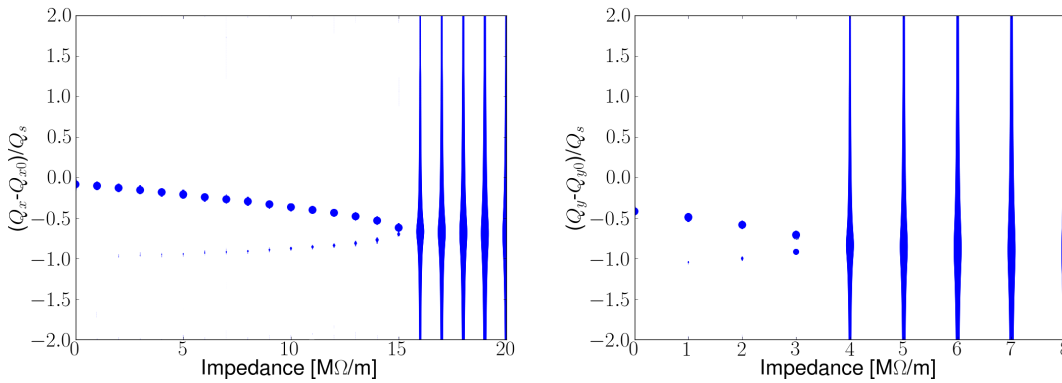


Figure 3.9: Mode spectrum of the x (left) and y (right) coherent motion for 0 chromaticity, as a function of R_s . A TMCI is observed at 16 MΩ/m and 4 MΩ/m in x and y plane respectively.

3.3. Transverse impedance budget

Modes 0 and -1 are observed to move and couple at $16 \text{ M}\Omega/\text{m}$ and $4 \text{ M}\Omega/\text{m}$ in the horizontal and vertical plane respectively. The vertical plane, which is the most critical one, would therefore indicate that the remaining transverse impedance budget is $4 \text{ M}\Omega/\text{m}$ at operation with zero chromaticity, once the resistive wall impedance is explicitly included in the model.

Examining now the slightly positive chromaticity, a head-tail instability develops which can be detected as a higher order mode, $m = -1$, gets excited whereas 0 mode is damped. The mode spectrum as a function of the impedance is shown in Figure 3.10. The instability threshold is $2 \text{ M}\Omega/\text{m}$ for the horizontal and $1 \text{ M}\Omega/\text{m}$ for the vertical plane by comparing the rise times to the damping time in Figure 3.11.

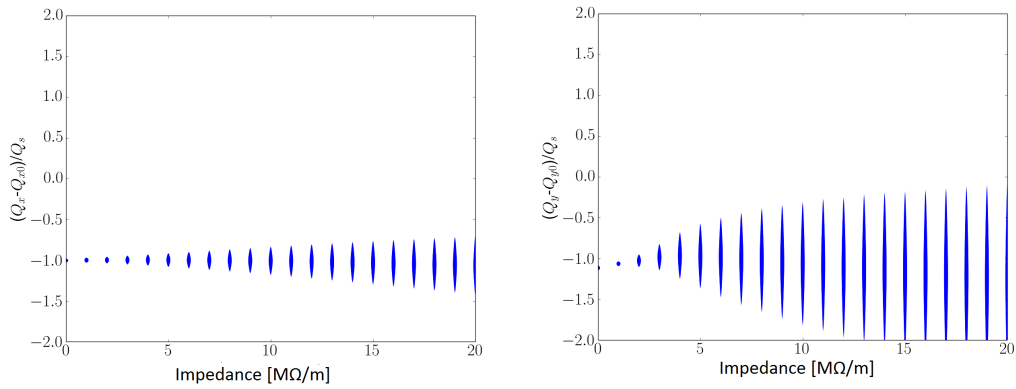


Figure 3.10: Mode spectrum of the x (left) and y (right) coherent motion for positive chromaticity $\xi_{x,y} = 0.02$, as a function of R_S .

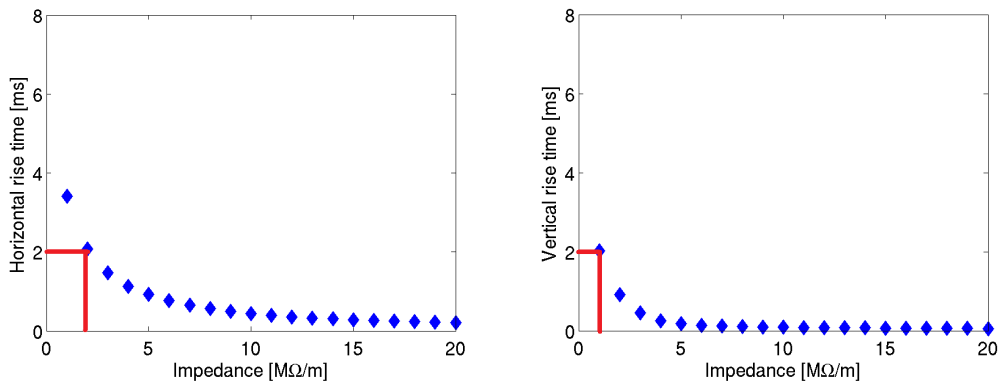


Figure 3.11: Rise time in the x (left) and y (right) plane for positive chromaticity $\xi_{x,y} = 0.02$. Damping time is 2 ms in both planes, therefore the remaining budget is below $2 \text{ M}\Omega/\text{m}$ in x and $1 \text{ M}\Omega/\text{m}$ in y.

aC coating

Coating the vacuum pipe with aC is an option against electron-cloud effects for the positron damping rings. Consequently, the impedance budget has to be estimated also for a uniform $1 \mu\text{m}$ aC coating.

The resistive wall is estimated as previously described in the NEG coating subsection, but now considering the aC conductivity, $\sigma_{\text{DC}} = 1 \times 10^3 \text{ S/m}$, for the wake calculations. A broadband resonator is also included in the impedance model with $Q = 1$, $f_r = 5 \text{ GHz}$ and the shunt impedance is scanned in the simulation process. The total transverse wake model with the three wall contributions (dipolar and quadrupolar terms) of the arcs, wigglers and the rest of the FODO cell plus the broad-band model (for a transverse shunt impedance of $5 \text{ M}\Omega/\text{m}$) is shown in Figure 3.12.

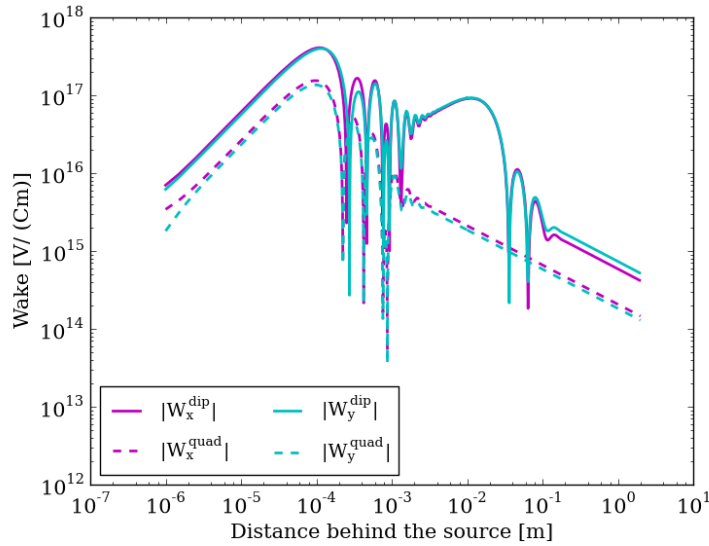


Figure 3.12: Transverse wake function model of the positron DR with $1 \mu\text{m}$ aC coating.

In Figure 3.13 the mode spectrum results are provided for the transverse plane in the case of 0 chromaticity. TMCI is found at $14 \text{ M}\Omega/\text{m}$ and $4 \text{ M}\Omega/\text{m}$ in the horizontal and vertical plane respectively, leading to the same budget in the vertical plane as for the electron DR with $2 \mu\text{m}$ NEG coating. For positive chromaticity, the mode spectrum is shown in Figure 3.14. Comparing the rise time to the 2 ms damping time in the transverse plane, the budget is estimated at $2 \text{ M}\Omega/\text{m}$ and $1.5 \text{ M}\Omega/\text{m}$ in the horizontal and vertical plane respectively. The transverse impedance budget results for the aC coating are very similar to the ones for NEG coating. The coating thickness does play a role and it should be noted that the results presented are for aC thickness of $1 \mu\text{m}$ and $2 \mu\text{m}$ of NEG.

3.4. Effect of coating thickness and properties at high frequencies

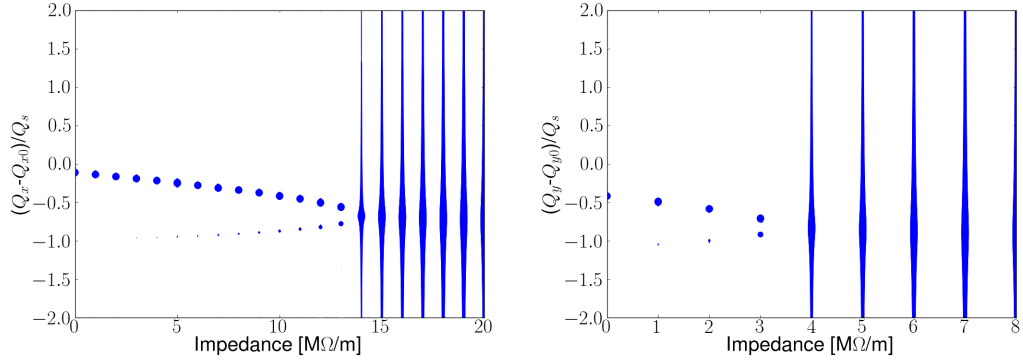


Figure 3.13: Mode spectrum of the horizontal (left) and vertical (right) coherent motion for 0 chromaticity, as a function of impedance. TMCI thresholds are at 14 and 4 MΩ/m for x and y plane.

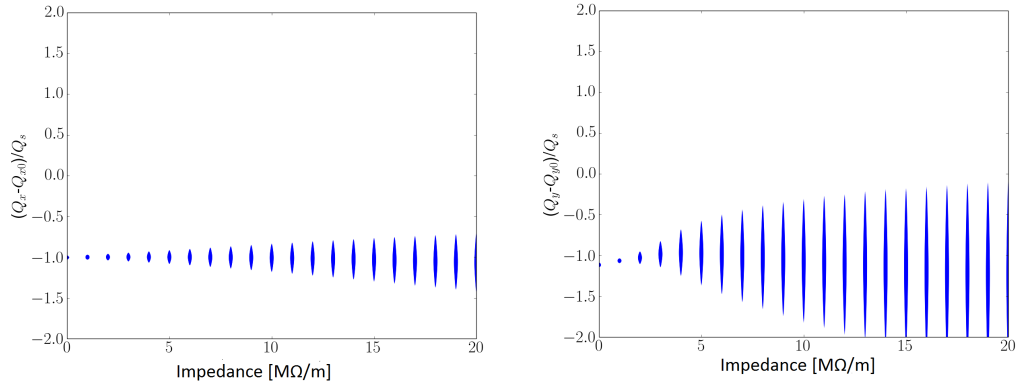


Figure 3.14: Mode spectrum of the horizontal (left) and vertical (right) coherent motion for positive chromaticity $\xi_{x,y} = 0.02$, as a function of the transverse shunt impedance.

3.4 Effect of coating thickness and properties at high frequencies

Since the DR are still under design, it is interesting to investigate the effect of coating thickness and different materials, with emphasis on high frequencies. Moreover, since the NEG conductivity is not well characterized at high frequencies, the effect of different properties is also of interest.

In order to investigate this, simulations of the vertical impedance were done with ImpedanceWake2D. Wigglers, due to the short aperture and the total length of 104 m, are the dominant contribution to the total resistive wall impedance. The NEG thickness usually varies between 1-2 μm while aC is usually between 0.5-1 μm . The generalized impedance for the various possible thicknesses and for coating of NEG or aC on a StSt vacuum chamber are plotted in Figure 3.15. The parameters of ImpedanceWake2D can be found in Appendix B.4 and B.5. The choice of NEG or aC coating seems to have an effect above 10 GHz, while at lower frequencies, coating is transparent. NEG behaves in a similar way for 1 or 2 μm thickness as can be clearly

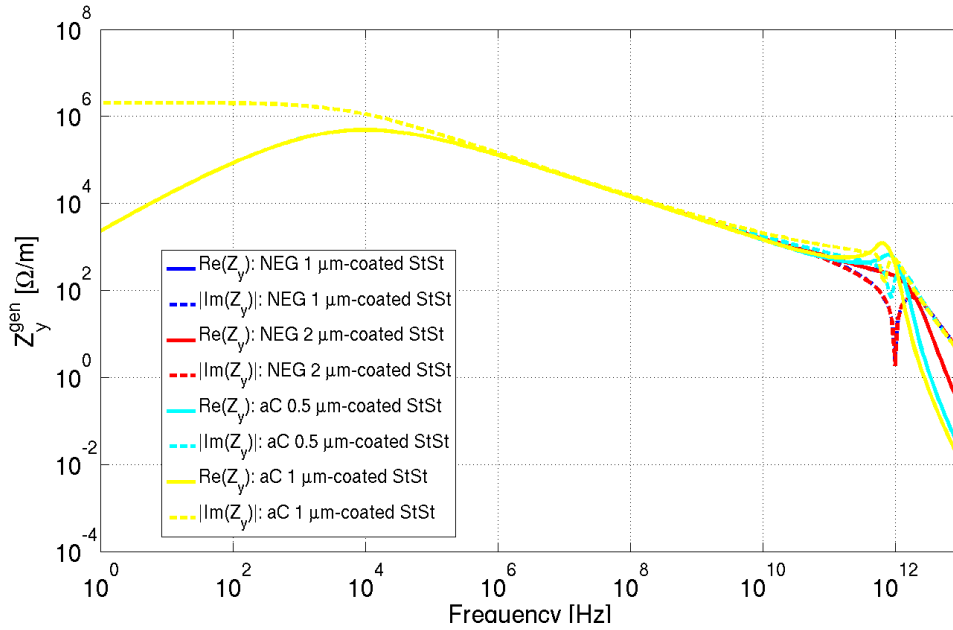


Figure 3.15: Generalized vertical impedance of the DR wigglers for various coating thicknesses and materials. The choice of material as well as thickness plays a role above 10 GHz.

seen in Figure 3.16, on the left. Therefore both coating thickness values are acceptable. On the other hand, there is a difference observed for aC, in Figure 3.16 on the right.

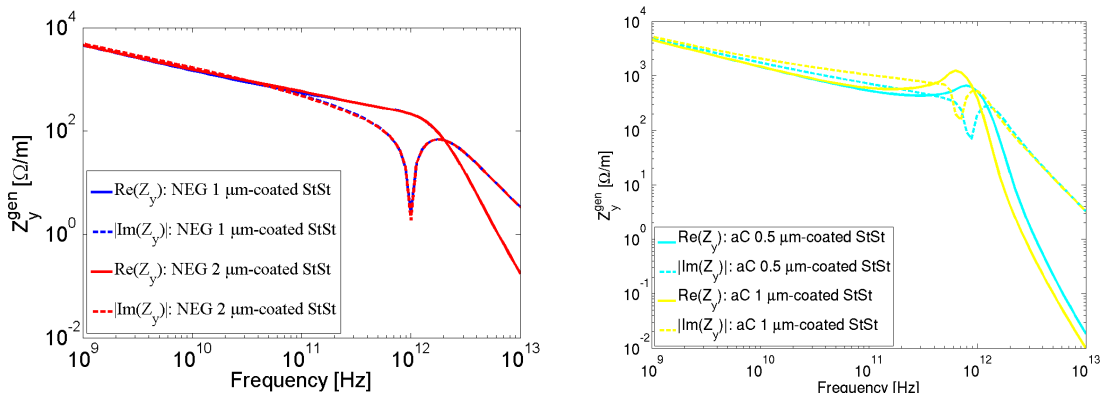


Figure 3.16: Generalized vertical impedance of the wigglers for NEG (left) or aC (right) on StSt chamber of various thicknesses.

Looking in more detail in the imaginary part of the wiggler’s impedance for aC coating in Figure 3.17, the impedance is larger for 1 μm of aC. A higher imaginary impedance would cause a stronger tune shift effect, and lead to a different coupling threshold (probably lower). Therefore, making the aC layer as thin as possible should be certainly recommended.

3.4. Effect of coating thickness and properties at high frequencies

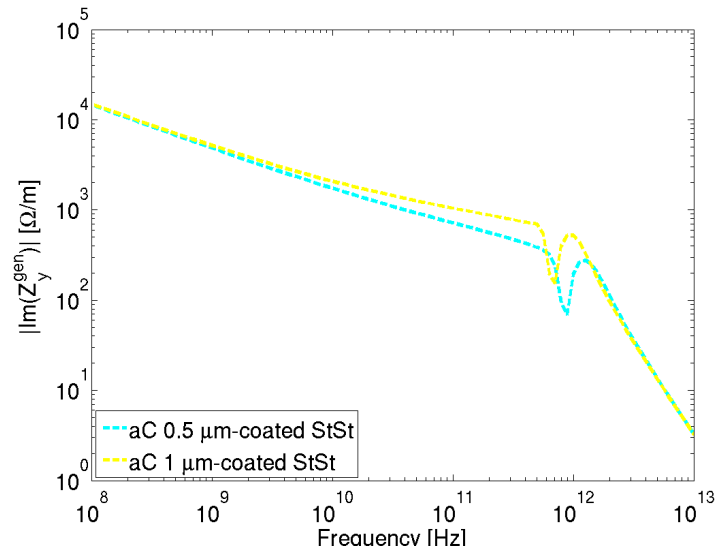


Figure 3.17: Imaginary vertical impedance for aC coating of 0.5 or 1 μm thickness.

It is also unknown how much an error in the material conductivity value can affect the impedance calculations up to high frequencies. For this reason, another simulation was done using ImpedanceWake2D, fixing the NEG thickness at 2 μm . The imaginary impedance is calculated for NEG conductivity of 1×10^5 S/m, 0.6×10^6 S/m, 1×10^6 S/m and 2×10^6 S/m. The results are plotted in Figure 3.18.

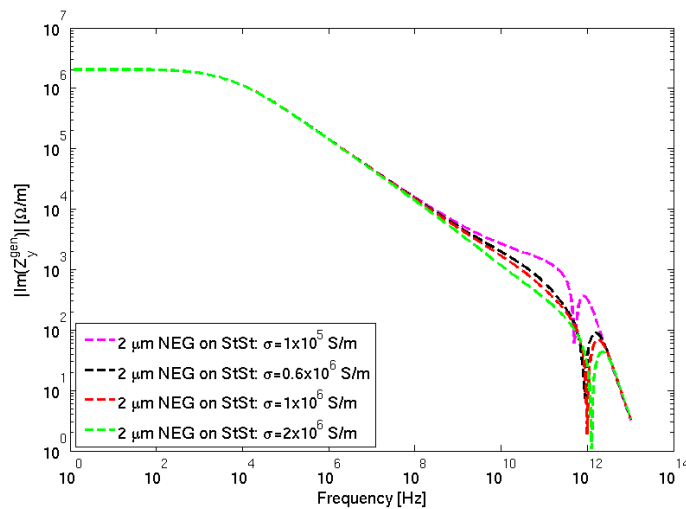


Figure 3.18: Absolute imaginary vertical impedance for 2 μm NEG coating for different conductivities. Above 1 GHz, the effect becomes significant.

The knowledge of material properties is important at high frequencies, since the impedance is different above 1 GHz for various conductivities. A miscalculated impedance, can result in a modeled tune shift error (underestimate or overestimate). The above simulation validated the

motivation to search for a method to characterize NEG properties at high frequencies. The method and the obtained results are discussed in detail in Chapter 4.

3.5 Injection and extraction kickers

Kickers are required to inject the beam into and extract it from the PDRs, as well as, the DRs. The PDR and DR kicker design is very challenging due to its requirement of excellent field homogeneity, high stability and reproducibility of the field, ultra-high vacuum, very small jitter and low longitudinal and transverse beam coupling impedances. In particular, the DR extraction kicker has the most demanding specification for field homogeneity.

Jitter in the magnitude of the kick waveform would cause a beam jitter at the interaction point [49]. For this reason, the PDR and DR kickers, but especially the DR extraction kicker, must have a very small magnitude of jitter as well as low longitudinal and transverse beam coupling impedances. In order to fulfill the tight requirements for the excellent field homogeneity and the very low beam coupling impedances, striplines were chosen as kicker elements [50]. A stripline kicker consists of two parallel metallic electrodes which are connected at each end to the external circuit by coaxial feedthroughs. The specifications of the DR kickers are gathered in Table 3.3 [51].

Table 3.3: CLIC DR kicker parameters.

Field rise and fall times [ns]	700
Pulse flat-top duration [ns]	160
Pulse flat-top reproducibility	$\pm 1 \times 10^{-4}$
Flat-top stability (injection)	$\pm 2 \times 10^{-3}$
Flat-top stability (extraction)	$\pm 2 \times 10^{-4}$
Injection field uniformity [%]	± 0.1
Extraction field uniformity [%]	± 0.01
Repetition rate [Hz]	50
Stripline and load impedance [Ω]	50
Pulse voltage per stripline [kV]	± 12.5
Stripline pulse current [A]	± 250
Length [m]	1.7
Vacuum [mbar]	10^{-10}

Optimization studies of the DR stripline kicker have been carried out [52]. The geometric cross-section of the striplines defines the field homogeneity and the characteristic impedance. Different electrode shapes have been studied for the extraction kickers: flat, curved and half-moon electrodes [53, 54]. Half-moon electrodes were selected as the optimum shape due to adequately good impedance matching and excellent field homogeneity [54]. Once the electromagnetic design of the striplines, including electrode supports and feedthroughs, had been completed, a prototype of the extraction stripline kicker for the CLIC DR was manufactured by Trinos Vacuum Projects (Valencia, Spain). The prototype kicker can be seen in Figure 3.19 [55]. The pipe enclosing the 1.639 m long electrodes is made from StSt with a length of 1.712 m. The

pipe diameter is 40.5 mm and the electrodes are made from Al.

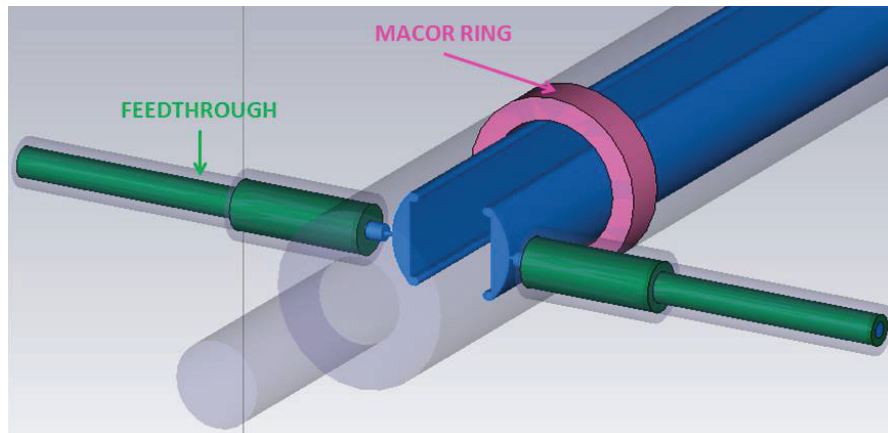


Figure 3.19: CLIC stripline kicker prototype.

The stripline kicker is another candidate of significant impedance source, that should be considered in the beam dynamics simulations with HEADTAIL. In order to calculate the wake function in this geometry, the CST Particle Studio is used, since analytical approach is limited for such complex geometry. A simplified 3D model is first tested for the calculation of transverse dipolar and quadrupolar impedance components. The simplified model is created with CST and is shown in Figure 3.20.

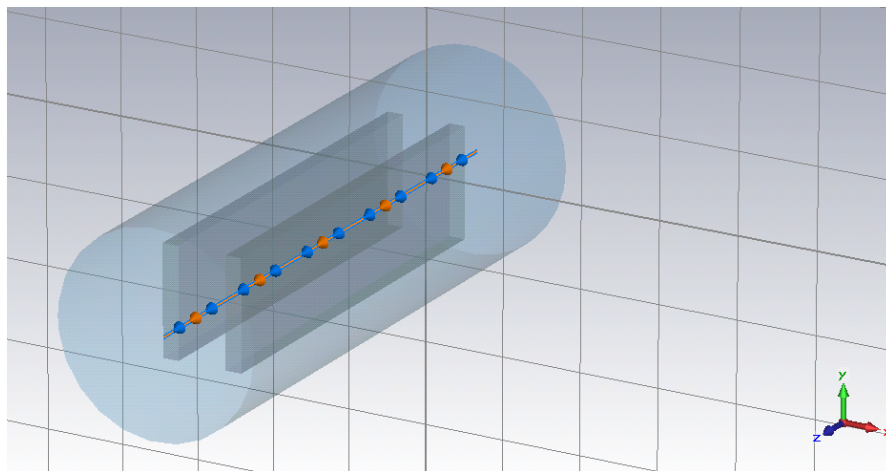


Figure 3.20: Simplified stripline kicker 3D model with CST.

The kicker's length has been reduced to 140 mm, in order to reduce the number of mesh cells, and 100 mm is the length of the electrodes. Two electrodes from PEC are located inside a vacuum chamber of 25 mm radius. The height of the electrodes is 27 mm, the distance between them 12 mm and their thickness is 4 mm. The electrodes' height is increased to include the edges of the half-moon electrodes.

An ultra short bunch of 0.2 mm is necessary for the wake function calculation with CST. For this simulation setup and for 10 lines per wavelength, the number of mesh cells is ~ 5 billions.

Chapter 3. Transverse impedance budget of the CLIC DR

Use of symmetries, electric $E_t = 0$ in YZ plane and magnetic $H_t = 0$ in XZ, reduces the number to ~ 1.3 billions. However, such large number of mesh points prevents the realization of the simulation, even with the use of a cluster.

The number of mesh points can be reduced if less lines per wavelength are used. For example, 3 lines per wavelength reduces the number of mesh cells to ~ 142 millions. Despite that, a convergence study revealed that simulation with fewer lines per wavelength than 10, cannot provide trustworthy results, as shown in Figure 3.21.

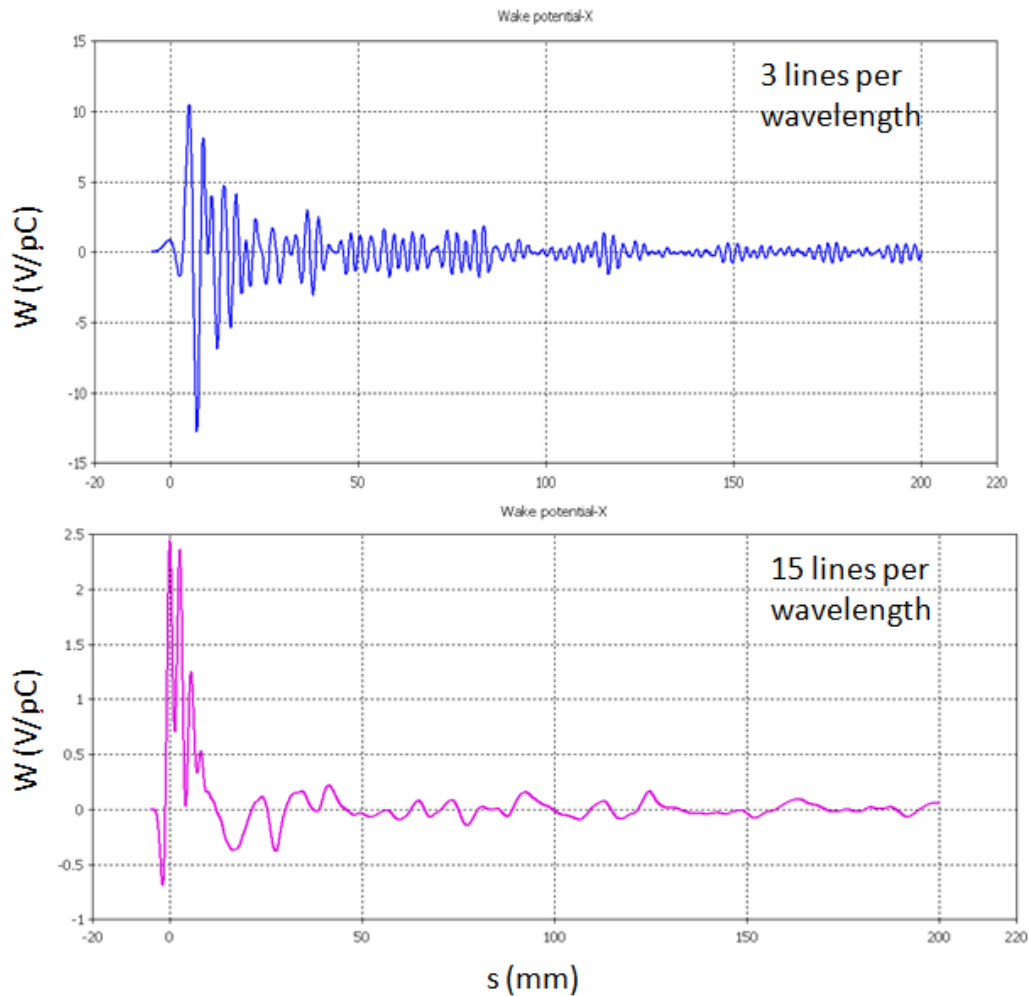


Figure 3.21: CST convergence study on the number of lines per wavelength.

A dedicated study has to investigate the problem of wake function calculation with CST of such complex geometries at high frequencies.

4 Electromagnetic properties of NEG at high frequencies

4.1 Motivation

The performance of the CLIC DR is likely to be limited by collective effects due to the unprecedented brilliance of the beams. Coating will be used in both electron (EDR) and positron damping rings (PDR) to suppress effects like electron cloud formation or ion instabilities. The impedance modeling of the chambers, necessary for instabilities studies which will ensure safe operation under nominal conditions, must include the contribution from coating materials applied for electron cloud mitigation and/or ultra-low vacuum pressure. This advocates for the correct characterization of this impedance in a high frequency range, which is still widely unexplored.

Layers of coating materials such as aC [56–59] and NEG [60, 61] are necessary for e-cloud mitigation and ultra-high vacuum respectively. Studies presented in this chapter are focused on NEG characterization and the waveguide method is used to define material properties in a range from tens to hundreds of GHz. The electrical conductivity of the material is inferred by combining the measured transmission coefficient S_{21} with 3D EM simulations with CST Microwave Studio® (CST MWS).

4.2 Waveguide method and CST simulation

4.2.1 Method

The proposed method requires the use of a rectangular waveguide connected to a vector network analyzer (VNA) and the 3D CST simulation of the exact geometry waveguide. The waveguide is a 2-port network that can be described by means of the S-parameters as a function of frequency. The transmission coefficient S_{21} , from the scattering matrix, is related to the waveguide's attenuation, which depends on the effective conductivity. For a rectangular

Chapter 4. Electromagnetic properties of NEG at high frequencies

waveguide, the attenuation a is given by

$$a = -\frac{10}{L} \log_{10} \frac{r-1}{r+1} \text{ dB} \quad (4.1)$$

where L is the length of the waveguide and r the measured voltage standing-wave ratio. The attenuation for the TE₁₀ mode is related to the effective conductivity as follows [62]

$$a = \frac{1}{2b} \frac{1}{[1 - (\lambda_0/\lambda_c)^2]^{1/2}} \left(\frac{4\pi}{\lambda_0 \mu_0 c \sigma} \right)^{1/2} \left[1 + \frac{2b}{\alpha} \left(\frac{\lambda_0}{\lambda_c} \right)^2 \right], \quad (4.2)$$

where a is the attenuation in Nepers per meter, b the waveguide height in meters, λ_0 the free space wave-length in meters, λ_c the cut-off wave-length in meters, μ_0 the permeability of free space, c the speed of light and α the waveguide width in meters.

As an example of different losses experienced due to different material conductivities, S_{21} measurements of StSt and Cu waveguides are shown in Figure 4.1. Lower losses are observed in a Cu waveguide due to its higher conductivity, compared to StSt.

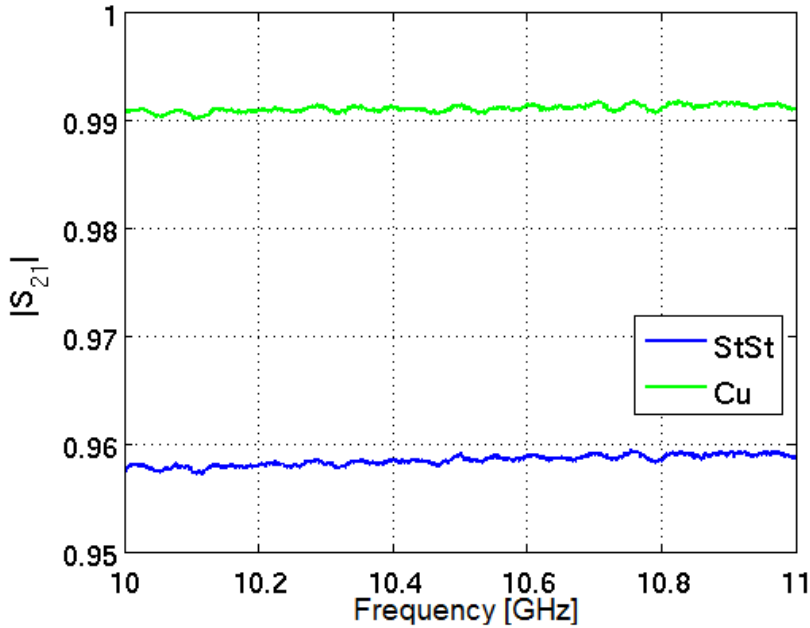


Figure 4.1: S_{21} for StSt and Cu waveguide. Higher losses are measured for StSt due to its lower conductivity.

The VNA was calibrated using Short-Open-Load-Thru (SOLT) [63]. The exact geometry Cu waveguide can be simulated with CST and S_{21} is calculated assuming the DC conductivity of Cu. However, if the material conductivity is the unknown parameter, several simulations can be done sweeping the conductivity. As an example, CST calculation of S_{21} (at 10 GHz), for various conductivities, is shown in Figure 4.2.

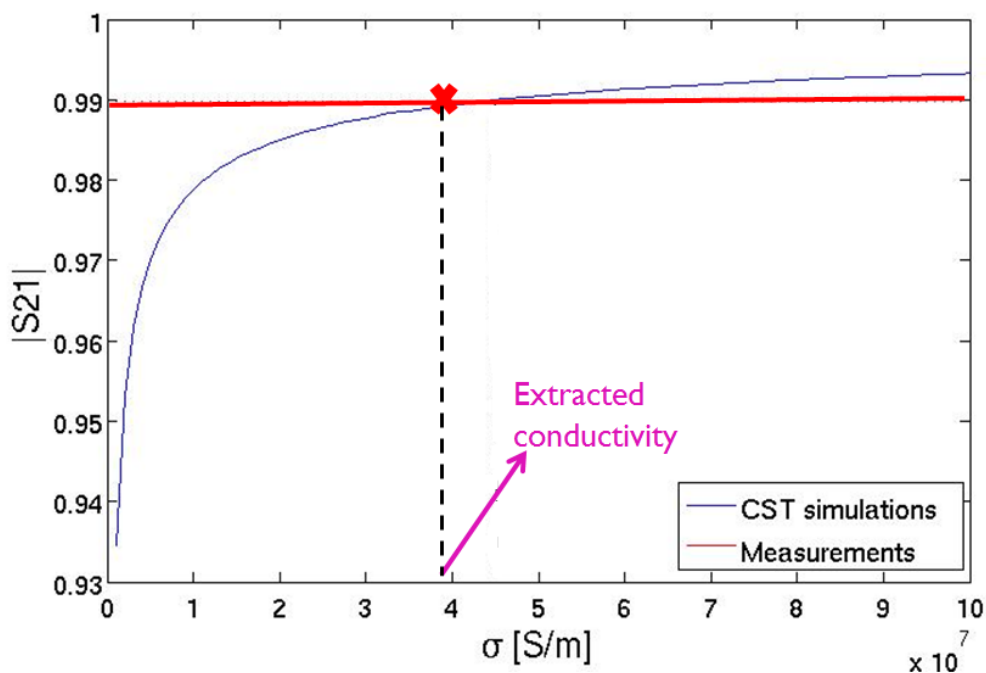


Figure 4.2: S_{21} calculation for various conductivities with CST, at 10 GHz (in blue). Intersection with measured data from Cu (in red) at the same frequency. From the intersection, the conductivity that matches the measured losses is extracted at this specific frequency.

The CST calculation of S_{21} at 10 GHz is shown in blue for various conductivities in Figure 4.2. At the same frequency, the measured value of S_{21} is available for Cu (Figure 4.1). Intersecting the measured data (in red) with the results from the CST simulation, the conductivity that matches the measured losses is extracted at this specific frequency. By repeating the intersection over the whole frequency range of interest, the conductivity can be extracted as a function of frequency.

4.2.2 Benchmark with known materials

As a benchmark of this method, standard X-band waveguides are used, made from well known and characterized materials such as Cu and StSt. The measurements are carried out on the loss arising from the fundamental TE_{10} mode near the cutoff frequency. As a second step, Cu waveguides are sputtered with NEG for the characterization of the effective conductivity. Using a network analyzer, the transmission coefficient is measured over a frequency range from 10 to 11 GHz. The experimental method's setup is displayed in Figure 4.3, where a Cu rectangular waveguide is connected to a VNA. The waveguide has a width of 22.86 mm, height of 10.16 mm and length of 50 cm.

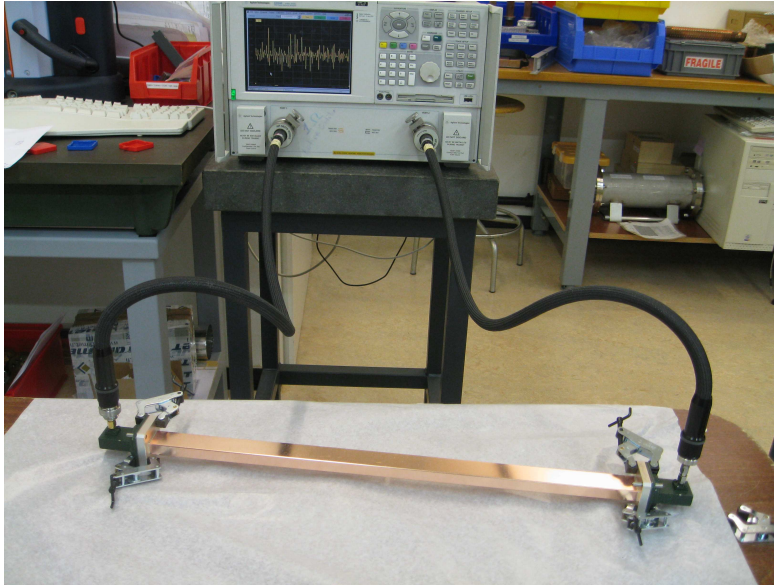


Figure 4.3: Experimental setup: using a network analyzer, the transmission coefficient S_{21} is measured.

4.2.3 S parameters

The scattering parameters, or also known as S-parameters, are used to describe the behavior in frequency domain of a linear electrical network. Networks are described in terms of ports and a 2-port network is the most commonly used. In Figure 4.4 [64], α_n corresponds to the signal traveling towards port n (incident power wave), while b_n corresponds to the signal traveling away from port n (reflected power wave). As shown in Figure 4.4, α_n is defined as the complex signal at a certain frequency ω , which is fed into port n . The return signal at port n is defined as b_n and is a linear combination of the reflected signal ($\alpha_n S_{nn}$) and the transmitted one from port m ($\alpha_m S_{nm}$). The relationship between α_n and b_n parameters can be expressed with a set of linear equations for a 2-port network

$$\begin{aligned} b_1 &= \alpha_1 S_{11} + \alpha_2 S_{12}, \\ b_2 &= \alpha_1 S_{21} + \alpha_2 S_{22}. \end{aligned} \quad (4.3)$$

Eq.(4.3) can be expressed also in a matrix form as

$$\begin{pmatrix} b_1 \\ b_2 \end{pmatrix} = \begin{pmatrix} S_{11} & S_{12} \\ S_{21} & S_{22} \end{pmatrix} \begin{pmatrix} \alpha_1 \\ \alpha_2 \end{pmatrix}. \quad (4.4)$$

The first index in the S-parameter S_{mn} refers to the port at which energy emerges and the second is the port at which energy enters. Therefore, S_{21} is a measure of power coming from port 2 after applying an RF excitation at port 1, while S_{11} represents the reflection at port 1.

4.3. Measurements with a stainless steel waveguide in X-band

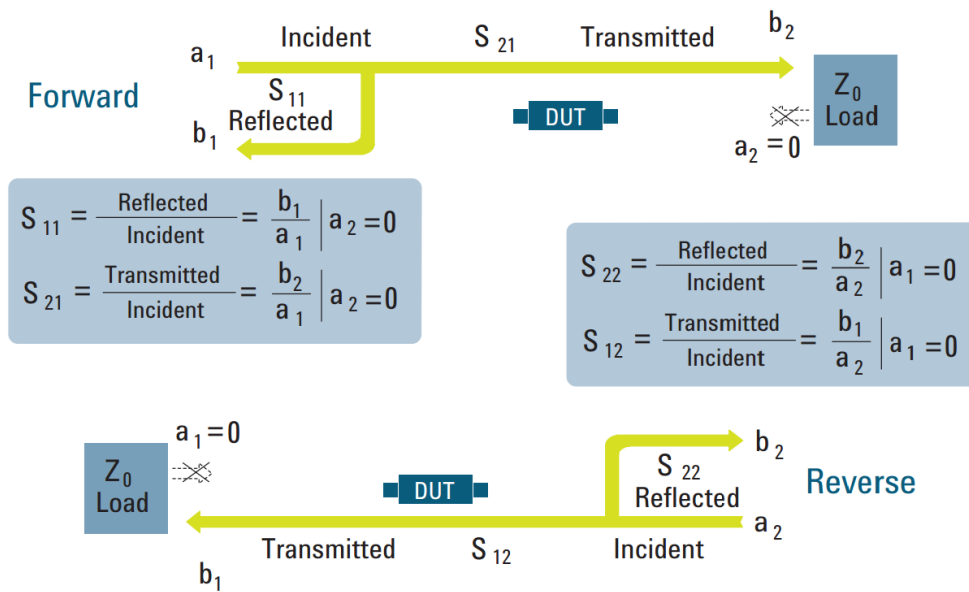


Figure 4.4: Measuring scattering parameters.

4.2.4 Network analyzer

A network analyzer is used for measuring the S-parameters. A sinusoidal wave of a certain frequency is sent into the Device Under Test (DUT) in order to measure the transmitted and reflected wave. Measurements can be done over a range of frequencies.

With the amplitude and phase information of the reflected and transmitted waves, it is possible to define the reflection and transmission characteristics of the DUT. The characteristics can be expressed as vector (with magnitude and phase), or scalar (with magnitude only or phase only) quantities. There are two basic types of network analyzers, the scalar network analyzer (SNA), that measures amplitude properties only, and the vector network analyzer, that measures both amplitude and phase properties.

The S_{11} and S_{21} parameters are defined using the magnitude and phase of the reflected, transmitted and incident signals as port 2 is terminated on a known load. The S_{22} and S_{12} parameters can be defined if port 2 becomes the source and port 1 is terminated on a perfect load. Measurements of the S-parameters are illustrated schematically in Figure 4.4. The measured $|S_{21}|$, or $|S_{12}|$, coefficient is related to the attenuation due to the EM losses in the network, and thus related to the unknown properties.

4.3 Measurements with a stainless steel waveguide in X-band

A 50 cm long StSt waveguide, of type 316LN, was the first DUT for benchmarking the method in X-band (see Figure 4.5). The waveguide was produced by the Mechanical and Materials Engineering group of CERN (EN-MME) in two split-blocks with a vertical cut, also known

as an E-plane split. Such waveguides are known as WR-90, with frequency limits from 8.2 to 12.4 GHz (so that only the lowest mode, TE₁₀, can propagate) and have inner dimensions of 22.86×10.16 mm [67].

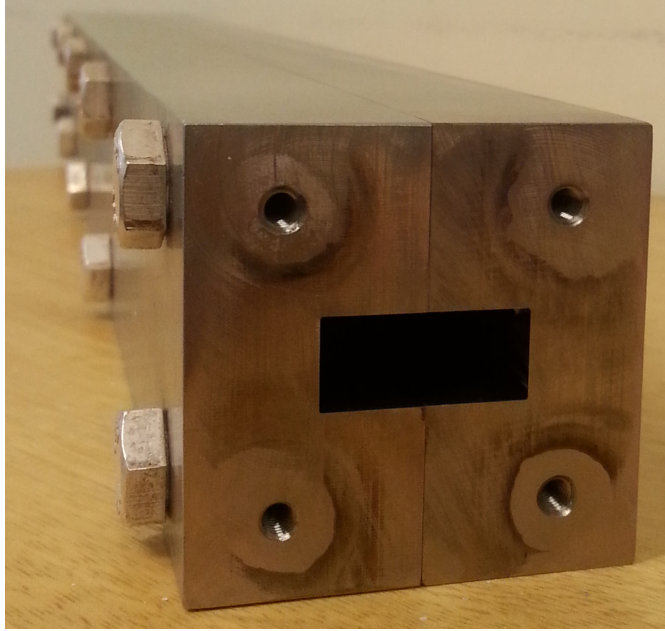


Figure 4.5: X-band StSt waveguide with a vertical cut.

Using a network analyzer, the transmission coefficient S_{21} is measured over a frequency range from 10 to 11 GHz. In Figure 4.6, the result of this measurement is illustrated in blue. In the same plot, it is compared with the expected S_{21} parameter from CST simulations for an X-band StSt waveguide with conductivity $\sigma = 1.35 \times 10^6$ S/m (magenta). For the CST simulation, the model shown in Figure 4.7 was used.

Surface Roughness

In CST simulations, it is assumed that the waveguide surface is perfect, i.e. perfectly smooth. However, this component of surface texture that quantifies deviations of the real surface from the ideal form, has to be taken into account since it could play a role.

There are several parameters that describe surface roughness, among which R_a is the most common. It is used to describe the arithmetic average and is defined as $R_a = \frac{1}{n} \sum_{i=1}^n |y_i|$, where

n is the number of points along the trace and y_i the vertical distance from the mean line to the i^{th} data point. The root mean square, R_q or R_{RMS} , is another way to define roughness by

$$R_q = \sqrt{\frac{1}{n} \sum_{i=1}^n y_i^2}.$$

Measurement of the R_a parameter was performed along the StSt waveguide, by measuring 15 points in each block, as can be seen in Figure 4.8 [65].

4.3. Measurements with a stainless steel waveguide in X-band

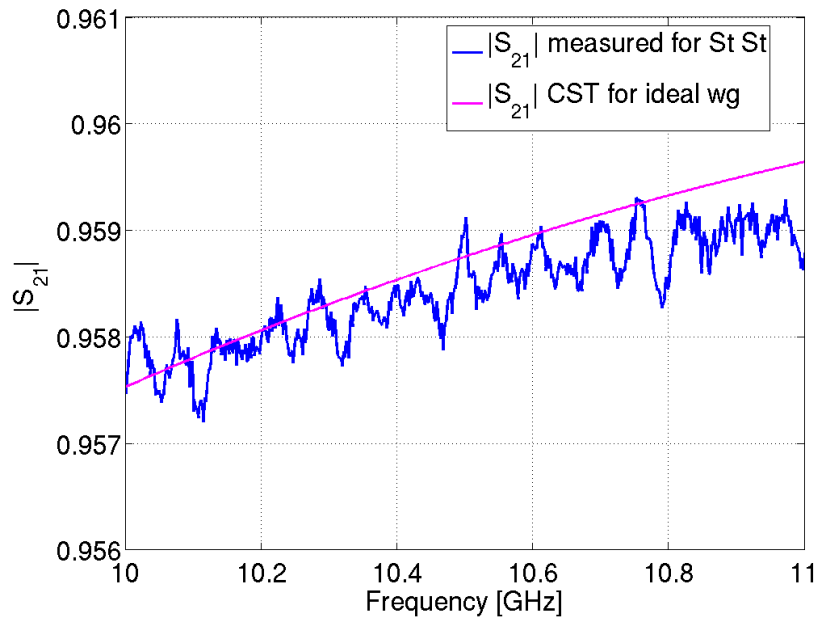


Figure 4.6: S_{21} for a StSt waveguide: experiment (blue) and CST simulation (magenta) comparison.

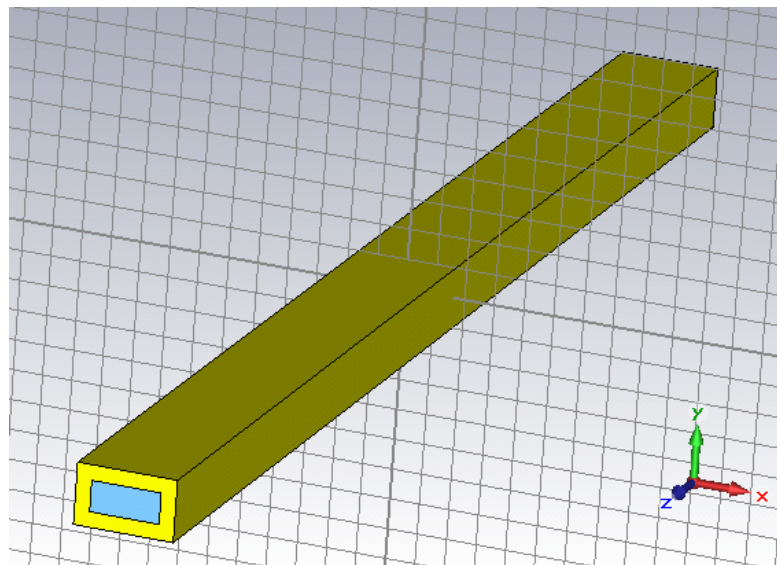


Figure 4.7: 3D CST model of a rectangular X-band waveguide made of StSt (yellow) and vacuum (blue).

Calculating the average R_a value, surface roughness was estimated to be $0.6 \mu\text{m}$. The skin depth δ at a certain frequency $\omega = 2\pi f$, quantifies at which depth the EM field is attenuated by a factor of e^{-1} inside the material with conductivity σ . It can be calculated using the

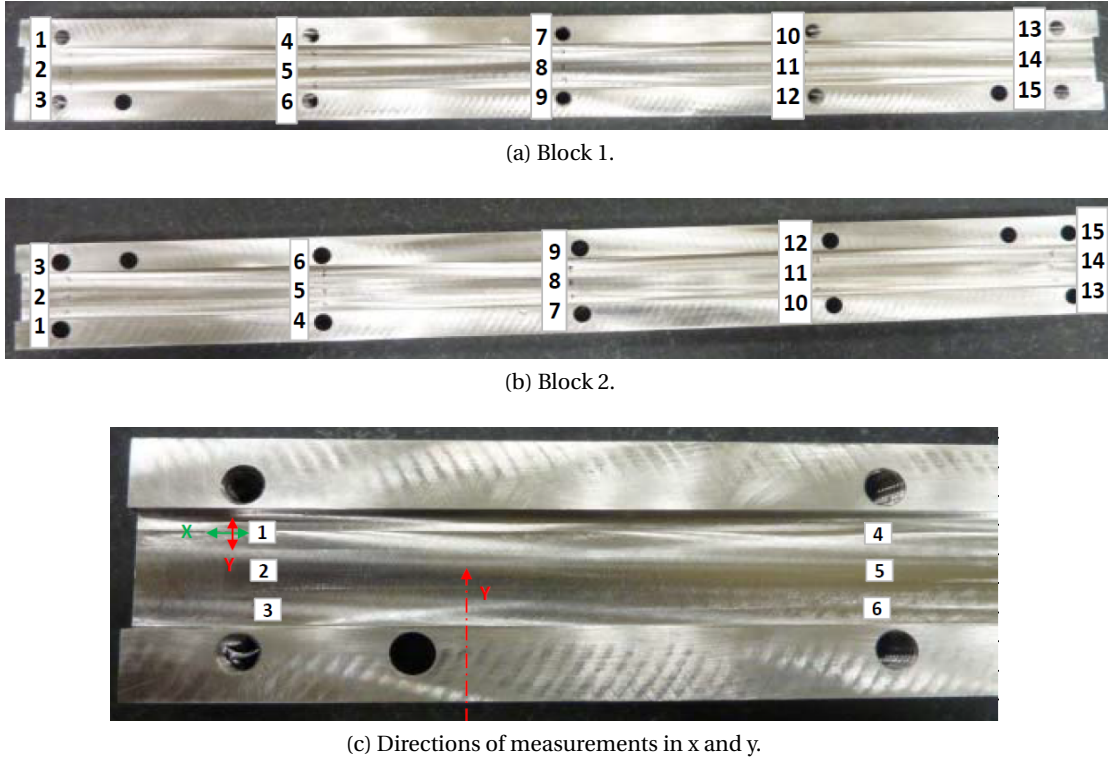


Figure 4.8: Measurement points along the split blocks of the StSt waveguide in x and y plane.

formula [66]

$$\delta = \frac{1}{\sqrt{\pi f \mu \sigma}}, \quad (4.5)$$

where $\mu = \mu_r \mu_0$ is the permeability, μ_r the relative magnetic permeability and μ_0 the permeability of free space. For non magnetic materials with $\mu_r = 1$, the formula 4.5 can be simplified to

$$\delta \approx 503 \sqrt{\frac{1}{\sigma f}}. \quad (4.6)$$

At 10 GHz and for StSt conductivity of $\sigma = 1.35 \times 10^6$ S/m, the skin depth is $\delta = 4.3 \mu\text{m}$. In this case, the skin depth is much larger than the surface roughness and the latter is not expected to induce significantly higher losses. The S_{21} results from measurements and simulation are in good agreement, as illustrated in Figure 4.6 above.

From CST simulation and measurements to the characterization of conductivity

At each frequency, the output of CST is the S_{21} parameter as a function of conductivity. The relative permittivity ϵ_r and permeability μ_r are assumed to be equal to one, while conductivity

4.4. Measurements with a copper waveguide in X-band

σ is assumed to be the unknown parameter. By intersecting at each frequency the measured S_{21} with the CST output obtained numerically, the electrical conductivity is determined as a function of frequency. The extracted conductivity of StSt is shown in Figure 4.9, while the DC conductivity for 316LN is $\sigma = 1.35 \times 10^6$ S/m. The AC conductivity is expected to be very close to DC in this frequency regime, therefore the very good agreement between measurements and theory confirms the validity of the waveguide method.

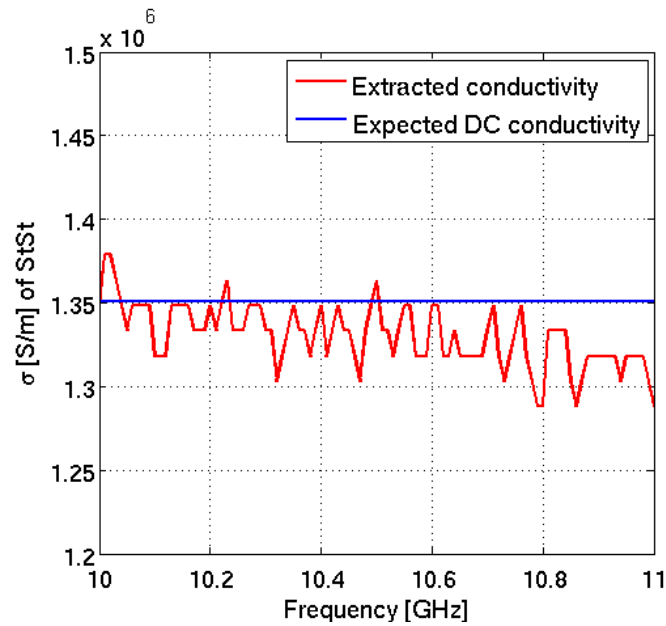


Figure 4.9: Extracted conductivity of StSt from measurements and CST simulations for a waveguide with smooth surface. The expected DC conductivity for this type of StSt is added for reference (blue).

4.4 Measurements with a copper waveguide in X-band

An X-band 50 cm long, with interior dimensions 22.86×10.16 mm [67], annealed Cu waveguide was the second DUT. It was also used to validate the method between 10 and 11 GHz. Measurements of the S_{21} parameter were performed using the VNA and the results are shown in Figure 4.10 (in blue), compared to the expected S_{21} from CST (in purple) for an ideal Cu waveguide with conductivity $\sigma = 5.8 \times 10^7$ S/m.

For Cu, the measured S_{21} is lower than the simulation for the ideal waveguide. That indicates that extra losses have occurred, as seen in Figure 4.10. Theoretical losses for Cu are 0.108 dB/m at 10 GHz [68], while measured losses are 0.16 dB/m at the same frequency. Therefore, real losses were slightly higher. At frequencies where the skin depth approaches the surface roughness, higher losses occur having as a consequence to measure lower S_{21} values compared to the ideal case.

The extracted Cu conductivity in Figure 4.11, is about a factor of 2 lower than the expected DC $\sigma = 5.8 \times 10^7$ S/m. CST is found to agree with this estimated effective conductivity of Cu if

roughness is $R_q=0.4 \mu\text{m}$. However, such small difference in S_{21} between measurements and theoretical expectation could easily be justified from the S_{11} reflection.

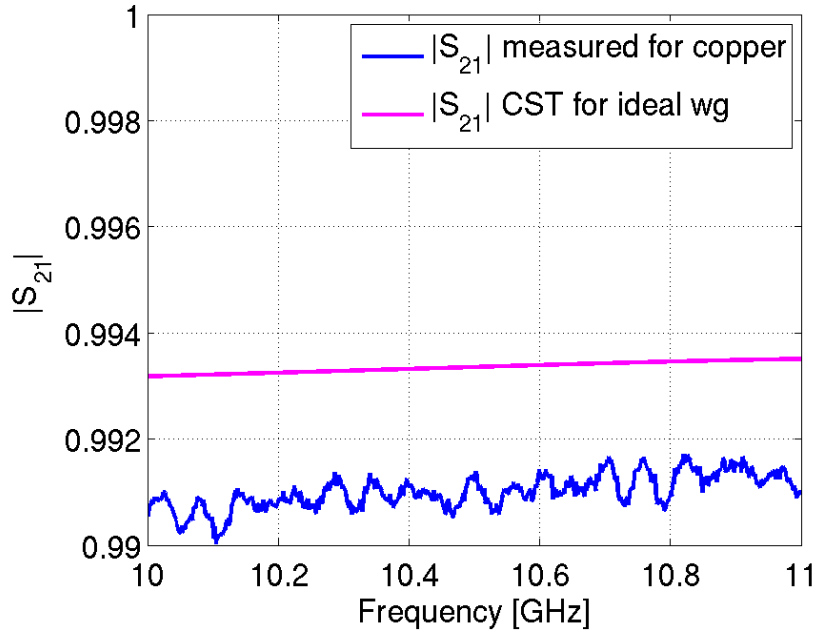


Figure 4.10: S_{21} for Cu: measured (blue) and CST simulation (magenta) comparison.

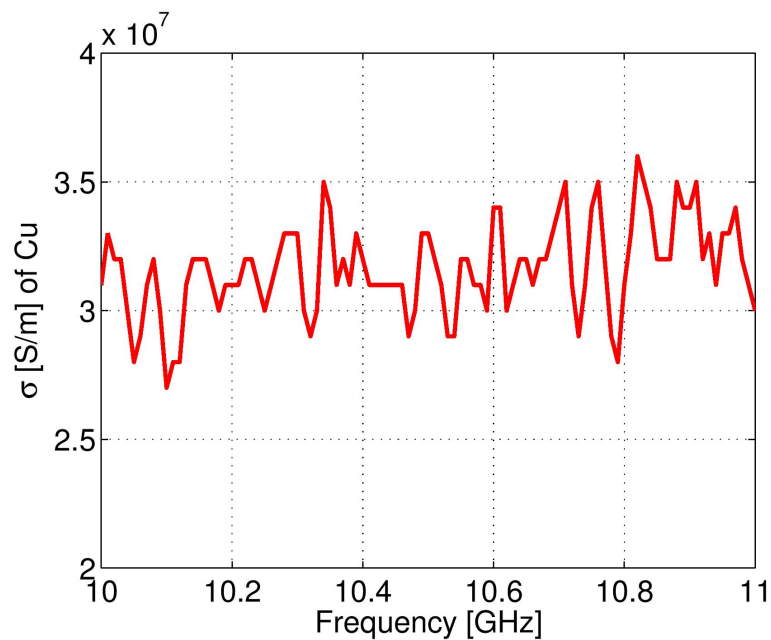
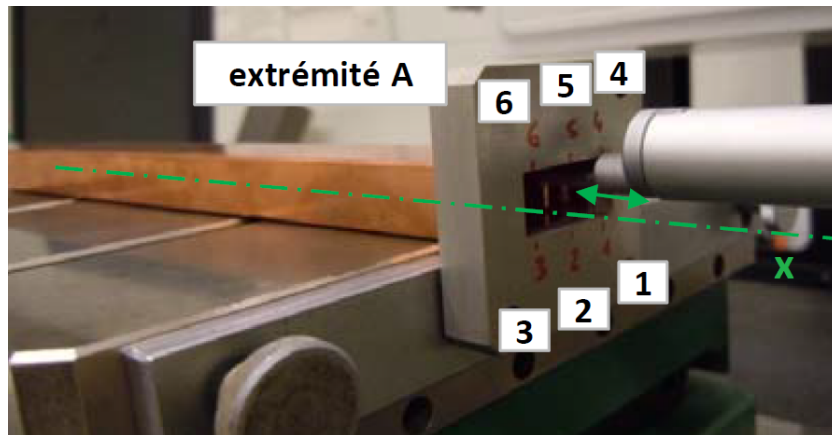


Figure 4.11: Effective conductivity of Cu as extrapolated from waveguide measurements and CST simulations for a waveguide with smooth surface.

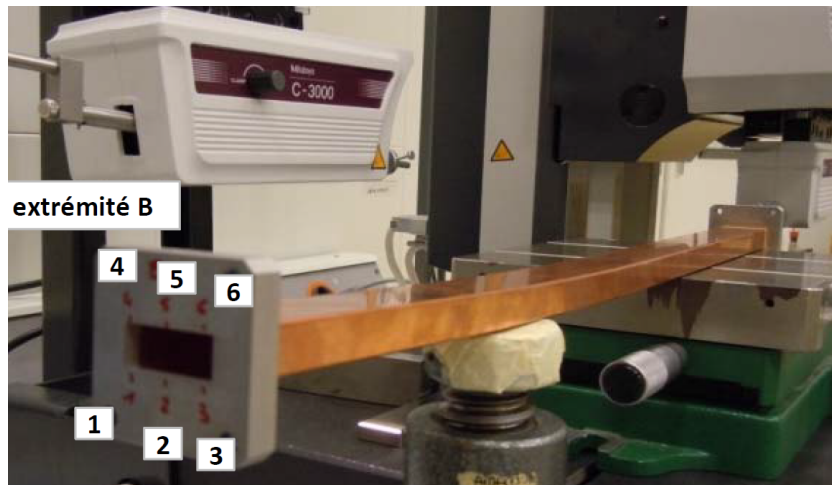
4.4. Measurements with a copper waveguide in X-band

Surface roughness measurements on the Cu waveguide

Measurements of R_q were realized at the two extremities of the Cu waveguide, which were accessible without having to destroy the waveguide. R_q measurements were taken at six points at each extremity, as seen in Figure 4.12 [69].



(a) Measurement points at one extremity.



(b) Measurement points at the second extremity.

Figure 4.12: Measurement points of R_q at the two extremities of the Cu waveguide.

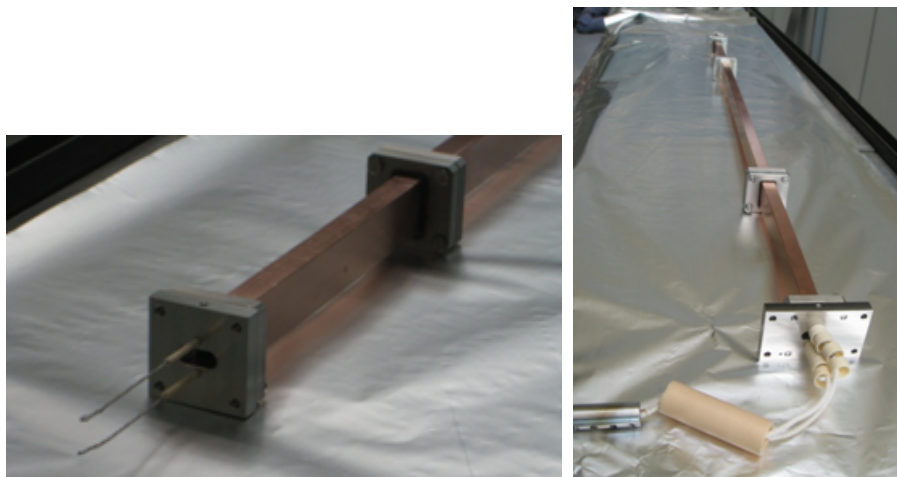
The average R_q is $0.3 \mu\text{m}$, while the skin depth at 10 GHz is $\delta=0.66 \mu\text{m}$. This value is very close to the predicted one from CST ($0.4 \mu\text{m}$), that would explain the extracted Cu conductivity. CST has a built-in calculator of effective conductivity. The input parameters required are the DC conductivity, the frequency and the surface roughness.

4.5 Measurements of NEG on a copper waveguide in X-band

After the successful benchmark of the method for StSt and Cu, the next step was to characterize NEG. For this purpose, the aforementioned Cu waveguide had to undergo a NEG coating procedure.

4.5.1 NEG coating process

For the NEG coating process, 3 inter-twisted wires of 3 mm diameter were used, made from an alloy of Titanium, Zirconium and Vanadium (Ti-Zr-V) [60]. Two cathodes, made of inter-twisted elemental wires, were placed inside the Cu waveguide, as shown in Figure 4.13, and NEG is deposited via DC magnetron sputtering on the waveguide's inner wall.



(a) Inter-twisted wires of Ti-Zr-V placed inside the Cu waveguide.

(b) Two cathodes placed inside the Cu waveguide.

Figure 4.13: Preparation of the Cu waveguide for the NEG coating.

The expected composition is around 30% Ti, 30% Zr and 40% V [61]. Typical values of NEG coating films in accelerators are 1-2 μm . For the purpose of the measurements, a much thicker coating of 9 μm was targeted in order to maximize the EM interaction inside the NEG film.

4.5.2 NEG-coated Cu waveguide measurement results

NEG coating of 9 μm

S_{21} was measured for the NEG-coated Cu waveguide. In Figure 4.14, the results are shown before and after the coating. The lower measured S_{21} coefficient in the presence of the NEG film (in blue) compared to higher S_{21} values (in green), indicates that the NEG thickness is sufficient to allow EM interaction of the propagating wave with NEG [70], causing a significantly higher amount of losses.

4.5. Measurements of NEG on a copper waveguide in X-band

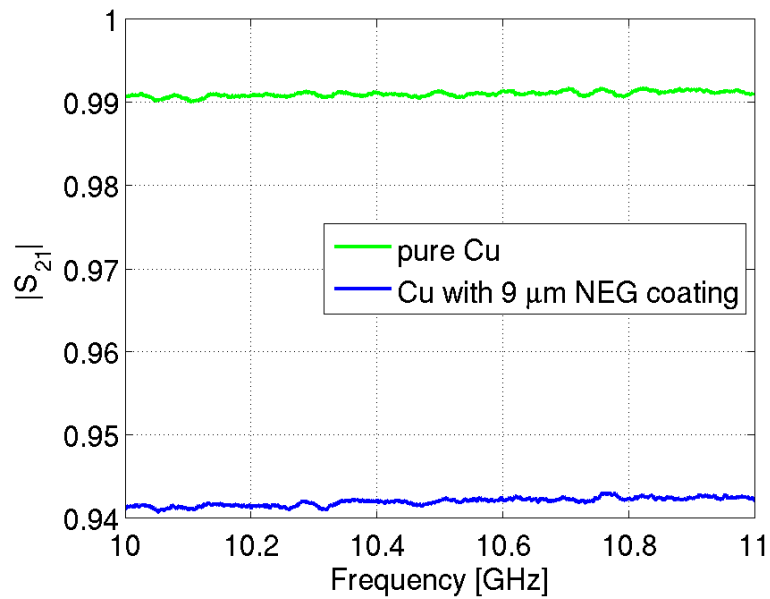


Figure 4.14: Measured S_{21} as a function of frequency for Cu and NEG-coated Cu waveguide.

Ambiguity of the solution for the NEG conductivity

The intersection of simulated and measured S_{21} is shown in Figure 4.15 at 10 GHz.

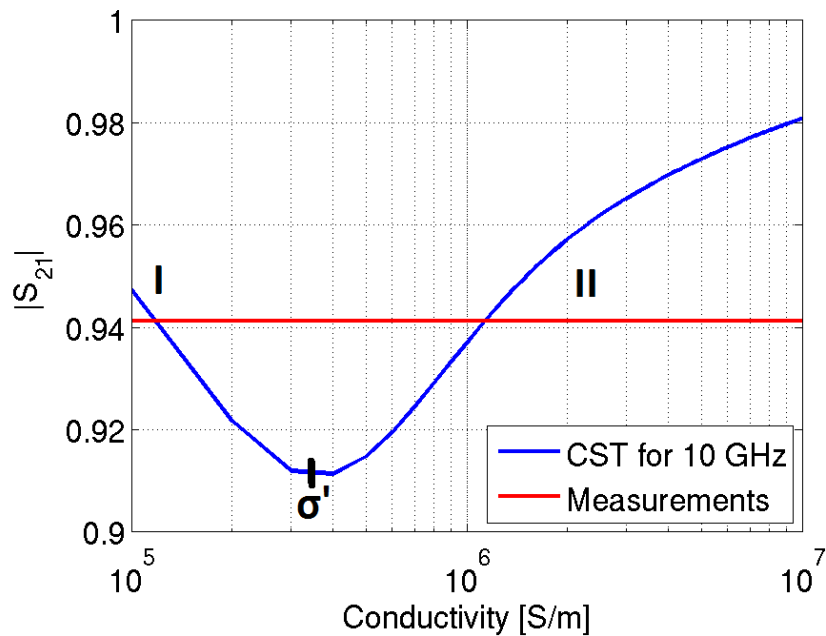


Figure 4.15: Example of intersection of simulated S_{21} (blue) as a function of conductivity with the measured value (red) at 10 GHz for a NEG-coated waveguide.

Chapter 4. Electromagnetic properties of NEG at high frequencies

As seen in the plot, two possible solutions exist, while only one can correspond to the real material properties. The lower conductivity is named as *first solution* and the higher as *second solution*. To explain the shape of the blue curve in Figure 4.15, let's first assume that the NEG has low conductivity, below the value σ' at which the simulated curve of $|S_{21}|$ exhibits a minimum. Here, the skin depth, as calculated from Eq.(4.5), is found to be larger than the NEG thickness, which is assumed to be $t_{\text{NEG}}=9 \mu\text{m}$. Therefore, since $\delta > t_{\text{NEG}}$, the EM field will be attenuated inside the NEG film as well as in the Cu underneath. In this region, as σ_{NEG} increases, the skin depth decreases and the attenuation inside the NEG film dominates since the amount of EM field attenuated inside the NEG film is increased. This leads to a decreasing $|S_{21}|$, if the assumption is made that $\sigma_{\text{NEG}} < \sigma_{\text{Cu}}$. For $\sigma_{\text{NEG}} > \sigma'$, the losses mainly happen in the NEG and therefore $|S_{21}|$ again increases as a function of σ_{NEG} . For $\sigma_{\text{NEG}} = \sigma'$, the two effects compensate each other. For a single layer material, the blue curve from CST would only have a monotonic behavior like that of region II, since all the field would attenuate inside the one layer structure. Due to the existence of the NEG coating, the structure is now a two layer structure. Therefore, depending on the conductivity of the two materials of the two layers, we have a regime in which two possible solutions occur, the *first* and the *second solution*, as shown in Figure 4.15.

The plot displayed in Figure 4.16 shows the NEG effective conductivity and the two different curves correspond either to the *first* or *second solution* as a function of frequency. Accepting the *first* solution results in a very stable conductivity value of $1.2 \times 10^5 \text{ S/m}$, while the *second* solution is in the order of 10^6 S/m and seems to exhibit a frequency dependent behavior. Since the EM properties of a material, such as conductivity, are unique only one of the 2 solutions can correspond to the real properties.

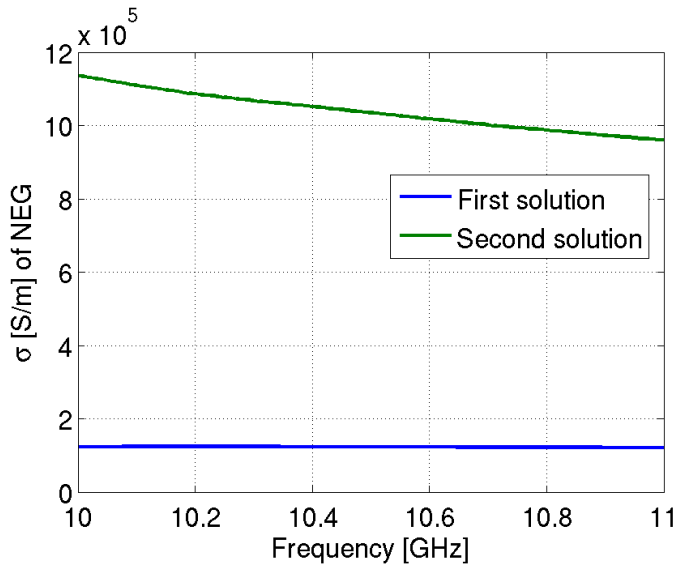


Figure 4.16: Effective conductivity of NEG.

The unknown NEG conductivity leads to two possible scenarios. The first is when the skin depth is much smaller than the thickness of the NEG film. In this case, the EM interaction is

4.5. Measurements of NEG on a copper waveguide in X-band

only with the NEG (*second* solution). The second is when the skin depth is comparable to the thickness and the EM interaction is with both the NEG and the Cu.

4.5.3 Error analysis for CST simulations

In order to check the reliability of CST results for the coated waveguide, two tests are done. For the first, different values of NEG thickness are simulated varying from 1 up to 20 μm . NEG conductivity is assumed to be 2×10^6 S/m. The results are illustrated in Figure 4.17 from 10 to 11 GHz. The skin depth at 10 GHz is $\delta=3.56$ μm . From 1 up to 4 μm , the skin depth is comparable, or only slightly larger, than the thickness, and therefore the EM fields interact with both the NEG and the Cu.

As the thickness is increased, the interaction with Cu is reduced to the point where the skin depth is much smaller than the thickness, allowing only the interaction with NEG (thickness between 10 and 20 μm). This explains why the losses are the same if the NEG thickness is between 10 and 20 μm and the curves are superimposed, as shown in Figure 4.17. Therefore, in this region the field is attenuated 100% inside the NEG film. CST MWS results are in agreement with the theoretical expectations.

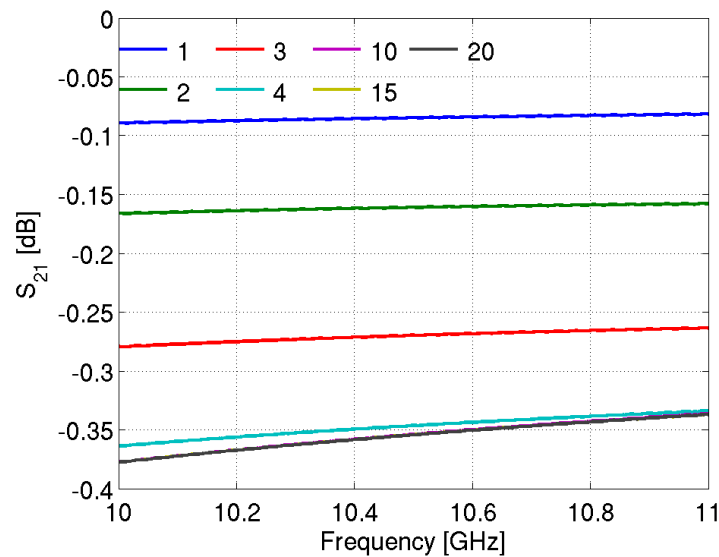


Figure 4.17: S_{21} results obtained from CST MWS for different values of NEG thickness in μm .

As a second test, a waveguide with the properties of NEG (conductivity assumed $\sigma_{NEG} = 2 \times 10^6$ S/m) is compared to a Cu waveguide coated with NEG of 100 μm thickness. Such thick coating results in EM interaction only with the NEG film, since the skin depth is much smaller than the thickness. Therefore, the results of those two simulations should basically be identical. The comparison is illustrated in Figure 4.18 and the two cases are very close, as expected from theory.

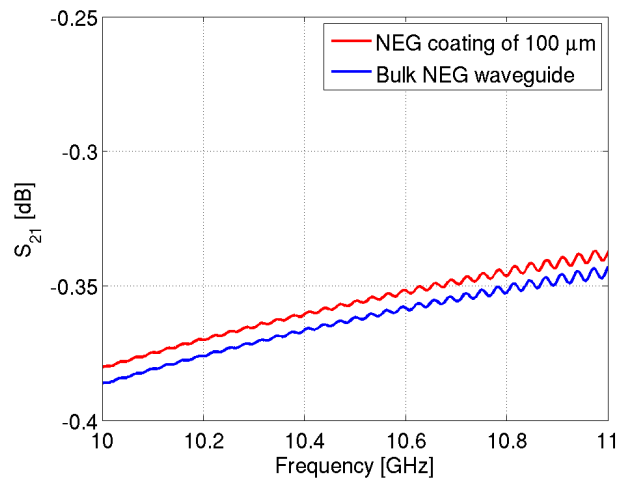


Figure 4.18: Comparison of CST S_{21} results for 100 μm NEG-coated waveguide (red) and a bulk waveguide with NEG properties (blue).

Measurements of the NEG film thickness with XRF

In order to investigate the NEG profile, thickness measurements were done using X-ray fluorescence (XRF). The method is based on the interaction of atoms with X-radiation. If the sample is bombarded by an intense X-ray beam, part of the energy is scattered, but part of it is also absorbed. When the primary X-ray beam hits the sample, the latter is excited. The excited sample emits X-rays along a spectrum of wavelengths characteristic of the atoms present in the sample. The results of XRF measurements along the wider strip of the waveguide, after it was cut, are shown in Figure 4.19. The profile varies between 6 and 11 μm .

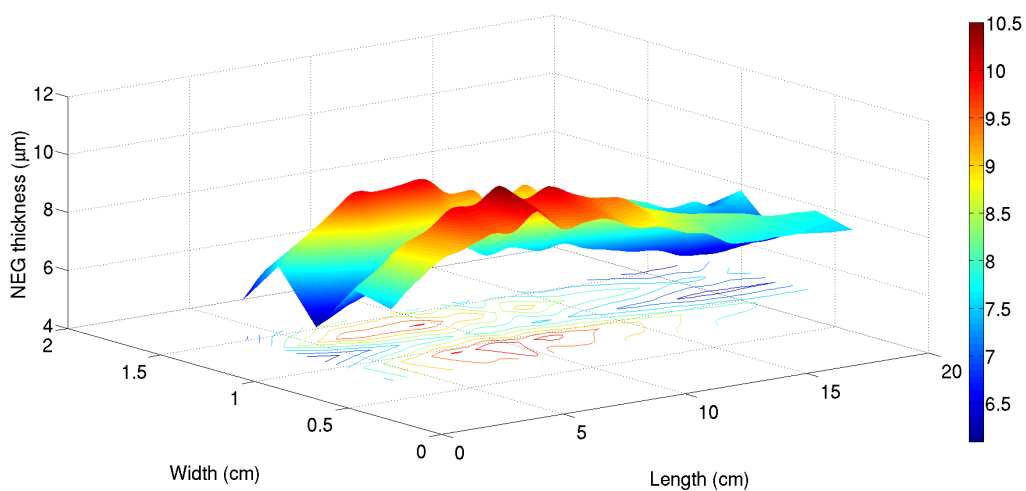


Figure 4.19: NEG layer profile with XRF along 20 cm length.

4.5. Measurements of NEG on a copper waveguide in X-band

Measurements of the NEG film thickness with SEM

The Scanning Electron Microscope (SEM) technique was also used to measure the NEG profile as a comparison to the XRF results. Using an electron microscope and a focused electron beam, images of a sample's surface topography and composition can be obtained. The electron beam, emitted from an electron gun, had an energy ranging from 5 keV to 20 keV.

Four samples were used for those measurements, shown in Figure 4.20, which were bent in order to perform the electron beam scan.

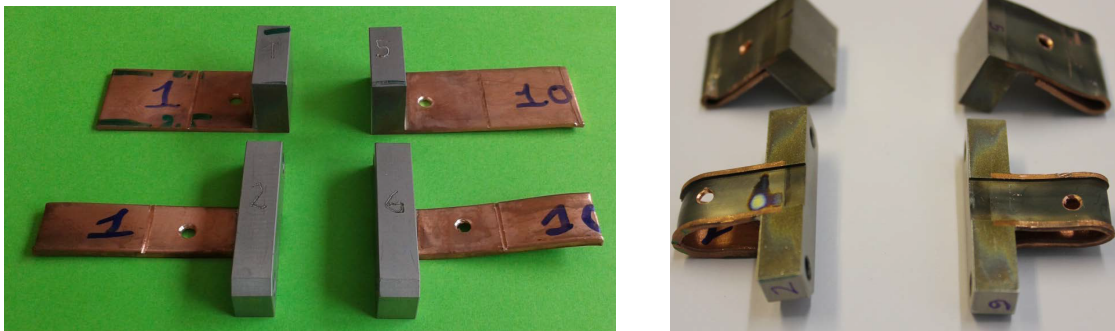


Figure 4.20: Samples for the SEM profile measurements.

Example of the thickness measurements are shown in Figure 4.21. The measurements revealed a profile between 6 and 11 μm , similar to the one with XRF.

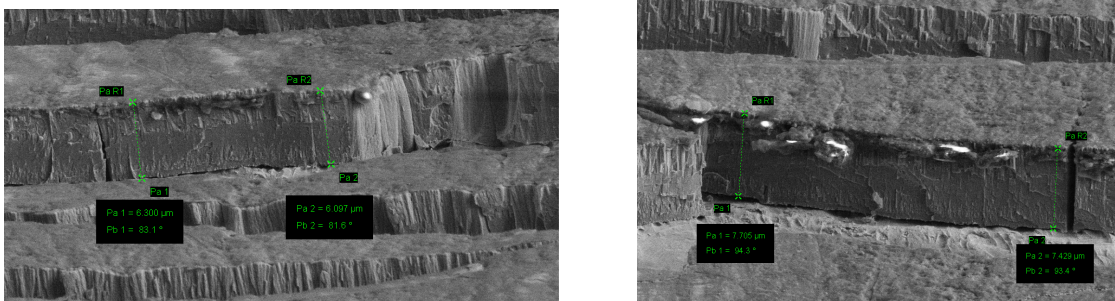


Figure 4.21: SEM profile measurement examples.

A direct comparison to XRF was done by using 3 samples shown in Figure 4.22.

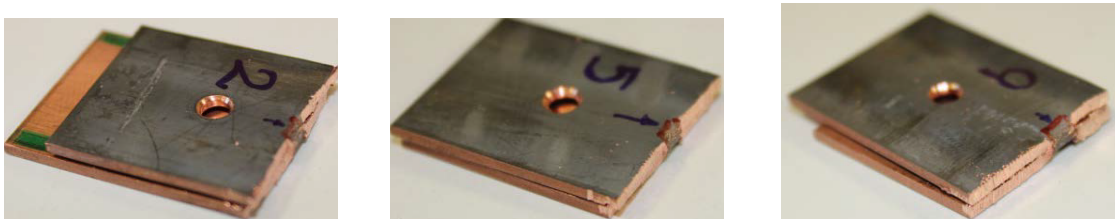


Figure 4.22: Samples used to compare SEM and XRF measurements.

Chapter 4. Electromagnetic properties of NEG at high frequencies

The results from the comparison are summarized in Table 4.1. SEM and XRF techniques provided very similar results for the NEG profile, with values deviating less than 7%.

Table 4.1: SEM and XRF results on NEG thickness.

Sample number	SEM thickness [μm]	XRF [μm]
2	7.60	7.15
	7.24	7.08
	7.28	7.14
5	7.97	7.97
	8.06	8.01
	8.50	7.88
9	8.05	8.04
	8.42	8.00
	7.84	7.93

NEG coating of 20 μm

In order to distinguish which of the two solutions in Figure 4.16 corresponds to the real one, measurements were repeated for a new Cu waveguide. The first stage of coating targeted at 6 μm thickness. As a second step, the waveguide was further coated to reach a final thickness of 20 μm . The much thicker coating of 20 μm could help sort out the ambiguity in the solution of NEG conductivity. S_{21} coefficient measurements are shown together with the previous 9 μm coated waveguide in Figure 4.23.

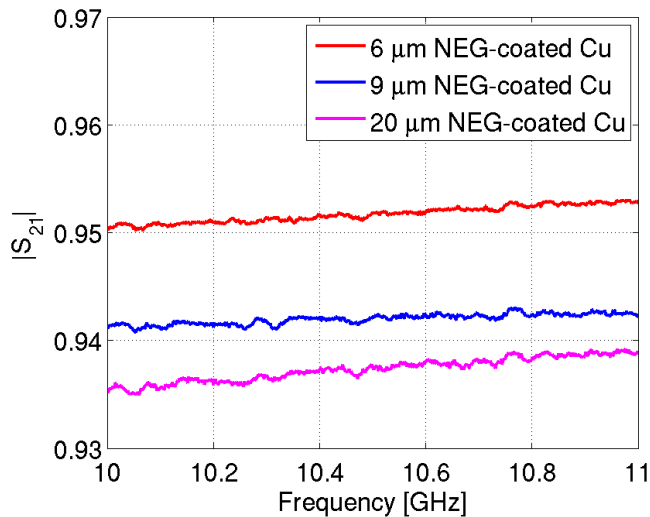


Figure 4.23: S_{21} measurements for the new waveguide coated first at 6 (red) and then at 20 μm (magenta). Also the previous results from the 9 μm coated waveguide are shown for reference (blue).

4.5. Measurements of NEG on a copper waveguide in X-band

A comparison of two different calibration methods, SOLT that was used so far and Thru-Reflect-Line (TRL), was also done. The two methods give similar results within 0.2%, as seen in Figure 4.24.

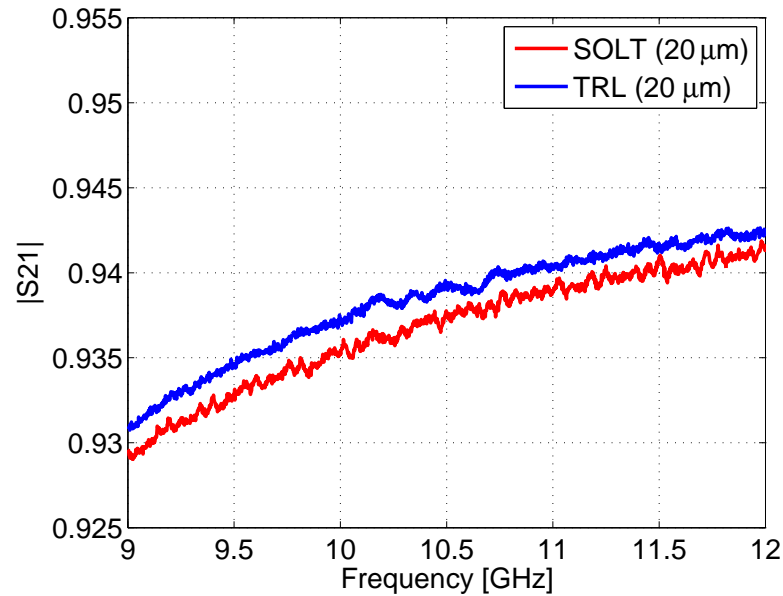


Figure 4.24: S_{21} measurements of the 20 μm NEG-coated waveguide with SOLT and TRL calibration.

Coating in two different steps contributed in understanding that not 100% of the field was attenuated inside the 9 μm film. Losses inside the 6 μm coating, shown in red in Figure 4.23, are less important than losses for 9 μm , shown in blue. What was also demonstrated, is that different losses were measured for the 20 μm coating compared to 9 μm . That indicated that still not 100% of the field was attenuated in the 9 μm film. If that was the case, blue and magenta curve would have to be almost superimposed. Proceeding with the same analysis for the 20 μm NEG-coated waveguide as previously described, there is only one solution in the conductivity range scanned in CST, shown in Figure 4.25.

The extracted NEG conductivity is plotted in Figure 4.26 in purple (almost superimposed with the yellow) assuming 20 μm thickness and is compared to the 9 μm result (in black). The difference observed between 9 and 20 μm can be attributed to the fact that not all the losses occur inside the NEG film when the thickness of the coating is 9 μm . Assuming 12 up to 28 μm in CST simulations, all curves are in good agreement which shows that losses are only inside the NEG film. Therefore, the extracted conductivity value remains the same and is independent of the NEG thickness as long as it is above 12 μm .

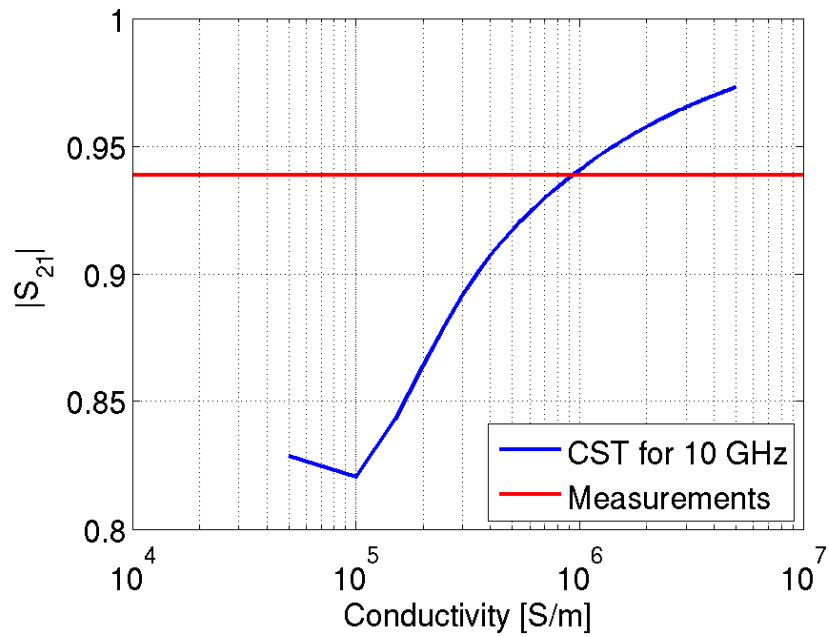


Figure 4.25: Intersection of simulated S_{21} (blue) as a function of conductivity with the measured value (red) at 10 GHz.

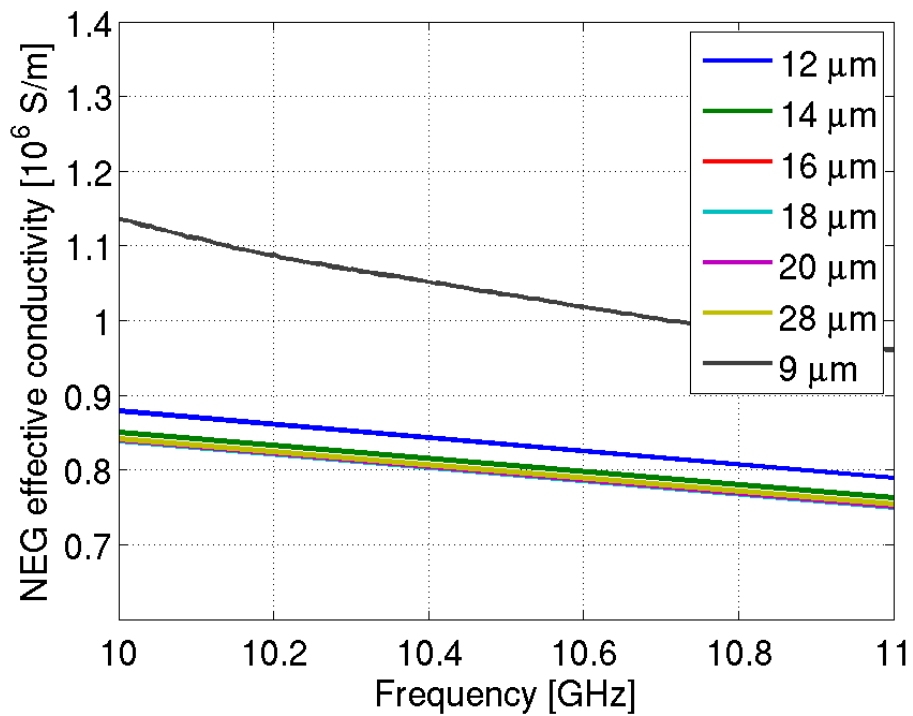


Figure 4.26: Effective conductivity of NEG.

Measurements of the NEG film thickness with XRF

Once the measurements with the second NEG-coated Cu waveguide were completed, the XRF method was used to reveal the NEG profile. Measurements were performed along the 2 cm wide strip. The results are shown in Figure 4.27.

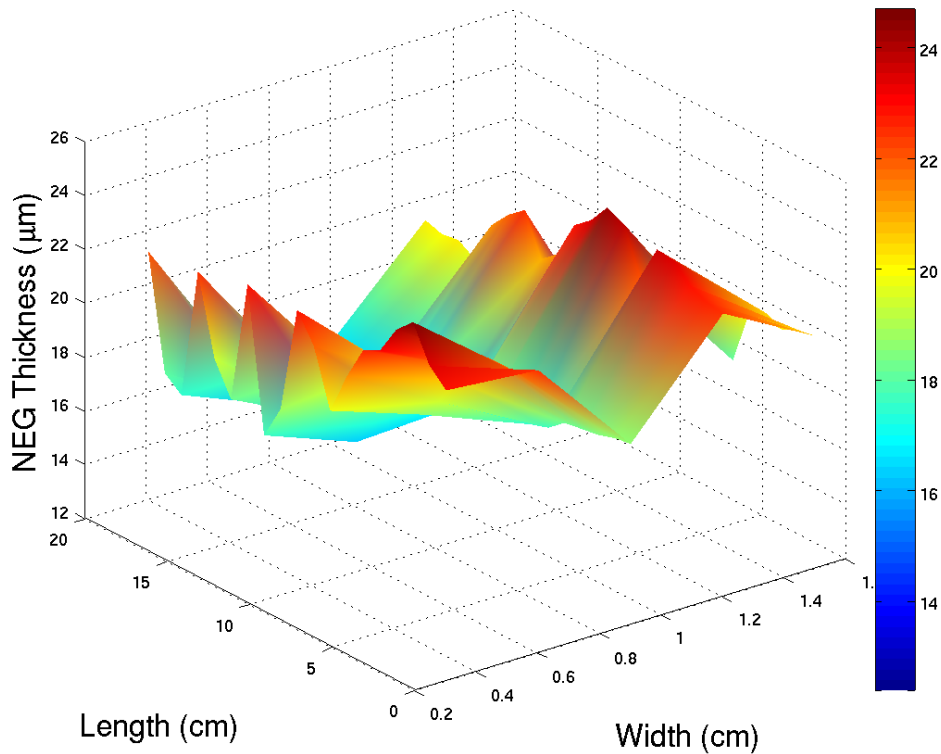


Figure 4.27: NEG thickness profile with x-ray measurement.

The coating profile varies between 12 and 28 μm , with the plot having 2 sets of maxima corresponding to the position of the 2 cathodes along the waveguide.

4.5.4 Conclusions about the NEG conductivity in X-band

Measurements with the waveguides in X-band conclude to values of NEG conductivity of about $(1 \pm 0.2) \times 10^6$ S/m. The uncertainty is about 20% coming from the 2 sets of measurements, as well as the non-uniformity of the profile, which cannot be correctly simulated in CST but was revealed with XRF measurements.

Resistance measurements were realized at CERN for NEG thin films in order to characterize the DC conductivity. Resistance was found between 100 and 150 $\mu\Omega$ cm. Therefore, the DC conductivity was measured to be between 0.66 and 1×10^6 S/m. The extracted conductivity value with our method is in good agreement with the DC value.

4.6 NEG properties characterization above 200 GHz

The proposed method, once benchmarked in X-band and used for characterizing NEG between 10 and 11 GHz, is then applied to hundreds of GHz. The short DRs bunch length of 1.8 mm rms, translates into a frequency spectrum up to hundreds of GHz, therefore the characterization of NEG is necessary up to those frequencies. The VNA, necessary to perform such high frequency measurements, is not currently available at CERN.

For this reason, a collaboration was established with Virginia Diodes (VDI) [71], a company located in Charlottesville, Virginia, which manufactures state-of-the-art measurement equipment for THz applications. That includes VNA and extension modules, as well as rectangular waveguides in several frequency bands. Using VNA extenders, a network analyzer can extend into THz. For the purpose of those measurements, WR3.4 and WR1.5 rectangular waveguides were used between 220-330 GHz and 500-750 GHz. An order was placed with VDI to purchase four WR3.4 and three WR1.5 waveguides of 25 mm length.

4.6.1 220-330 GHz: WR-3.4 waveguides

The species of the purchased waveguides can be viewed in Figure 4.28.

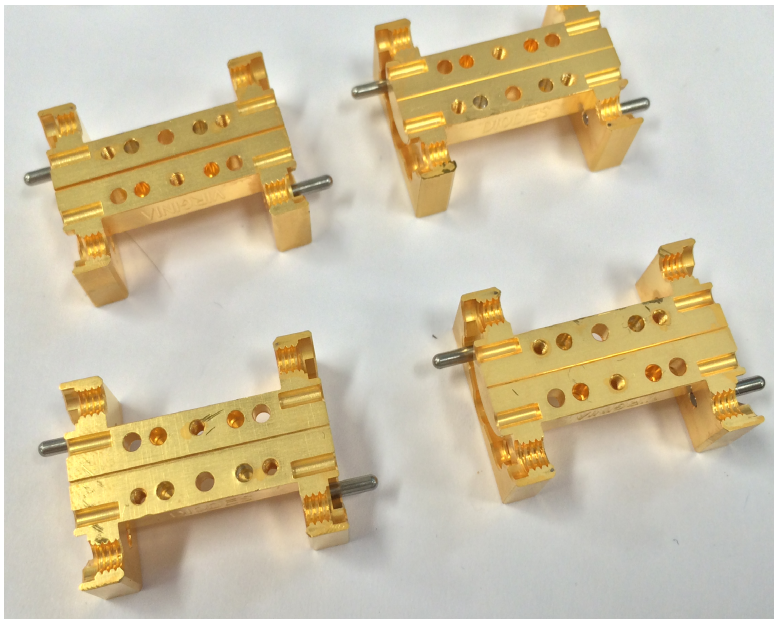


Figure 4.28: WR3.4 (left) and WR1.5 (right) waveguides from VDI made of Aluminum with a thin gold plating.

The waveguides are produced in 2-split blocks made of Aluminum with a thin gold plating. The left two halves belong to WR3.4 with groove dimensions of 0.864×0.432 mm, and the right to WR1.5 of 0.381×0.191 mm.

As soon as the purchased items were sent to CERN, they were rinsed with n-Hexane and anti-dust blowing was applied prior to coating. The NEG coating was realized by magnetron

4.6. NEG properties characterization above 200 GHz

sputtering but this time the waveguides were disassembled into two halves, since a wire cannot fit in such small dimensions. An alternative coating process was followed. The source with the inter-twisted wires of Ti-Zr-V is shown in Figure 4.29 (left) and the closed in-vacuum device on the right.



Figure 4.29: NEG sputtering setup on WR3.4 and WR1.5 waveguides.

The two halves of each waveguide were masked to avoid coating (as much as possible) outside the groove. Two coated halves of WR3.4, together with the dummy pieces for coating protection, are illustrated in Figure 4.30.

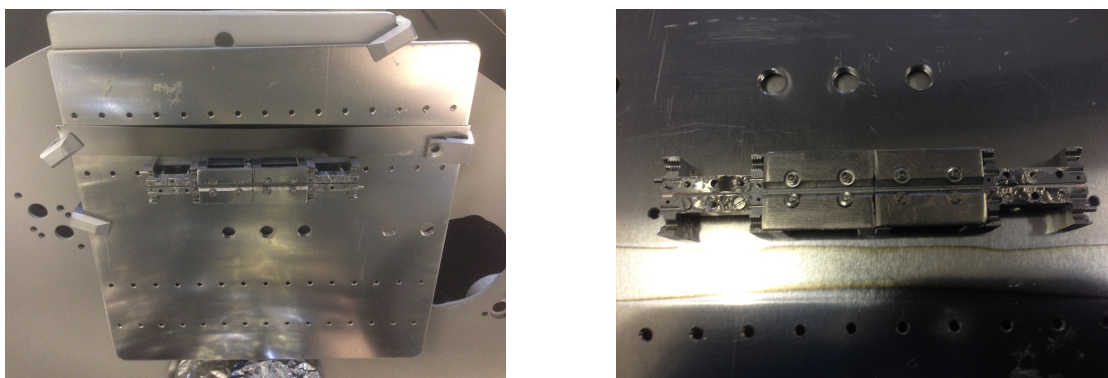


Figure 4.30: WR3.4 after NEG sputtering. In the middle, the two coated halves can be seen. On the left and right side, dummy pieces were used to protect coating on the side. The mask to prevent coating outside the waveguide's groove is also visible.

Full two-port S-parameter measurements were performed at VDI to measure the NEG-plated Aluminum waveguides. The setup can be seen in Figure 4.31.

The transmission coefficients S_{21} and S_{12} are measured. The waveguide is measured in one direction and then flipped 180 degrees and re-measured (named forward and reverse orientation). In Figure 4.32, the transmission S-parameters are plotted for the four WR3.4 waveguides. Measurements include S_{21} , as well as S_{12} parameters, in both forward and reverse orientation. For a reciprocal network, S_{mn} and S_{nm} are expected to be equal. Moreover, forward and reverse orientation should give the same results. For the prototype WR3.4 (1) (top-left plot and TRL

Chapter 4. Electromagnetic properties of NEG at high frequencies

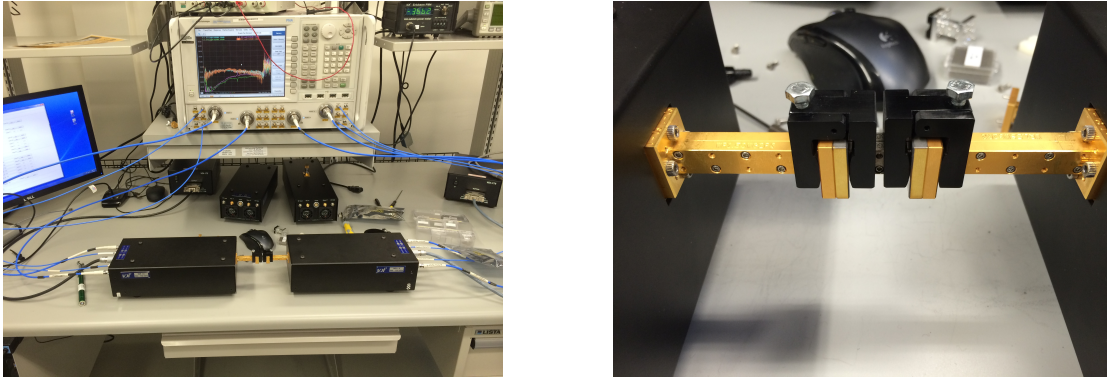


Figure 4.31: Measurement setup at VDI. A WR1.5 is connected with flanges to the VNA extenders of 500-750 GHz.

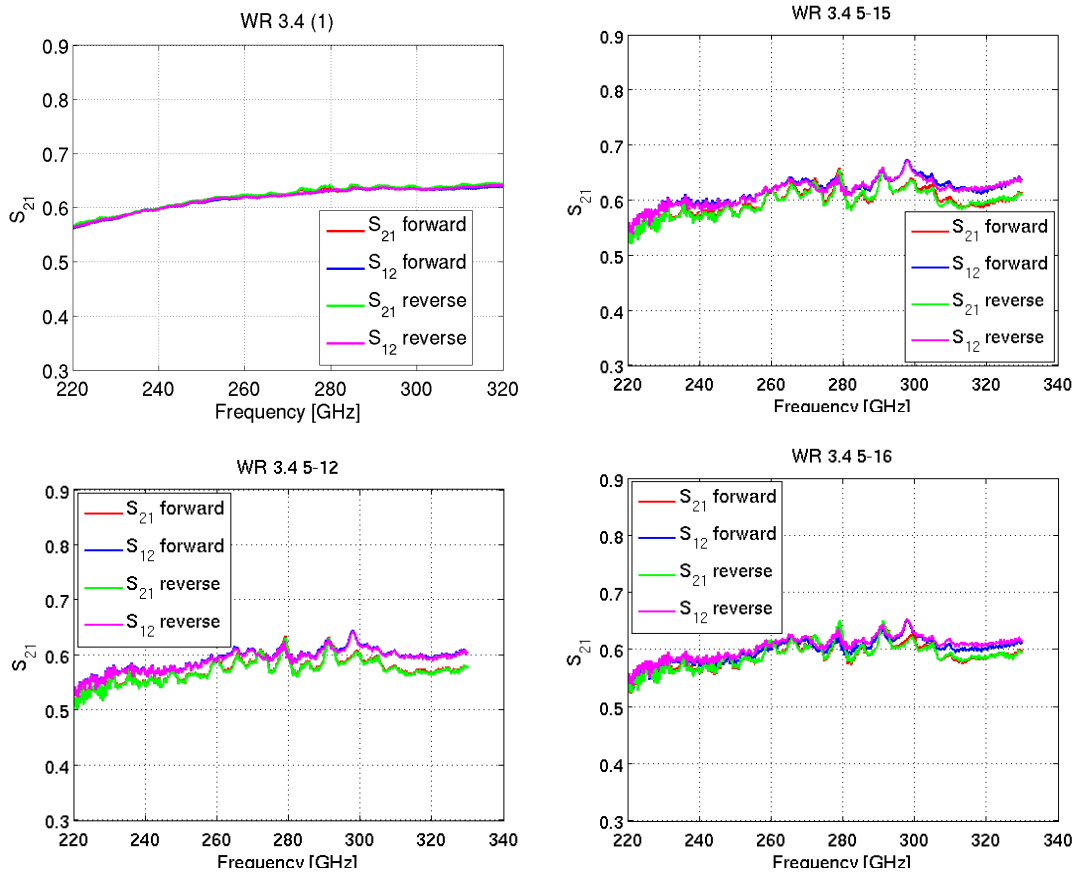


Figure 4.32: Transmission measurements for the four WR3.4 waveguides between 220-330 GHz.

calibration), the four measured parameters are close to each other. A larger discrepancy was found for the remaining three waveguides (Unknown Thru calibration was used): 5-12, 5-15 and 5-16. Results are very close in forward and reverse direction but there is a systematic difference between S_{21} and S_{12} in each orientation. This observation leads to the conclusion

4.6. NEG properties characterization above 200 GHz

that the difference cannot be related to the waveguide itself (since forward and reverse gave same results), but most likely it is related to a calibration error. The measurement uncertainty (connector repeatability, cable drift, e.t.c.) is estimated to be 5%. The WR3.4 (1) waveguide was measured first as a test. A different VNA, compared to 5-12, 5-15 and 5-16, was used. These three were measured using a different VNA and under the same calibration.

The WR3.4 model is implemented in CST, assuming a 3 μm thick NEG film. The simulation is done considering a DC conductivity of NEG equal to $\sigma_{\text{NEG}} = 0.57 \times 10^6 \text{ S/m}$. Using the same coating setup as the one used in the WR3.4 waveguides, NEG of various thicknesses was deposited on glass. Measurements of resistance gave DC values of conductivity scattered between $0.5 \times 10^6 \text{ S/m}$ and $0.7 \times 10^6 \text{ S/m}$. The error of the measurements is estimated around 15%. A difference is observed in the measured DC value compared to the previous measurements using a different coating setup, presented in 4.5.4. This is attributed to the different cathode used in each setup for the NEG deposition. The CST 3D model can be viewed in Figure 4.33.

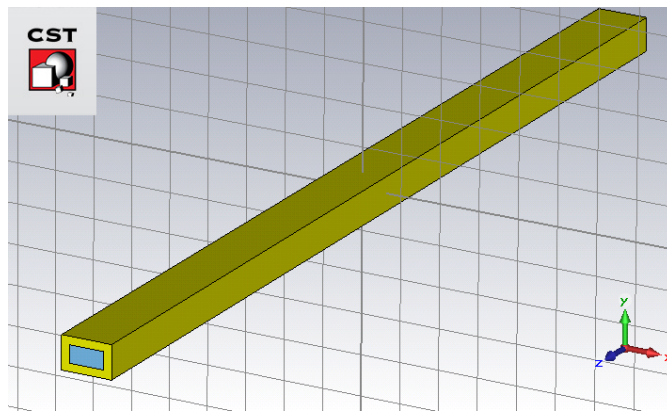


Figure 4.33: CST 3D model of a WR3.4. The 3 μm NEG-coated Aluminum is in yellow and the vacuum in blue.

In Figure 4.34, the CST simulated S_{21} is compared to the measurements. The measured losses are higher than CST prediction for a smooth waveguide by around 10%. The same method, as already described in 4.5.2, is applied to extract the effective conductivity by intersecting at each frequency simulation and measurements. The effective conductivity is plotted for each waveguide in Figure 4.35. In all four waveguides, the effective conductivity seems to decrease as frequency increases. The range of $\sigma_{\text{NEG}}^{\text{eff}}$ values lies between $0.46 \times 10^6 \text{ S/m}$ and $0.27 \times 10^6 \text{ S/m}$. For lower frequencies around 220 GHz, a 20% difference is observed between the DC conductivity value and measurements. This difference lies within the uncertainty of the experimental method. At higher frequencies, up to 330 GHz, this difference is further increased to around 45%.

Measurements of roughness with an optical profilometer revealed an average R_q of 0.2 μm . The skin depth varies between 1.4 μm and 1.15 μm across 220-330 GHz, thus not a significant reduction is expected due to surface roughness. The CST roughness model can explain a 6-7% reduction from the DC conductivity. Typical values of roughness in today's accelerator

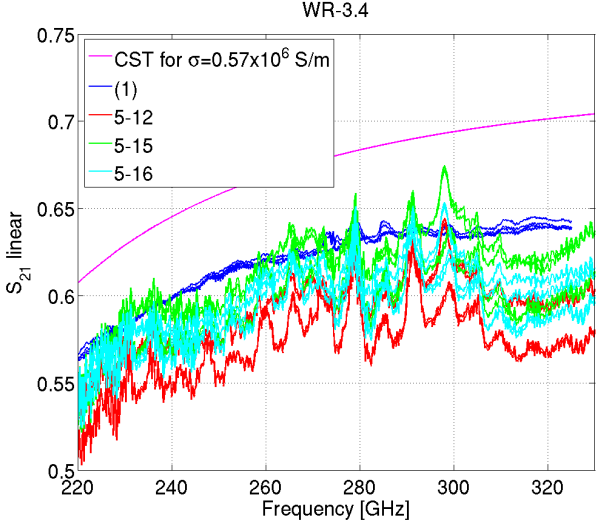


Figure 4.34: S_{21} comparison between CST (magenta) and the 4 measurements.

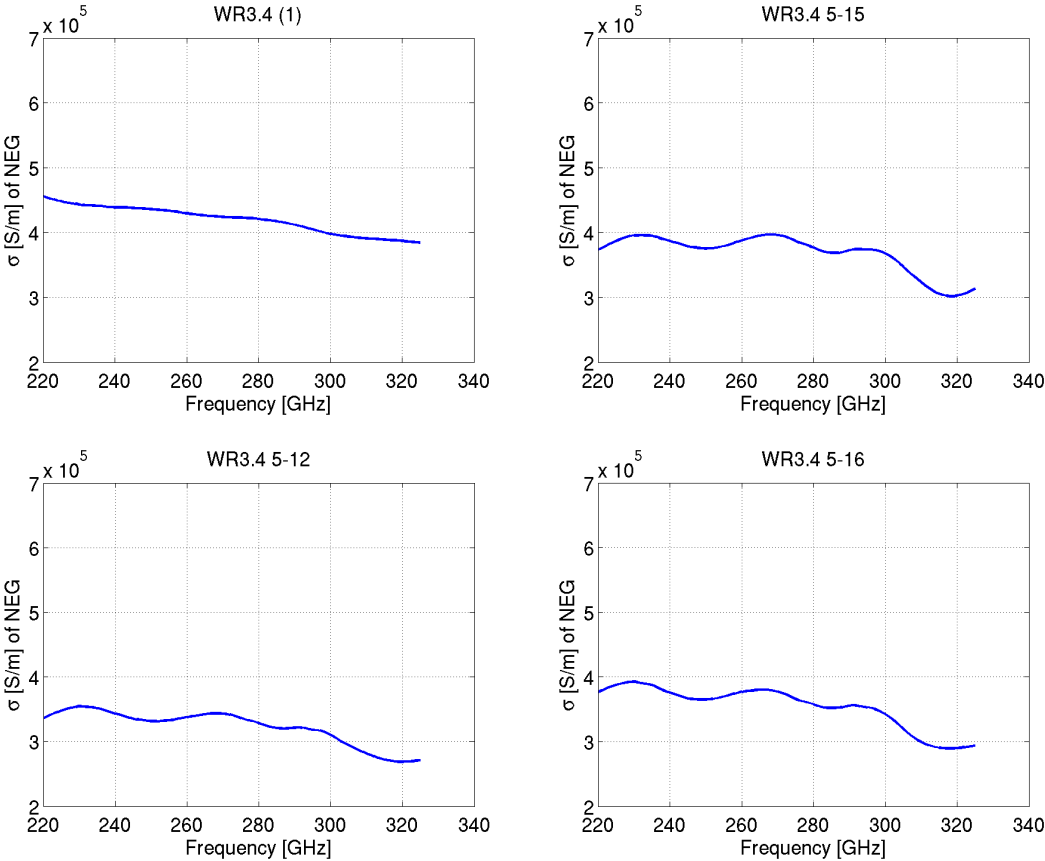


Figure 4.35: NEG effective conductivity between 220-330 GHz.

4.6. NEG properties characterization above 200 GHz

chambers are around $0.2 \mu\text{m}$ (LHC beam screen and SPS vacuum chamber). The roughness of the coating is dominated by the roughness of the substrate, therefore, for a NEG-coated StSt vacuum pipe (foreseen for the DRs), R_q of around $0.2\text{-}0.3 \mu\text{m}$ can be expected.

WR3.4 - second round measurements

Due to the noticeable measured difference in S_{21} between the prototype and the other three WR3.4 waveguides (Figure 4.32), a second round of measurements was done for 5-15 and 5-16. The idea was to crosscheck results using a third VNA. WR3.4 5-15 and 5-16 were re-measured using TRL calibration. The comparison is shown in Figure 4.36, where in black and red are the 5-15 and 5-16 waveguides measured with another VNA (round 2) and compared to the previous set of measurements (green and cyan). CST prediction is also included in the plot, for $\sigma_{\text{NEG}}^{\text{DC}} = 0.57 \times 10^6 \text{ S/m}$ (magenta), as well as the measurements of the first waveguide (blue) which were done with a different VNA than the other two.

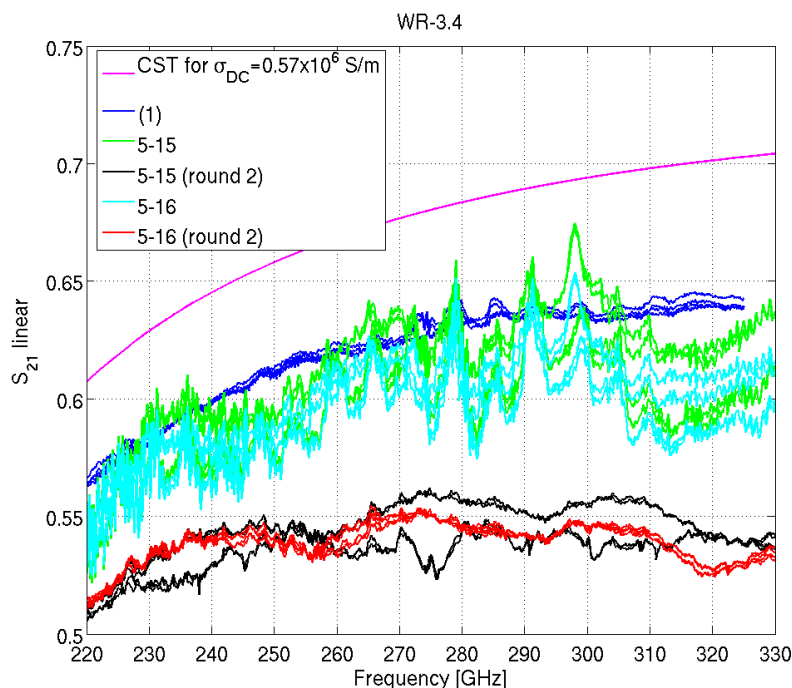


Figure 4.36: S_{21} comparison between CST (magenta), prototype (1) (blue), 5-15 and 5-16 waveguides (green and cyan) and 5-15, 5-16 waveguides using a different VNA (black and red).

A 10-15% sample-to-sample variance characterizes the S_{21} measurements that comes from the VNA itself.

The effective conductivity, as extrapolated from the two different network analyzers, is plotted in Figure 4.37 for 5-15 and 5-16. Measurements with different VNA showed a 10-15% uncertainty. As already observed in the first round, at lower frequencies, the extracted effective

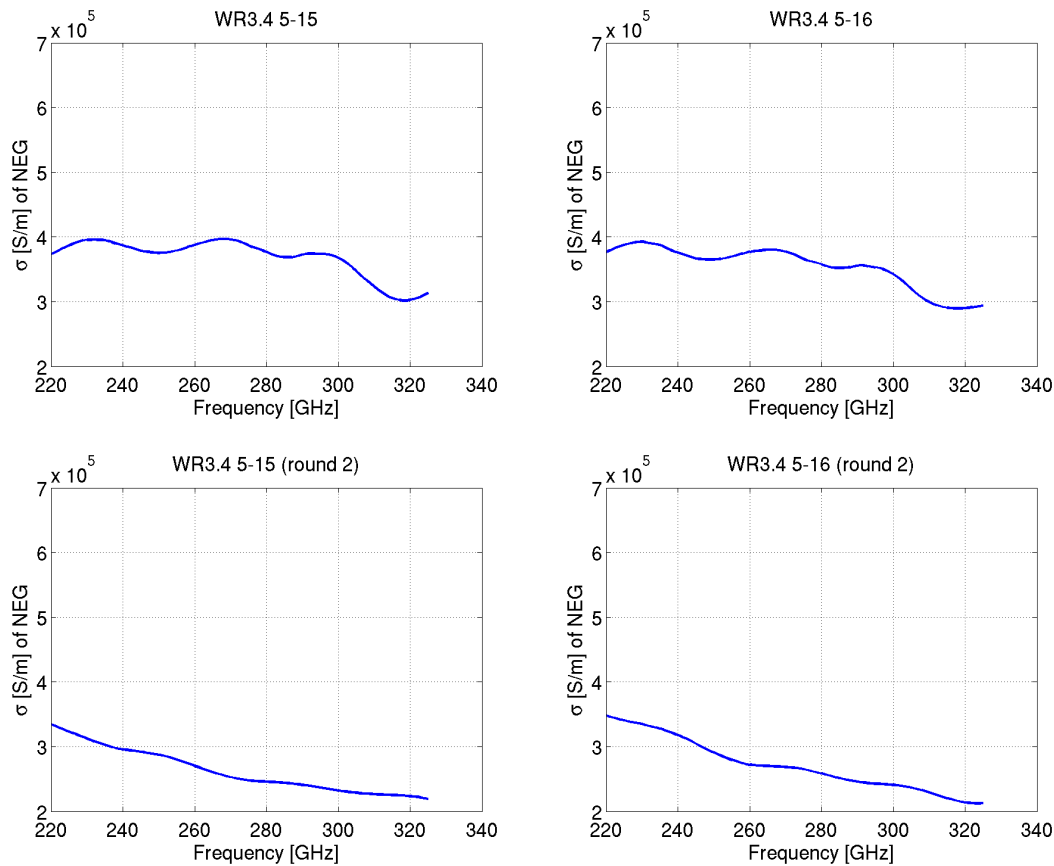


Figure 4.37: NEG effective conductivity between 220-330 GHz for 5-15, 5-16 measured with two VNA. Top plots correspond to the first round of measurements, bottom plots to the second round.

conductivity differs by around 20% from the DC value, which is within the accuracy of the experimental method, while at higher frequencies the difference is increased.

4.6.2 500-750 GHz: WR-1.5 waveguides

Measurements were also conducted for frequencies between 500-750 GHz. This is above the frequency spectrum of the bunch in the CLIC DR but could be important for the transverse motion. Moreover, measurements at higher frequencies could contribute essentially to the correct results interpretation between 10-11 GHz, as well as 220-330 GHz.

Three WR1.5 waveguides were purchased from VDI. The first one was used as a prototype to test the NEG coating. Similarly to the WR3.4 prototype, once it was cleaned with n-Hexane and anti-dust blowing, NEG coating was applied with targeted thickness of $6 \mu\text{m}$.

Once the coating process was completed, the halves were observed with an optical microscope. By optical microscopy, some defects on the coating became visible. To study in detail, the samples were also observed by SEM in different sites of interest along the coated groove. The

4.6. NEG properties characterization above 200 GHz

results can be seen in Figure 4.38.

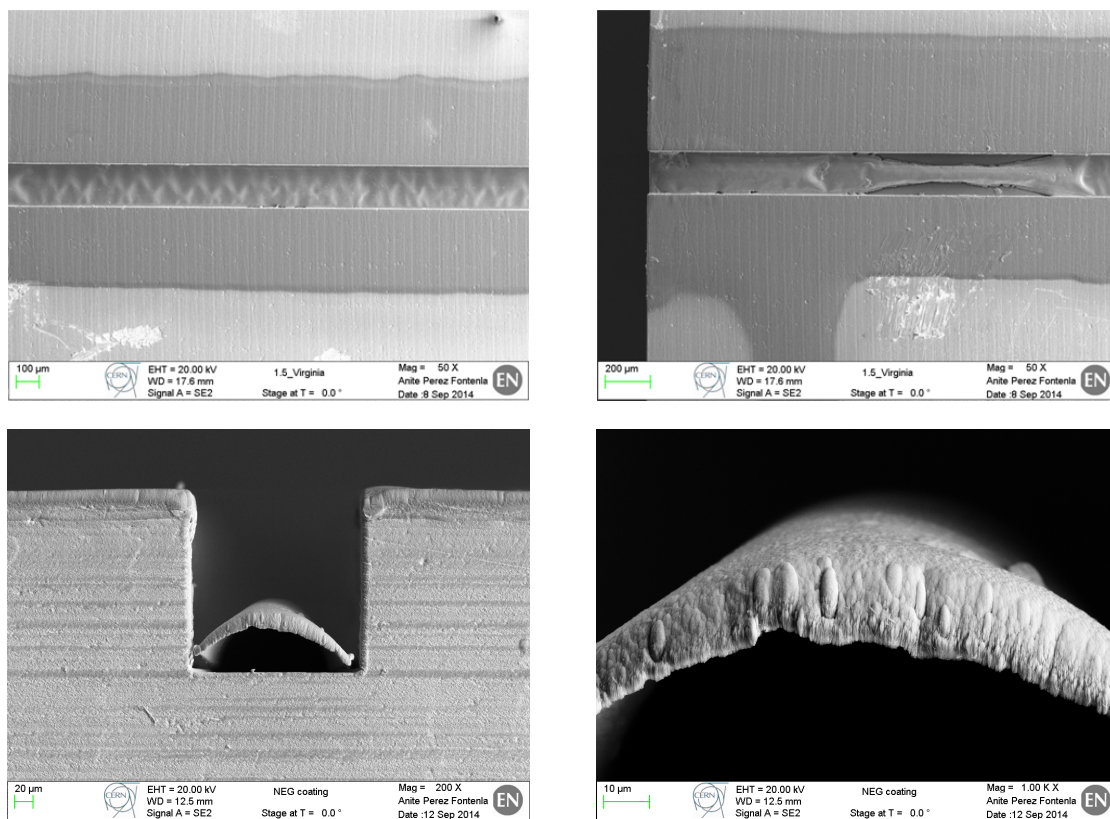


Figure 4.38: SEM pictures after NEG coating of WR1.5. The top photos are SEM results looking on the top of the groove, and bubbles were observed along the whole length. The bottom plots are SEM photos from the side view of the waveguide, where it is obvious that the coating is almost detached.

Bubbles were observed all along the groove and some parts seemed to be detached (top-right photo). That was confirmed with a side view of the coating (bottom plots) where the almost detached coating is clearly visible. Since the surface of the inner groove of the WR1.5 was of equal roughness and quality as the WR3.4, the attributed reason for the unsuccessful coating was the smaller groove dimension. WR1.5 has at least half the width and height of WR3.4, leading to more stress on the coating and causing difficulties of adherence. For the 2 remaining purchased WR1.5, a thinner coating of 3 μm was attempted. The result was successful adherence and no bubbles were observed along the groove.

Measurements of the S-transmission coefficients S_{21} and S_{12} were done at VDI for the 2 WR1.5 waveguides, both in forward and reverse direction using Unknown Thru calibration. The results of the measurements are presented in Figure 4.39.

The waveguide was modeled with CST considering DC conductivity of 0.57×10^6 S/m. Simulated S_{21} is compared to measurements of the 2 waveguides. The comparison can be viewed in Figure 4.40. In reality, more losses were observed than the CST prediction for a perfectly smooth waveguide.

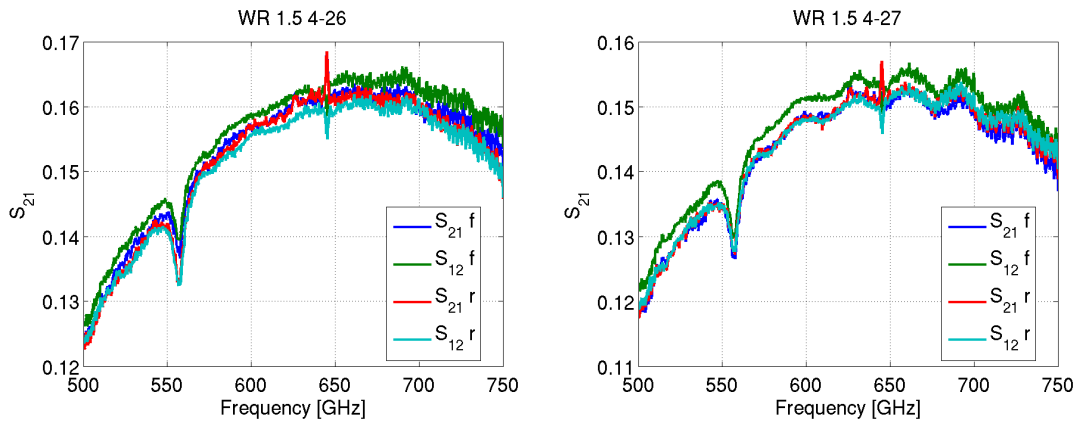


Figure 4.39: S_{21} measurements between 500-750 GHz for the 2 NEG-coated WR1.5 waveguides.

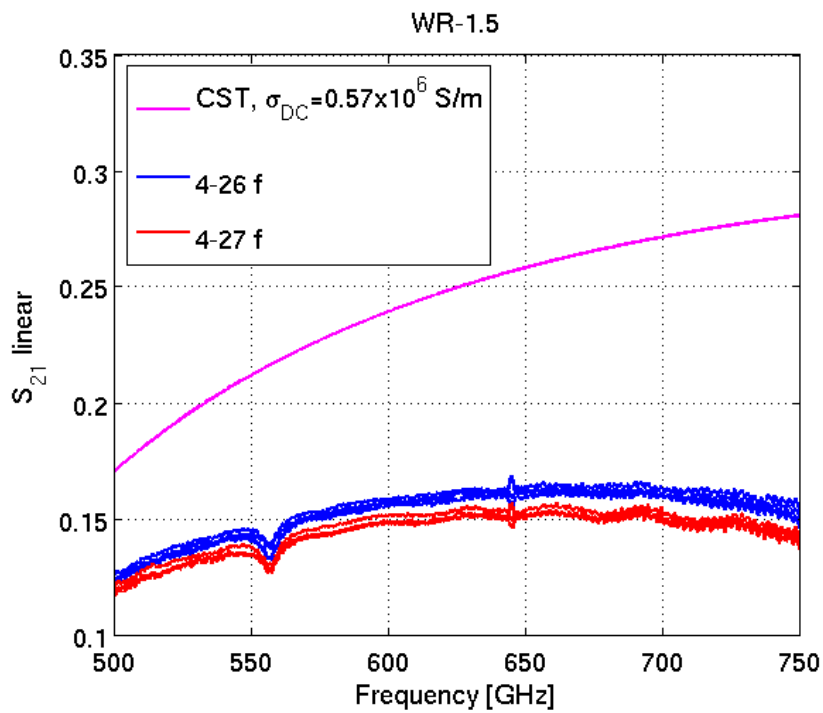


Figure 4.40: Comparison of S_{21} CST prediction with measurements along the two WR1.5 waveguides, named as 4-26 and 4-27 in forward orientation.

In Figure 4.41, the effective conductivity is shown as extracted for the 4-26 and 4-27 WR1.5 waveguides. The extracted values lie between 0.36×10^6 S/m and 0.2×10^6 S/m. A 35% difference from the DC conductivity is found at 500 GHz. The CST roughness model can explain a reduction of 20-22% from the DC value, for R_q of around $0.3 \mu\text{m}$ (as measured with the profilometer). Once more, the conductivity seems to reduce as frequency increases, up to 60% at 750 GHz.

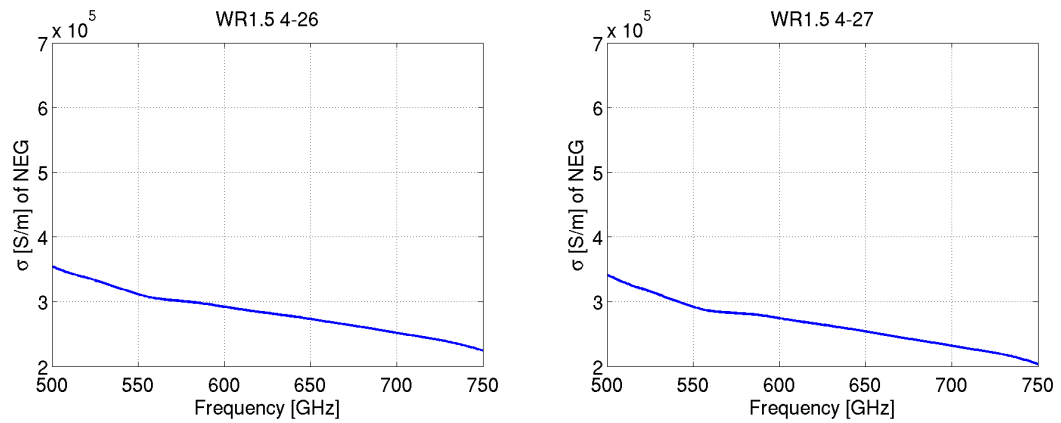


Figure 4.41: NEG effective conductivity at 500-750 GHz.

4.7 Effect of the non-uniform coating profile

The extracted NEG conductivity at lower frequencies, during all our measurements, agrees within 15-20% with the DC value. In all the frequency ranges of the measurements, 10-11 GHz, 220-330 GHz and 500-750 GHz, a reduction of conductivity has been observed as frequency increases. Around 10% reduction is noticed between 10 and 11 GHz compared to DC (see Figure 4.26), while the reduction is significantly stronger, about 45%, between 220 and 330 GHz and 60% between 500 and 750 GHz (see Figures 4.37 and 4.41). However, such big reduction cannot be explained by roughness in this frequency regime nor relaxation effects are expected below 10^{14} Hz for metals.

A systematic feature that was neglected in the CST simulations is the non-uniformity of the coating profile. So far, it was assumed to be constant, however XRF and SEM analysis revealed very non-uniform profiles for all waveguides that were used in the experiments. In order to investigate that the non-implementation of the non-uniform profile is responsible for the apparent conductivity drop, another simulation with CST was set up.

WR3.4 waveguide

SEM analysis on a WR3.4 waveguide, showed a variation between 5 and 10 μm along the wide part of the groove (with 10 μm in the center and 5 μm in the corners) and between 1 and 3 μm on the side walls of the groove, which is the least preferential direction during the coating process. The targeted thickness was 3 μm , but in reality we can see that the profile varies significantly. In order to simulate that, the idea is to divide the rectangular structure in CST into smaller blocks and apply coating of different thickness on the various blocks. The structure can be viewed in Figure 4.42.

The CST results from Figure 4.42, are intersected with the measurements and the results are shown in Figure 4.43.

We can see that in this case the slope of conductivity versus frequency has changed completely. Other simulations were set up with 1.5 μm coating thickness on the side walls or 1.8 μm . The

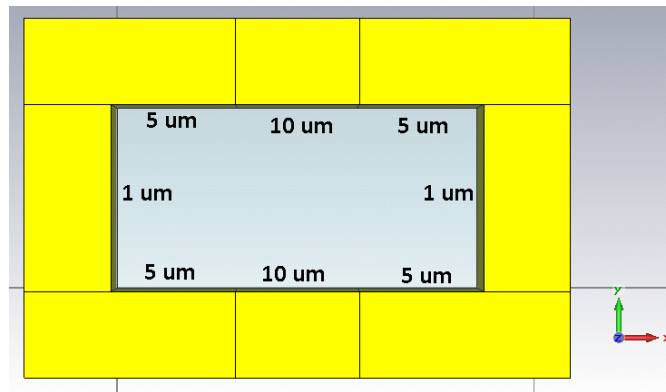


Figure 4.42: Front view of a WR3.4 waveguide separated in various blocks to apply NEG coating with different thickness. In the wider part of the groove, SEM indicated variation of the thickness from 5 to 10 μm , with the maximum value in the center. For the side walls, the coating is thinner, around 1 to 3 μm .

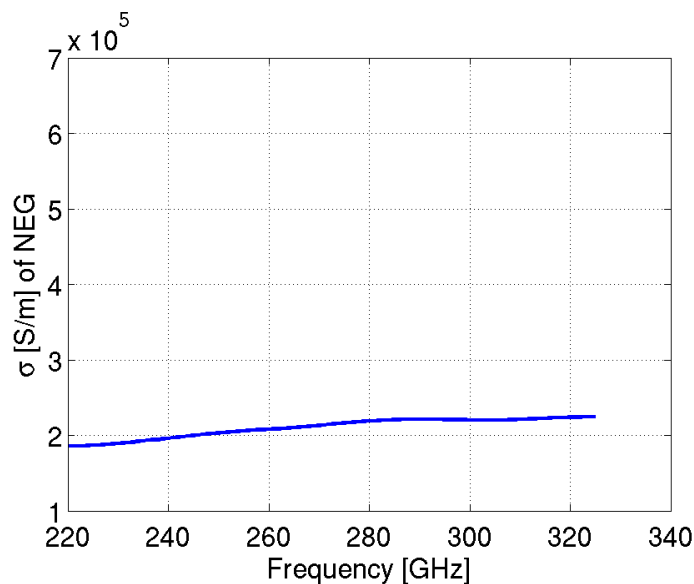


Figure 4.43: NEG effective conductivity between 220 and 330 GHz for a non-uniform profile. For the wider part of the groove, coating of 5 and 10 μm was considered, while 1 μm was assumed for the side walls.

extracted conductivity now is shown in Figure 4.44. The side wall thickness plays an important role in the extracted results. The sensitivity becomes evident from Figure 4.44.

To further investigate the effect of the non-uniformity on the side walls, another simulation was performed by dividing the sides in three parts with coatings of 1.5, 2 and 1.7 μm . The coating in the wider part is the same as in Figure 4.42. The structure simulated with CST can be seen in Figure 4.45.

4.7. Effect of the non-uniform coating profile

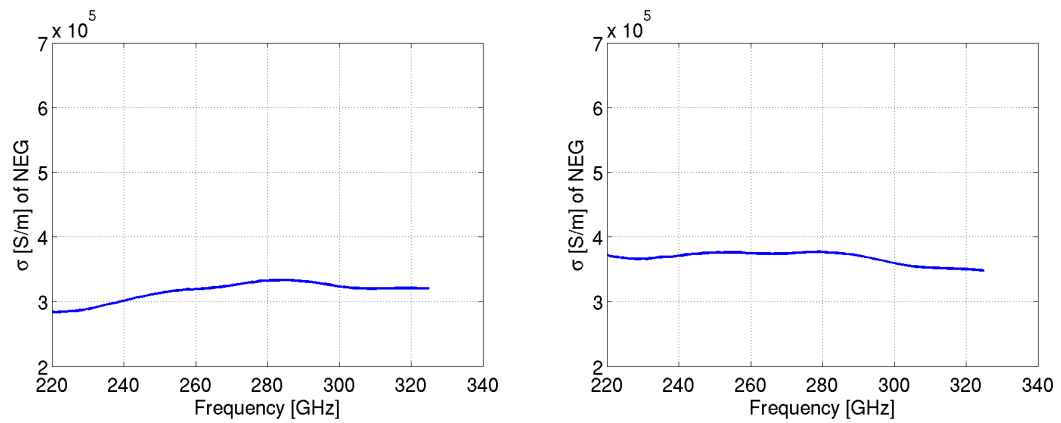


Figure 4.44: NEG effective conductivity between 220 and 330 GHz for a non-uniform profile. For the wider part of the groove, coating of 5 and 10 μm was considered, while 1.5 μm was assumed for the side walls (left plot) and 1.8 μm (right plot).

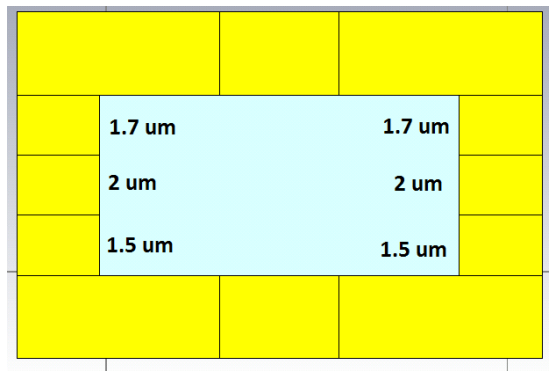


Figure 4.45: Front view of a WR3.4 waveguide separated in various blocks to apply NEG coating with different thickness. In the wider part of the groove, 5 and 10 μm are considered, similarly to the previous simulation. For the side walls, 1.5, 1.7 and 2 μm are assumed.

The result from the intersection is shown in Figure 4.46. Conductivity is varying by around 7%. A milder frequency dependent behavior of conductivity is observed, compared to the 45% variation found in Figure 4.37.

We can conclude therefore, that the correct implementation of the coating profile plays a crucial role in the seeming conductivity behavior. This behavior is due to a systematic error in the intersection of simulation with measured data, that originates from the inability to properly model the non-uniform 3D coating profile. In this section we saw that the apparent conductivity drop versus frequency obtained so far (assuming a constant coating thickness in CST) is subject to change, once the profile is set to non-uniform.

The results between 220-330 GHz are summarized in Figure 4.47, where the extracted conductivity is also compared to the measured DC values (with a 15% error) and roughness effects. We now use the extracted value of 0.35×10^6 S/m (which has an error band of around 15% if all four WR3.4 waveguides are considered), to feed it back to the CST simulation and compare it

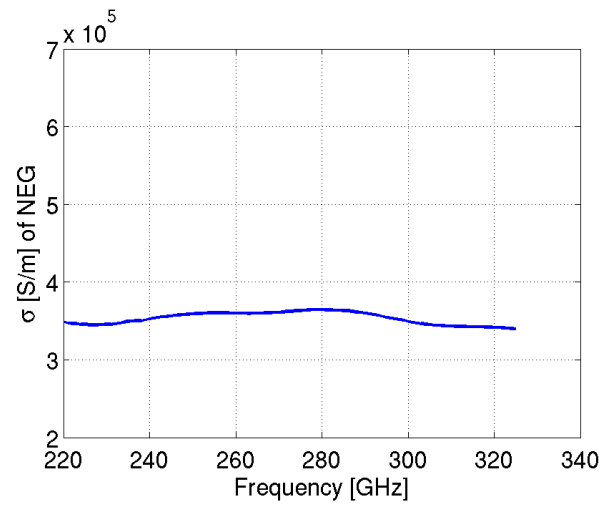


Figure 4.46: NEG effective conductivity between 220 and 330 GHz for a non-uniform profile also on the side walls.

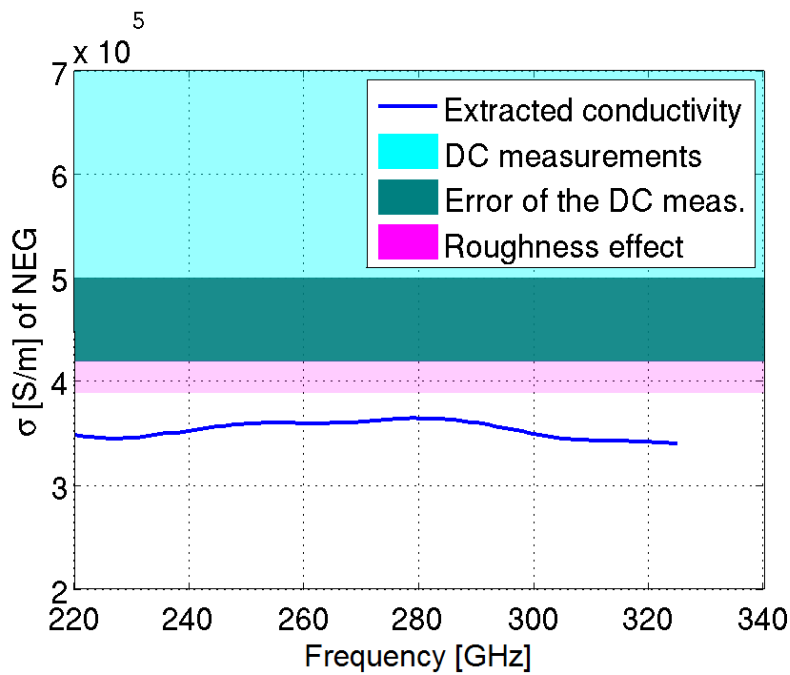


Figure 4.47: NEG effective conductivity between 220 and 330 GHz for a non-uniform profile, compared to DC measurements and roughness effects.

to the measured S_{21} . The outcome of the comparison is presented in Figure 4.48. As expected, there is a good agreement between measurements and CST for the conductivity extracted from the method, and using a non-uniform profile.

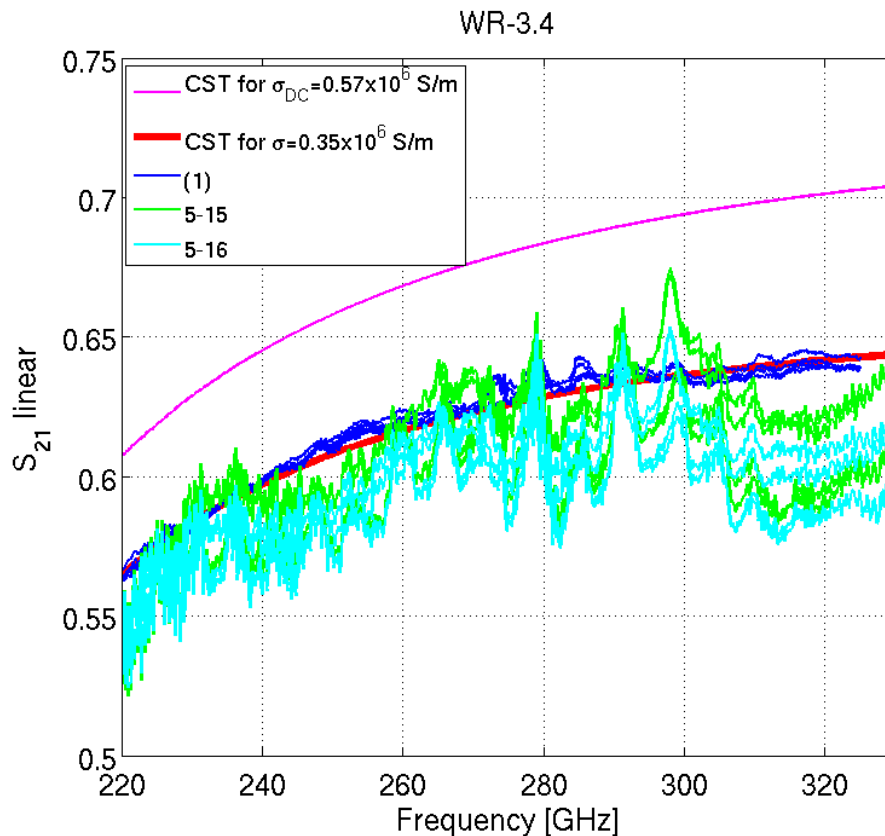


Figure 4.48: S_{21} comparison between CST for $\sigma_{DC} = 0.57 \times 10^6$ S/m (magenta), CST for $\sigma_{eff} = 0.35 \times 10^6$ S/m (red), prototype (1) (blue), 5-15 and 5-16 waveguides (green and cyan). As expected, CST and measurements agree very well if the conductivity extracted from the method is used.

WR1.5 waveguide

SEM analysis on a WR1.5 waveguide, showed a variation between 4 and 7 μm along the wide part of the groove (with 7 μm in the center and 4 μm in the corners) and between 0.5 and 1.5 μm on the side walls of the groove. The same idea of dividing the waveguide in CST into several blocks is followed, in order to mimic the non-uniformity of the coating. The structure can be viewed in Figure 4.49.

The results from the intersection are displayed in Figure 4.50. Conductivity is varying by around 15%. A milder frequency dependent behavior of conductivity is observed, compared to the 60% variation found in Figure 4.41.

The extracted conductivity is around 0.2×10^6 S/m, and therefore around 37% lower than the effective conductivity explained by roughness. This value is still within the accuracy of the method. Feeding the extracted value into CST, the comparison with the measured data can be seen in Figure 4.51.

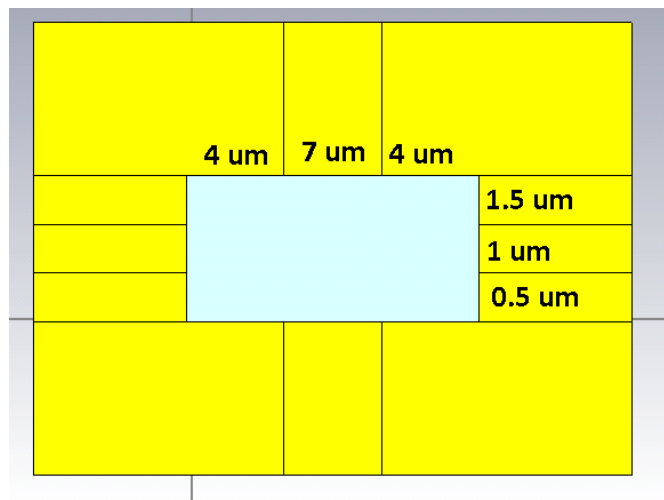


Figure 4.49: Front view of a WR1.5 waveguide separated in various blocks to apply NEG coating of different thicknesses. In the wider part of the groove, SEM indicated variation of the profile from 4 to 7 μm, with the maximum value in the center. For the side walls, the coating is thinner, around 0.5 to 1.5 μm.

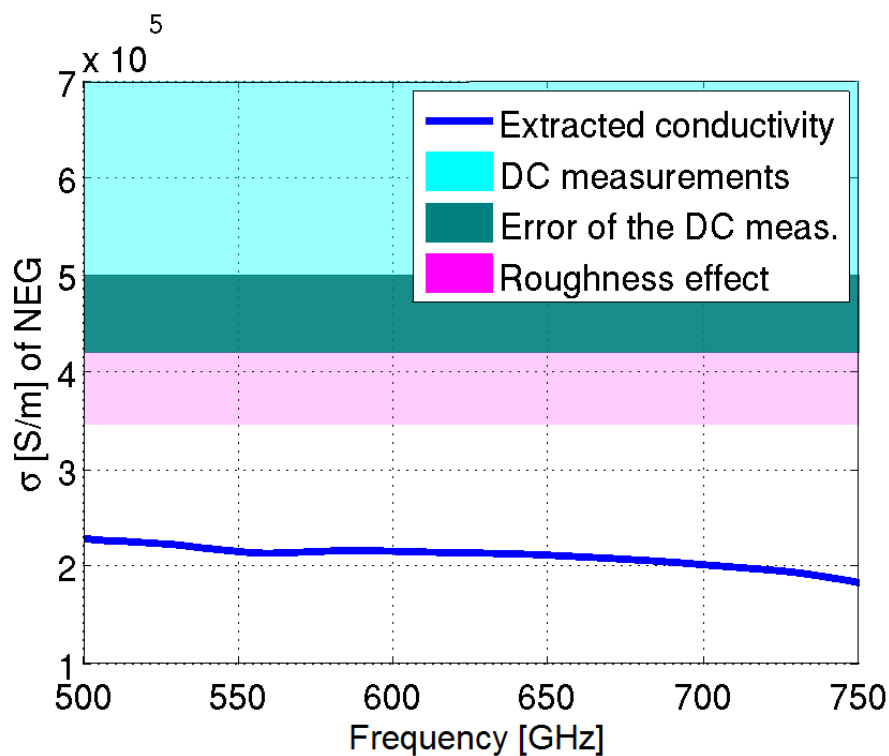


Figure 4.50: NEG effective conductivity between 500 and 750 GHz for a non-uniform profile, compared to DC measurements and roughness effects.

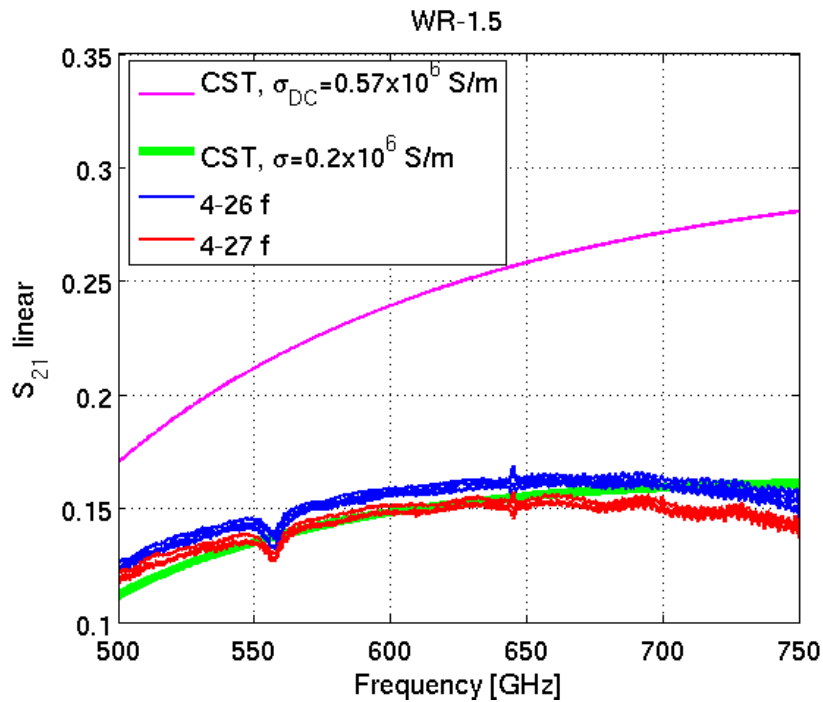


Figure 4.51: Comparison of S_{21} CST simulation assuming σ_{DC} with measurements along the two WR1.5 waveguides, named as 4-26 (blue) and 4-27 (red) in forward orientation. The CST simulation of S_{21} for the extracted conductivity 0.2×10^6 S/m is also shown (green), in good agreement with the measurements.

Conclusions on the material characterization

The experimental method, successfully benchmarked in X-band using StSt and Cu waveguides, was applied to characterize NEG conductivity in several frequency ranges: 10-11 GHz, 220-330 GHz and 500-750 GHz.

The extracted conductivity agrees within 10-15% with the DC value, which lies within the accuracy of the measurements. In particular, from 10 to 11 GHz, the conductivity is found to be $(1 \pm 0.2) \times 10^6$ S/m. At higher frequencies, the extracted conductivity is about 20% lower compared to DC value, that can be explained partially by the effect of roughness, the non-uniformity of the profile and the measurement accuracy itself. The appearing conductivity drop, as frequency increases, is attributed to the incapability of the simulation to consider the real 3D profile of the coating.

As NEG properties were characterized for the first time at such high frequencies, an important conclusion is that the effective conductivity to be considered can be significantly lower than the DC conductivity, especially at high frequencies (hundreds of GHz), even if relaxation effects are still not important in this frequency range.

4.8 Effect on the transverse impedance budget of the DRs

The original estimation of the transverse impedance budget of the DR, assumed that the conductivity of NEG is 1×10^6 S/m, which corresponds to the DC value measured in the past. The budget under these considerations, was found to be 16 and 4 M Ω /m in the horizontal and vertical plane for zero chromaticity, as presented in 3.3.2. For slightly positive chromaticity, $\xi_{x,y} = 0.02$, the budget was estimated at 2 and 1 M Ω /m.

The budget is now re-evaluated assuming a worst case scenario for the NEG effective conductivity, that is 0.3×10^6 S/m, in order to study the effect when the conductivity at high frequencies is different than what usually assumed.

The relative tune shift in the transverse planes with respect to the zero-current tune and normalized to the synchrotron tune Q_s is plotted, for zero chromaticity, as a function of transverse shunt impedance in Figures 4.52 and 4.53.

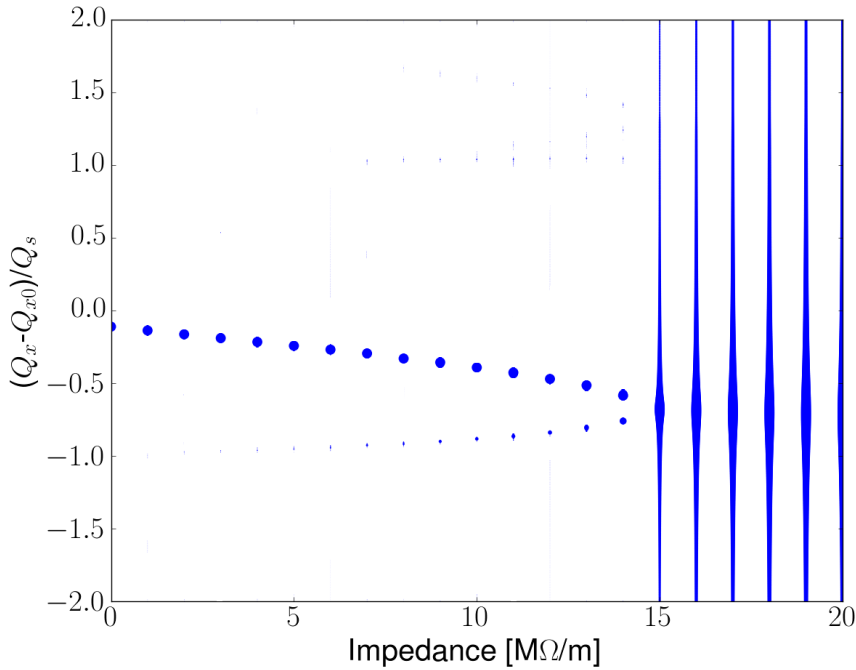


Figure 4.52: Mode spectrum of the horizontal coherent motion for zero chromaticity, as a function of transverse shunt impedance. The TMCI threshold is at 15 M Ω /m.

We can observe the TMCI threshold at 15 M Ω /m in the horizontal and 3 M Ω /m in the vertical plane. The model of the DR now accounts for a different resistive wall impedance, due to the lower NEG conductivity assumed. A 1 M Ω /m reduction is observed in the budget estimate in both transverse planes, compared to the thresholds previously computed for NEG conductivity of 1×10^6 S/m. For slightly positive chromaticity, the thresholds remain the same.

It is important therefore, at such high frequencies, to consider a lower NEG conductivity than the DC for beam dynamics simulations, accounting for roughness effects and non-uniformity

4.8. Effect on the transverse impedance budget of the DRs

of the profile. This could impact the resistive wall impedance and consequently the impedance budget estimate.

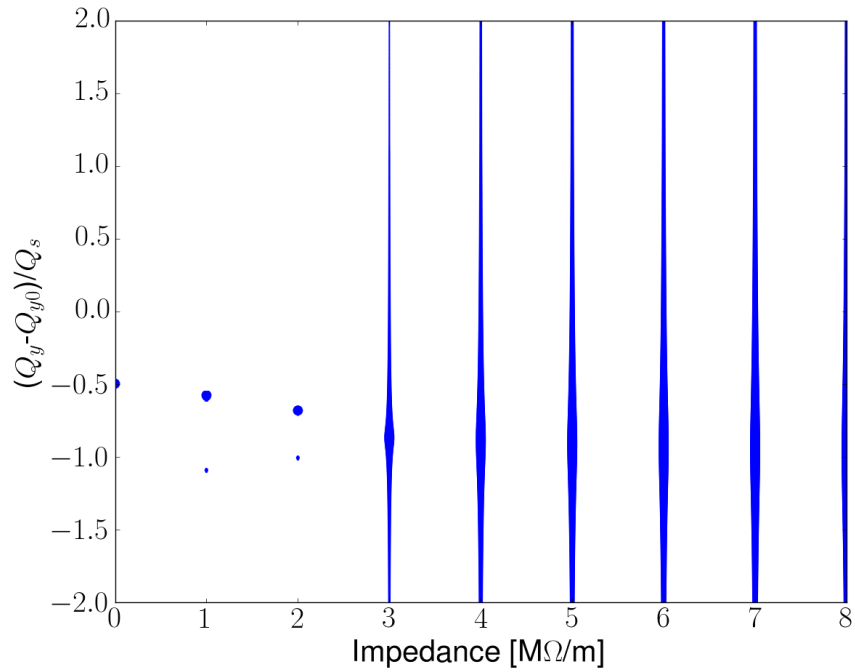


Figure 4.53: Mode spectrum of the vertical coherent motion for zero chromaticity, as a function of transverse shunt impedance. The TMCI threshold is at 3 $\text{M}\Omega/\text{m}$.

5 Studies on existing and future light sources

5.1 Single bunch measurements in the ALBA storage ring

There has been an effort to bring together scientific communities of synchrotron light sources, storage rings, damping rings as well as e^+ / e^- ring colliders in order to identify and promote common work on topics affecting the design of low emittance electron and positron rings. The state of the art in design of accelerator systems, especially in X-ray storage rings, has already approached the goals of damping rings for linear colliders and future e^+ / e^- ring collider projects. Existing light sources are targeting at more and more aggressive parameters to stay competitive. Machines aiming at ultra low emittances face similar beam physics and technical challenges. A strong collaboration between X-ray storage rings, damping rings and e^+ / e^- ring colliders has been established. Within this framework, a collaboration began between the CLIC DR and the ALBA light source.



Figure 5.1: The ALBA storage ring in Barcelona, Spain.

The ALBA storage ring (shown in Figure 5.1) is a 3 GeV third generation synchrotron light source in Barcelona (Spain). ALBA is optimized for high photon flux density with a beam

emittance of 4.5 nm.rad and a large number of straight sections for insertion devices in a relatively small circumference of 268.8 m. The injector complex consists of a 100 MeV Linac and a full energy Booster with a rather small emittance of 9 nm.rad, which ramps the electron beam up to 3 GeV in a 3 Hz cycle. The Linac had been commissioned in 2008 and the Booster in 2010 and there are 7 beam lines currently available for users [72]. For comparison, parameters of the ALBA storage ring are given together with the CLIC DR in Table 5.1. For ALBA, the 0-current value of the bunch length is listed and the RF voltage used during the measurements.

Table 5.1: Comparison of the CLIC DR and ALBA main parameters.

Parameters	DR@3 TeV	ALBA
Energy [GeV]	2.86	3
Circumference [m]	427.5	268.8
RF voltage [MV]	5.1	2.1
Damping time x/y [ms]	2/2	4.1/5.3
Bunch population	4.1×10^9	5×10^9
Horizontal normalized emittance [nm.rad]	456	26680
Vertical normalized emittance [nm.rad]	4.8	133
Bunch length [mm]	1.8	6.2
Momentum compaction factor [10^{-4}]	1.3	8.8

The measurements proposed target to benchmark the simulation tools (used so far for the CLIC DR) and in parallel, to validate the existing transverse impedance model of ALBA.

5.1.1 TMCI measurements at 0 chromaticity and HEADTAIL simulations

In order to crosscheck the transverse impedance model at ALBA, single bunch tune shift and instability thresholds were studied in the vertical plane. Chromaticity was set to zero and RF voltage at 2.1 MV. Measurements are compared to simulations in which the developed impedance model was implemented.

During the measurements, a single bunch was injected in ALBA and its current was increased from 1 mA in order to find the instability threshold. For the betatron tunes monitoring, two identical $\lambda/4$ stripline Beam Position Monitors (BPMs) are used. The $\lambda/4$ electrodes are used for white noise signal excitation and tune measurements, matched to 50Ω [73, 74]. The tunes are then computed by applying a FFT on the turn-by-turn position measurements. The tune shift measurements as a function of the bunch current were performed for closed, as well as, open in vacuum undulators (IVUs). In Figure 5.2, the tune monitor results are plotted for different bunch currents and the case of closed IVUs. The main betatron tune (highest amplitude), or else mode $m = 0$, shifts down, while another mode appears in the tune monitor, $m = -1$, just before the instability onset. A few other radial modes also seem to be visible from the monitor signal. A TMCI was observed at 8.8 mA when mode 0 and -1 coupled and immediate beam loss occurred.

5.1. Single bunch measurements in the ALBA storage ring

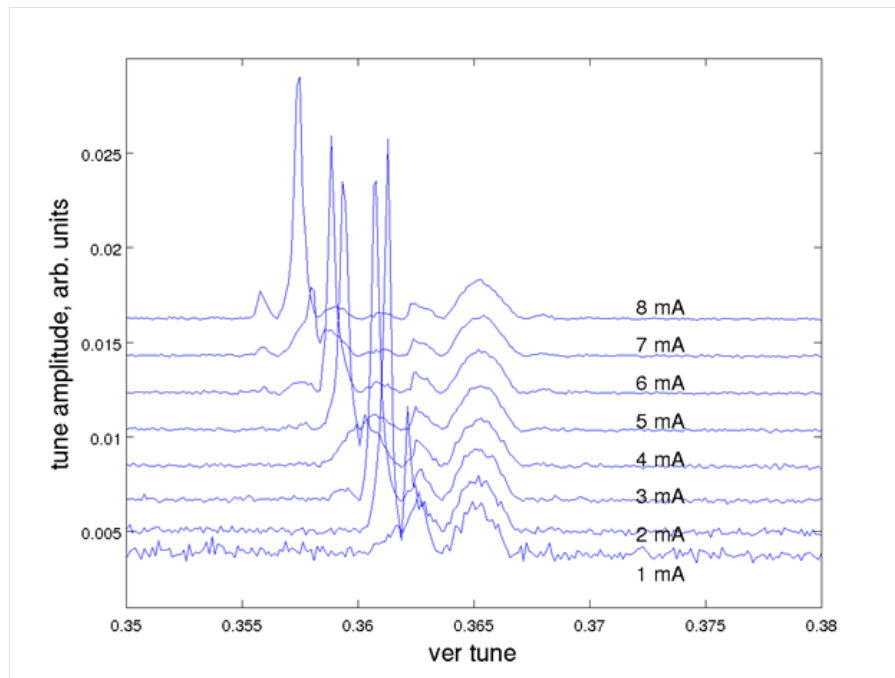


Figure 5.2: Tune monitor for closed IVUs [75]. Mode 0 shifts down as current increases and mode -1 appears before the instability onset (8.8 mA).

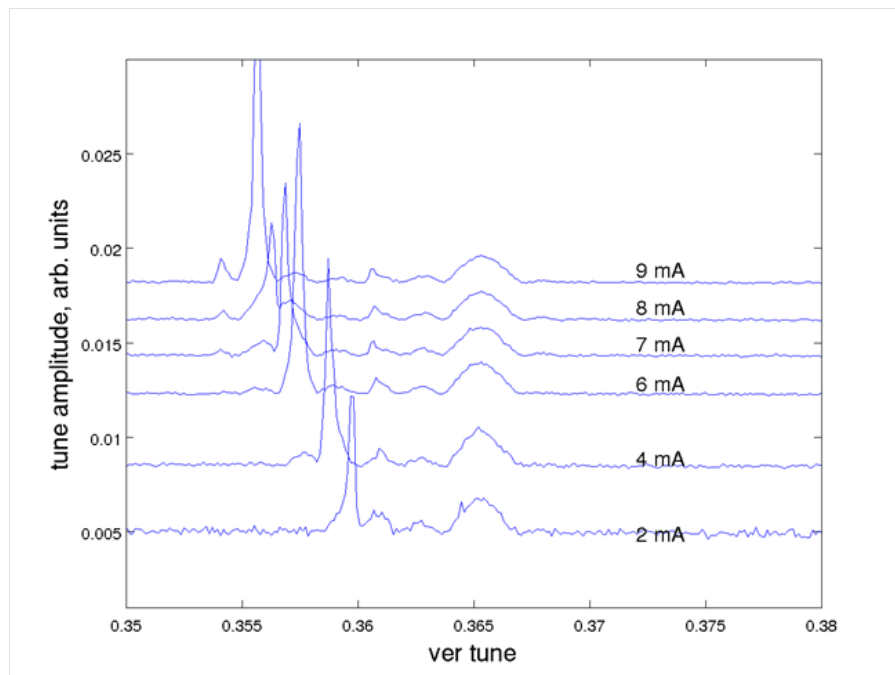


Figure 5.3: Tune monitor for open IVUs [75]. Mode 0 shifts down as current increases and mode -1 appears before the instability onset (9.8 mA).

The same set of measurements was repeated after opening the two IVUs. The undulators have 5.6 mm full gap which opens to 30 mm. The tune monitor results are shown in Figure 5.3 above. A higher instability threshold was measured at 9.8 mA, i.e. 1 mA higher compared to the closed IVUs. The instability is triggered by mode coupling between $m = 0$ and $m = -1$. A higher TMCI threshold was expected since the resistive wall transverse impedance is inversely proportional to the third power of the pipe radius [10]. For a larger aperture, when the IVUs are open, a smaller transverse resistive wall impedance is expected. Thus, the measurement's result is consistent with theory.

During the MD, the bunch length was monitored using a streak camera [76–78]. Bunch lengthening was observed due to potential well distortion [10, 79]. Results are plotted in Figure 5.4.

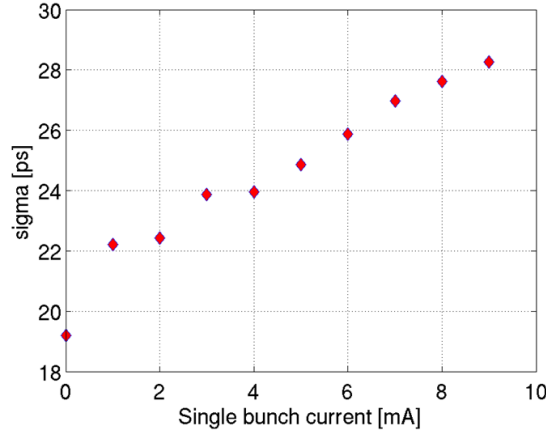


Figure 5.4: Bunch lengthening due to potential well distortion.

Since the bunch length increases as a function of current, the synchrotron tune will also change. Taking into account the change of length and tune is an essential ingredient in the interpretation of the measurements with simulations. In order to calculate the change of the synchrotron tune as a function of the beam intensity, the longitudinal matching condition [80] is used

$$\frac{R|\eta|\sigma_\delta}{Q_s\sigma_z} = 1, \quad (5.1)$$

$$Q_s = \frac{R|\eta|\sigma_\delta}{\sigma_z}, \quad (5.2)$$

where $R = 42.6$ m is the machine radius, $\eta = 8.8 \times 10^{-4}$ the slippage factor, $\sigma_\delta = 0.0012$ the momentum spread assumed to be constant to its equilibrium value, Q_s the synchrotron tune and σ_z the rms bunch length in m. Keeping the rest of the parameters unchanged and varying the rms bunch length according to the data of Figure 5.4, Eq. 5.2 estimates the change of the synchrotron tune (Figure 5.5).

5.1. Single bunch measurements in the ALBA storage ring

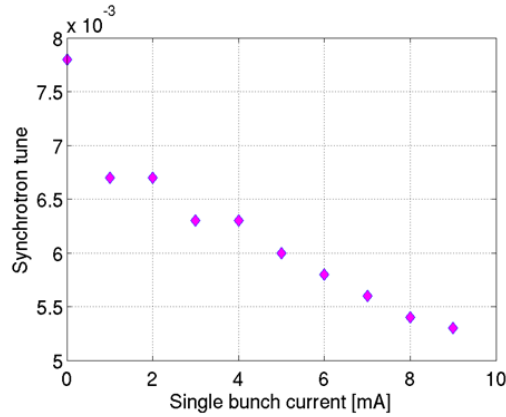


Figure 5.5: Synchrotron tune shift as a function of current.

HEADTAIL simulations

The current developed impedance model of ALBA was used as input in HEADTAIL simulations. The model includes four BBR and six multi-layer resistive wall contributors (dipolar and quadrupolar terms) [81, 82]. The model used in HEADTAIL does not yet include the stripline kickers. The frequency, quality factor and shunt impedance parameters of the four BBRs are listed in Table 5.2.

Table 5.2: BBR parameters for the ALBA transverse impedance model.

Frequency [GHz]	Quality Factor	Shunt Impedance [$M\Omega/m$]
1.81	14.56	0.26
7.72	0.32	0.014
8.9	33.2	0.008
56.1	1.72	0.037

The details of the RRW contributors are summarized in Table 5.3. The transverse wake functions, required for HEADTAIL simulations, are calculated with ImpedanceWake2D. The total wake function model is plotted in Figure 5.6.

Table 5.3: RRW contributors in the ALBA transverse impedance model.

Layers	Length [m]	Half Gap [mm]	β_x [m]	β_y [m]
Vacuum chamber (StSt)	201.4	14	7.89	6.2
IVUs (Cu/Ni)	4	3	2.22	1.67
1.5 μm NEG-coated Al chamber	8.1	4	2.37	1.87
Superconducting wiggler (Cu)	2.5	4.2	2.24	1.69
Dipole chamber (StSt)	44.3	14.4	0.82	21.53
Injection section chamber (StSt)	4	11.5	11.5	6.51

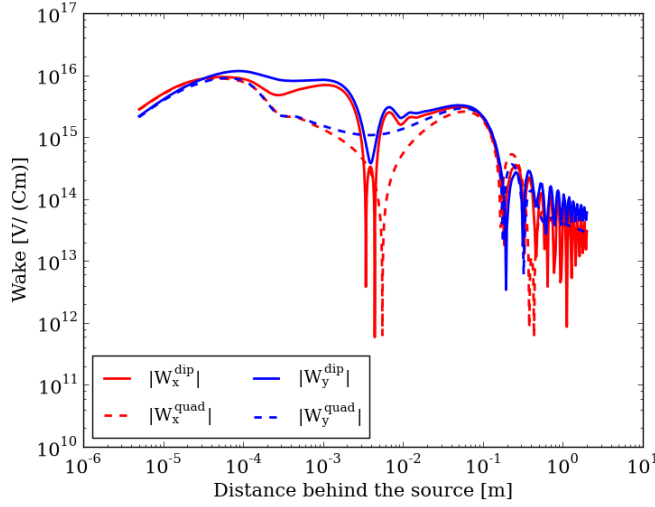


Figure 5.6: Transverse wake function model in HEADTAIL.

The relative tune shift with respect to the zero-current tune and normalized to the synchrotron tune is plotted in Figure 5.7, together with the measured data for closed IVUs (in red).

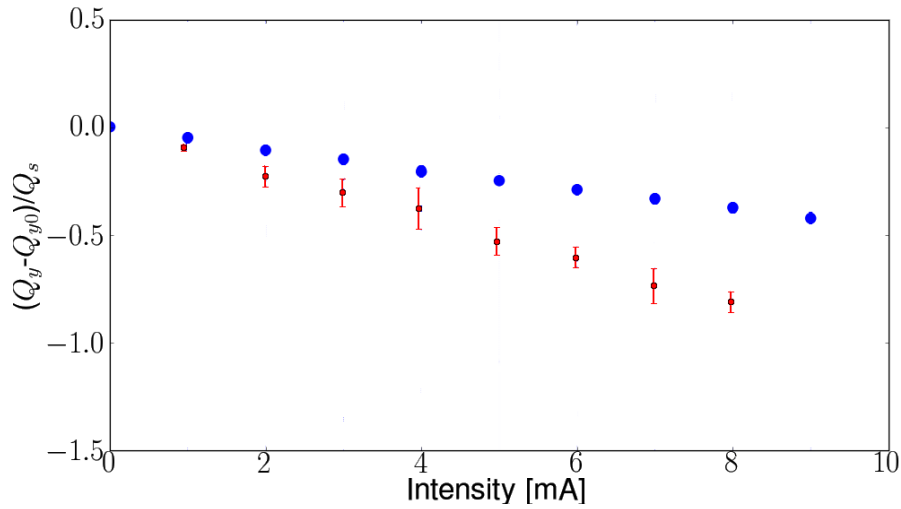


Figure 5.7: Normalized tune shift as predicted with HEADTAIL simulation (blue) based on the current impedance model and as measured (red) when the IVUs were closed.

During the measurements, twenty acquisitions take place at each intensity. A FFT is applied on the centroid data for all the acquisitions per intensity and then averaged. The main tune corresponds to the maximum while the error bar is calculated as the full width at half maximum (FWHM) divided by 2.355 of the tune peak. Mode 0 is observed to move but around 60% impedance is missing to explain the measured tune shift. Bunch lengthening was taken into account in the HEADTAIL simulations.

The first comparison between measurements and simulation revealed a lack of impedance in

5.1. Single bunch measurements in the ALBA storage ring

the existing model. Although an agreement within 40-50% is considered satisfactory, there is potential for improvement.

A parameter scan was done with HEADTAIL to quantify the missing impedance that could explain the measured TMCI thresholds for closed and open IVUs. As usual for broad band resonator models, we choose a resonant frequency close to the beam chamber's cut-off frequency (~ 1 GHz) and a quality factor of 1. Fixing these parameters, the transverse shunt impedance is scanned to match the measured thresholds. A shunt impedance of $1.6 \text{ M}\Omega/\text{m}$ is found to best match the measurements. Results are plotted in Figure 5.8.

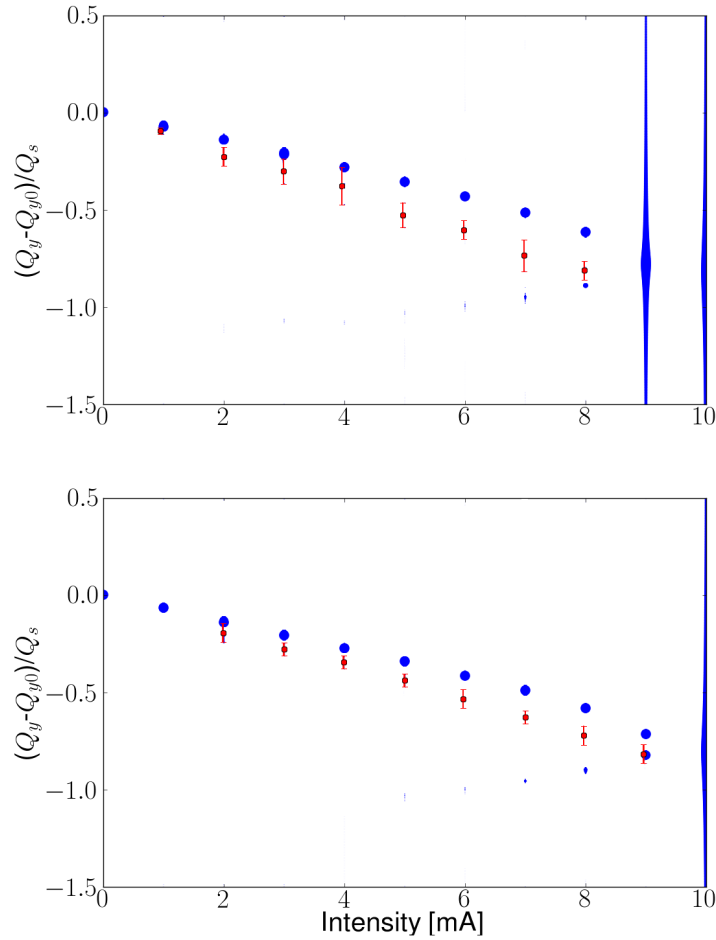


Figure 5.8: Normalized tune shift with HEADTAIL (blue) when a 5th BBR with $f_r=1$ GHz, $Q=1$ and $R_s=1.6 \text{ M}\Omega/\text{m}$ is added in the model. The comparison with measurements (red) is shown. The top plot is for IVUs closed (TMCI from simulation at 9 mA) and the bottom for open (TMCI from simulation at 10 mA).

Modes 0 and -1 are moving and couple at 9 mA, causing a TMCI for closed IVUs (top plot). The measured threshold was 8.8 mA. The slope of the tune shift is still underestimated, suggesting that there might be a missing quadrupolar component of the impedance to be added to the

model. HEADTAIL also predicts successfully the 10 mA threshold for open IVUs (bottom plot). The measured threshold was 9.8 mA.

HEADTAIL predicts the measured TMCI thresholds and explains around 85% of the found mode detuning if a 5th BBR is included in the model, as seen in Figure 5.8. The search for the machine elements candidate to be responsible for the additional impedance is investigated in the next sections.

5.1.2 Study of the injection kickers

Given the experience of other machines, e.g. the Super Proton Synchrotron (SPS) [16], the first suspicion has fallen on the injection kickers, which are still missing from the impedance model. There are four storage ring injection kickers, each one 0.78 m long and with independent power supplies. The kicker magnets' design is based on a C-shaped ferrite yoke which is installed around a ceramic vacuum chamber. The ceramic vacuum chamber is coated with a thin layer of Ti realized with magnetron sputtering [83]. A thickness of $0.4 \mu\text{m}$ was targeted and the kickers were built by Danfysik A/S [84]. The cross section of the injection kicker can be seen in Figure 5.9 [83].

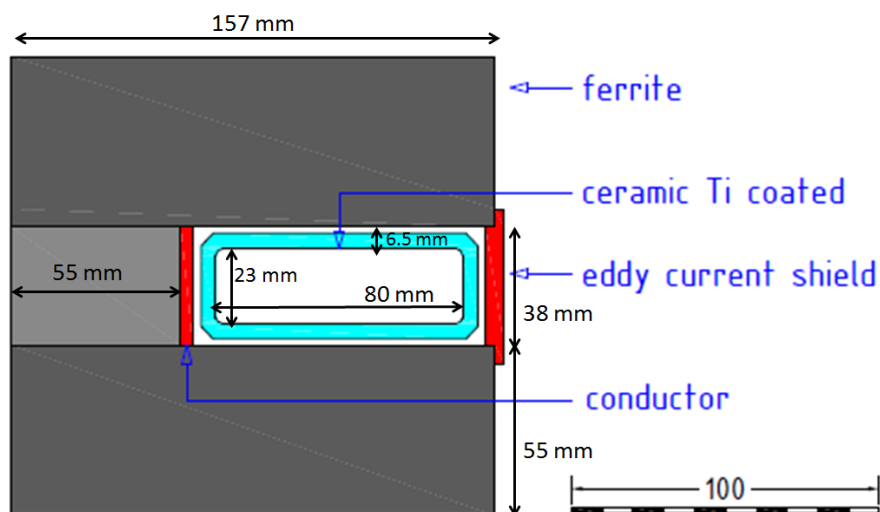


Figure 5.9: Cross section of the injection kicker.

Modeling the injection kickers with CST

In order to model the exact kicker geometry, CST Particle Studio has been used. In Figure 5.10, the 3D model is displayed. In blue is the C-shape Fe yoke of 55 mm thickness, in yellow the rectangular ceramic chamber of 6.5 mm thickness and there is also a thin Ti coating of $0.4 \mu\text{m}$. A 1 mm thick layer of air between chamber and yoke was also considered, required for air cooling.

5.1. Single bunch measurements in the ALBA storage ring

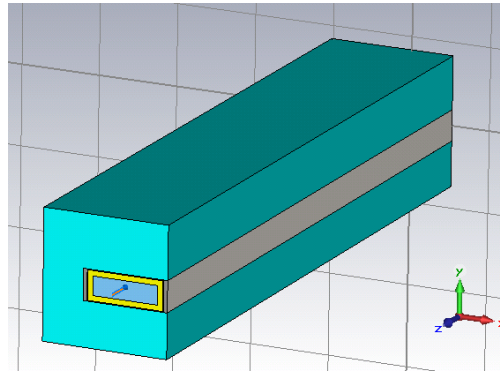


Figure 5.10: 3D model of the injection kicker with CST. In blue is the C-shape Fe yoke of 55 mm thickness, in yellow the rectangular ceramic chamber of 6.5 mm thickness and there is also a thin Ti coating of $0.4 \mu\text{m}$. The height of the ceramic chamber is 23 mm and the width is 80 mm. A 1 mm thick layer of air is also considered.

CST can calculate the wake potential of a given structure for a certain exciting bunch length. In order to approximate the wake potential with the wake function, a delta function excitation [85] is necessary. For use in HEADTAIL simulations, we would need the wake potential associated with an excitation as long as the slice used in the simulation. As the ALBA bunch is about 20 ps long and we use 500 slices in simulations, the structure has to be excited with a bunch 0.04 ps long. Such requirement results in an explosion of the number of mesh-cells to ~ 500 billion (for already a scaled down kicker length of 10 cm) in order to simulate the field structure. Such simulation cannot be realized with the supercomputer available at CERN, nor with the cluster. An alternative approach is to use 2D codes, based on semi-analytical calculations, such as ImpedanceWake2D.

Comparative studies of multilayer structures with CST and ImpedanceWake2D

Based on the above requirement, comparative studies were performed for CST and ImpedanceWake2D. A bench approach is necessary between the codes since CST can simulate the real element's geometry, but is limited by computer power, while ImpedanceWake2D can calculate semi-analytically the resistive wall contribution of a flat/round multilayer structure over an arbitrary frequency range but ignores the C-shape ferrite yoke. Therefore, we first want to show that in the available range of frequency for CST, the results from these two codes agree and then we can simply use the wake from ImpedanceWake2D in our study. A round and a flat multilayer structure are compared with the two codes.

Comparison for a round multilayer structure

The first comparison is done for a round multilayer structure, as shown in Figure 5.11. The radius is 11.5 mm, the ceramic is 6.5 mm thick (yellow) and the Fe is 55 mm thick (blue). The background is PEC and by offsetting the source and test particles by 4 mm in the y plane,

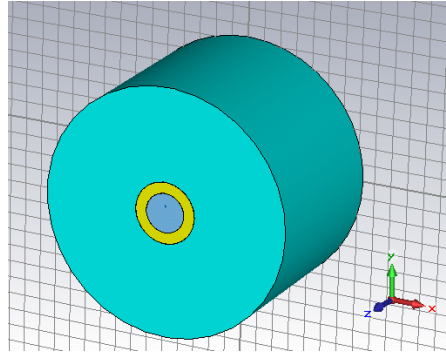


Figure 5.11: CST 3D model of a round multilayer structure with 11.5 mm radius. The inner layer is ceramic of 6.5 mm thickness (yellow) and the outer layer is Fe of 55 mm thickness (blue).

the vertical generalized impedance is calculated. The impedance from the CST computation is compared to the ImpedanceWake2D results, assuming the same structure and material properties. The latter are listed in Table 5.4.

Table 5.4: Material properties in the multilayer round structure, simulated with Impedance-Wake2D.

Layers	σ (S/m)	ϵ'	μ_r	f_{rel} (MHz)	d (mm)
1: Ceramic	1×10^{-12}	9.3	1	Infinity	6.5
2: Fe	1×10^{-4}	12	460	20	Infinity

The comparison of the vertical generalized impedance with CST and ImpedanceWake2D is shown in Figure 5.12. CST and ImpedanceWake2D results agree within 5%.

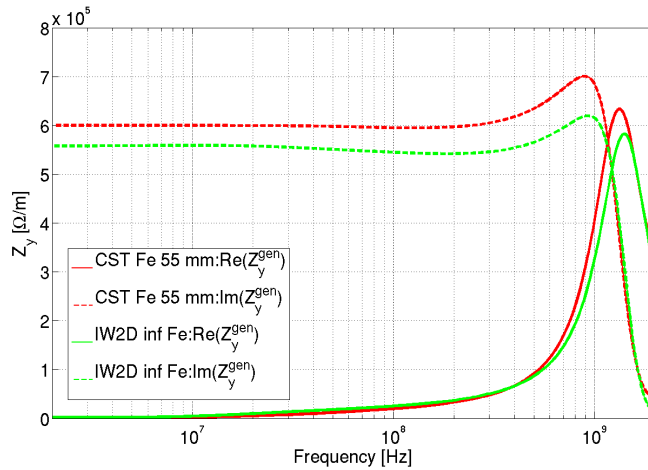


Figure 5.12: Comparison of the generalized impedance of a round multilayer structure with CST (red) and ImpedanceWake2D (green). Agreement within 5% is found.

Comparison for a flat multilayer structure

The second step is to compare a multilayer flat structure. The CST 3D model is shown in Figure 5.13.

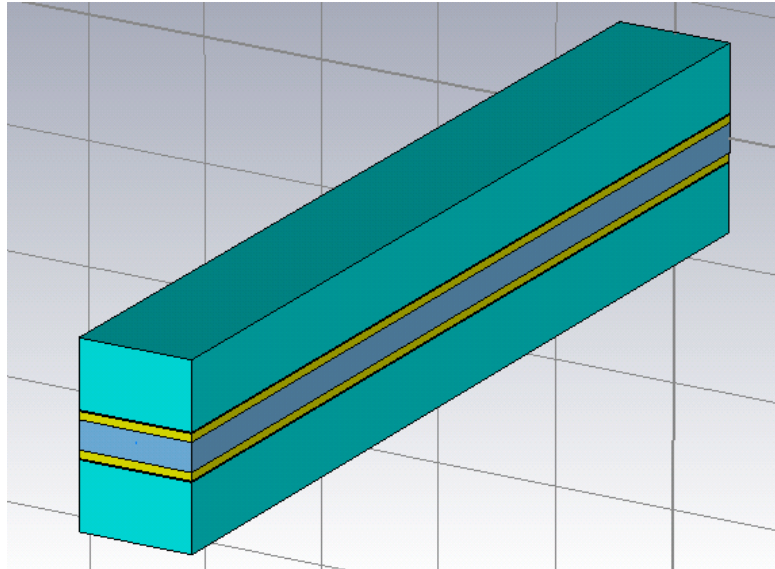


Figure 5.13: CST 3D model of a flat multilayer structure with a gap of 11.5 mm. The inner layer is ceramic of 6.5 mm thickness (yellow), the middle layer is air of 1 mm and the outer layer is Fe of 55 mm thickness (blue).

The half gap is 11.5 mm, the Ti coating is 0.4 μm thick (when considered), the ceramic (yellow) is 6.5 mm thick, 1 mm of air is also accounted and Fe (blue) is 55 mm thick. The background is PEC and the vertical generalized impedance is calculated. The calculated impedance with CST is compared to the ImpedanceWake2D results. The properties of the flat multilayer structure materials are shown in Table 5.5.

Table 5.5: Material properties of the flat multilayer structure with ImpedanceWake2D.

Layers	σ (S/m)	ϵ'	μ_r	f_{rel} (MHz)	d (mm)
1: Ti	2.38×10^6	1	1	Infinity	0.4×10^{-3}
2: Ceramic	1×10^{-12}	9.3	1	Infinity	6.5
3: Air	5×10^{-17}	1	1	Infinity	1
4: Fe	1×10^{-4}	12	460	20	Infinity

The vertical generalized impedance is shown in Figure 5.14. CST and ImpedanceWake2D agree within 5%. Therefore, a good agreement (no coating assumed so far) between the two codes is found for both round and flat structures.

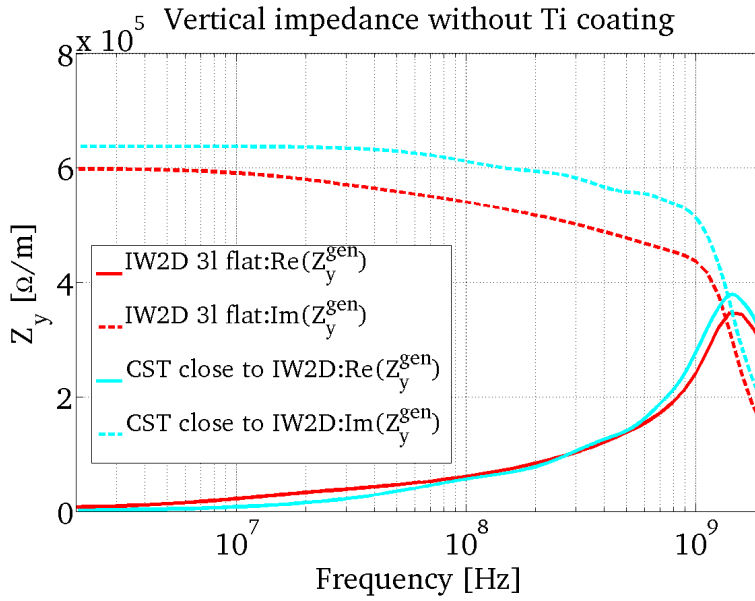


Figure 5.14: Comparison of the generalized impedance for a flat three-layer (3l) structure with CST (cyan) and ImpedanceWake2D (red). CST close to IW2D refers to the structure in Figure 5.13. Good agreement within 5% when no coating is used.

Comparison for a flat multilayer structure with coating

The next step is to compare the two codes in the case where coating is used. There are two different features to apply material coating in CST. One, which is called tabulated surface impedance, is compared with ImpedanceWake2D in Figure 5.15. A disagreement of almost a factor of 2 is observed. The second feature, which has been used in Chapter 4, requires to define the substrate material as lossy metal and apply the coating on top (see Figure 5.16). Differences in the impedance value as well as a frequency shift are observed and the two coating features give different results.

In the particular kicker structure, the lossy-material-coating feature cannot provide trustworthy results since the substrate is actually a ceramic, thus not a lossy metal. A comparison with a lossy metal substrate can be found in Appendix C.1.

Comparison with the real kicker geometry

The real kicker structure, shown in Figure 5.10, is compared in Figure 5.17 with the flat structure from Figure 5.13 (labeled as close to IW2D, since this is the 3D equivalent of what IW2D simulates) and the outcome from IW2D. Although there is disagreement with ImpedanceWake2D due to the tabulated surface impedance feature of CST, the important conclusion is that the real kicker (blue) can be simplified with a flat multilayer structure (cyan) since impedance calculations agree within 5%. Therefore, we feel confident that ImpedanceWake2D can be used for the impedance calculation of the ALBA kicker and the computed wake function

5.1. Single bunch measurements in the ALBA storage ring

for the HEADTAIL simulations.

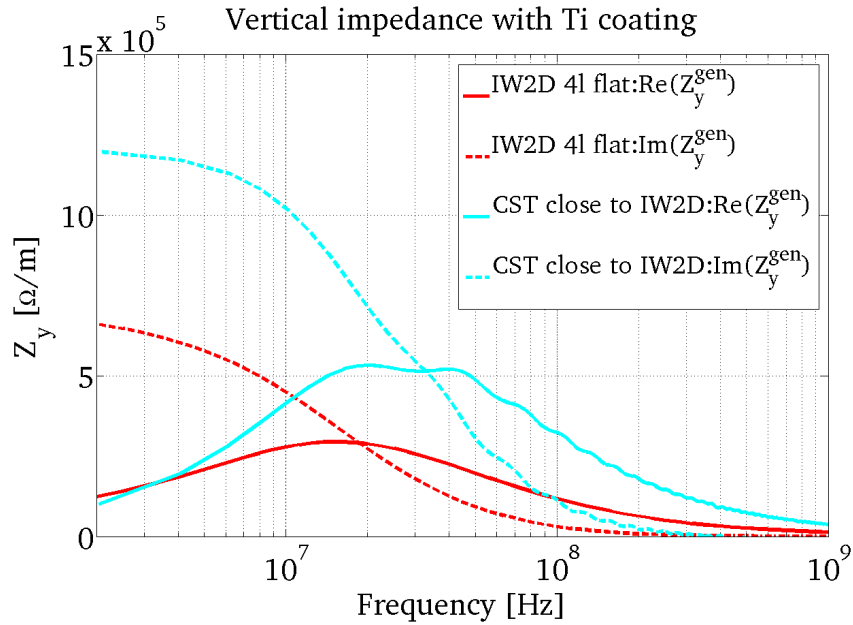


Figure 5.15: Comparison of the generalized impedance for a flat multilayer structure with CST (cyan) using tabulated surface impedance and ImpedanceWake2D (red). Disagreement of almost a factor of 2 is observed when Ti coating is implemented.

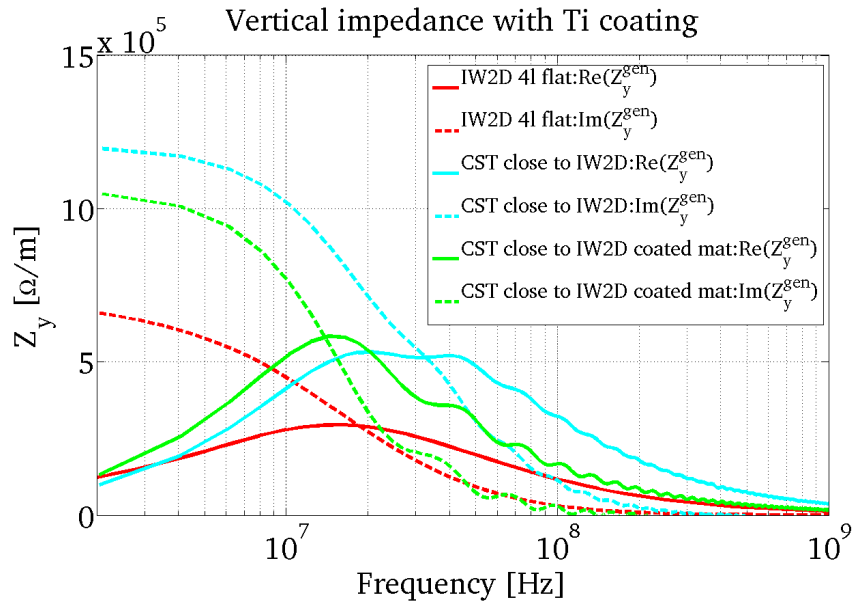


Figure 5.16: Comparison of the generalized impedance for a flat multilayer structure between the tabulated surface impedance with CST (cyan), the lossy metal coating with CST (green) and ImpedanceWake2D (red). The label CST close to IW2D again refers to the CST structure of Figure 5.13.

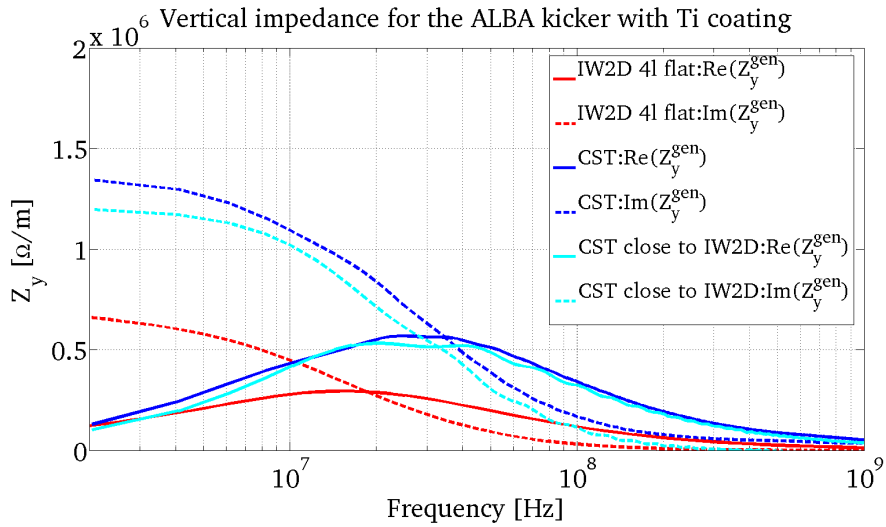


Figure 5.17: Comparison of the generalized impedance for a flat multilayer structure between CST using tabulated surface impedance (cyan), the real kicker geometry using tabulated surface impedance (blue) and ImpedanceWake2D (red).

ALBA kickers impedance simulation

ImpedanceWake2D is used for the semi-analytical calculation of the ALBA kicker's impedance. The simulated generalized vertical impedance for a 4-layer flat structure is shown in Figure 5.18.

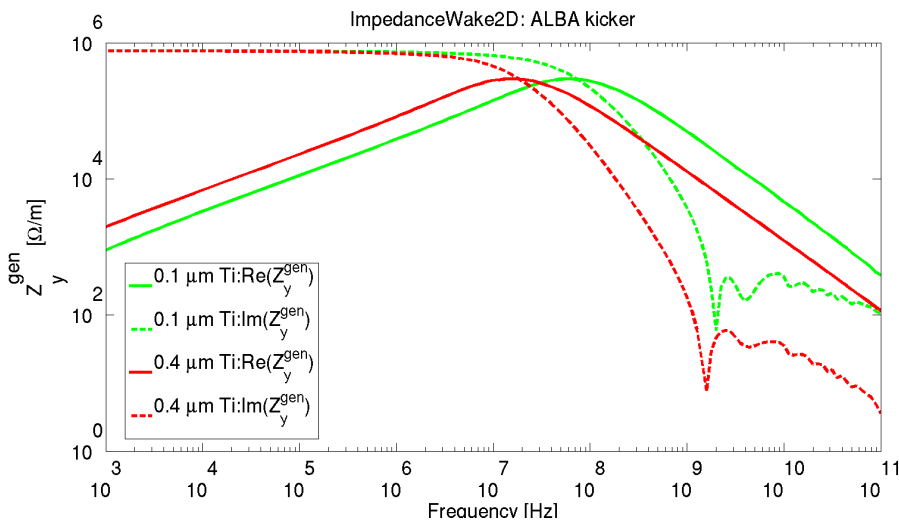


Figure 5.18: Vertical generalized impedance of the ALBA kicker with ImpedanceWake2D. In red, Ti thickness is $0.4 \mu\text{m}$. In green, a thinner coating is considered of $0.1 \mu\text{m}$. The absolute value of the imaginary impedance is displayed.

The material properties were previously listed in Table 5.5. The results presented show the real and the absolute value of the imaginary impedance for 0.1 and $0.4 \mu\text{m}$ Ti coating. From

5.1. Single bunch measurements in the ALBA storage ring

the computed impedance, the effective impedance for a Gaussian bunch can be calculated using Eq.(2.43), as explained in 2.3.3.

For a $0.4 \mu\text{m}$ thick Ti coating, the computed imaginary effective impedance, $\text{Im}(Z_{\text{eff}})$, is between $1.97\text{-}3.2 \text{ k}\Omega/\text{m}$, taking into account the observed bunch lengthening (Figure 5.4). For a $0.1 \mu\text{m}$ thick Ti coating, the $\text{Im}(Z_{\text{eff}})$ is estimated between $9.3\text{-}14 \text{ k}\Omega/\text{m}$. Small deviation from the expected Ti thickness results in an important difference in the effective impedance calculation.

Including the kickers in the impedance model

The above mentioned ImpedanceWake2D results for the kickers are now implemented in the HEADTAIL impedance model to see the effect on the missing impedance. A $0.4 \mu\text{m}$ thick Ti coating is considered. The comparison between the model with and without the kickers, along with the measured tune shift, is shown in Figure 5.19.

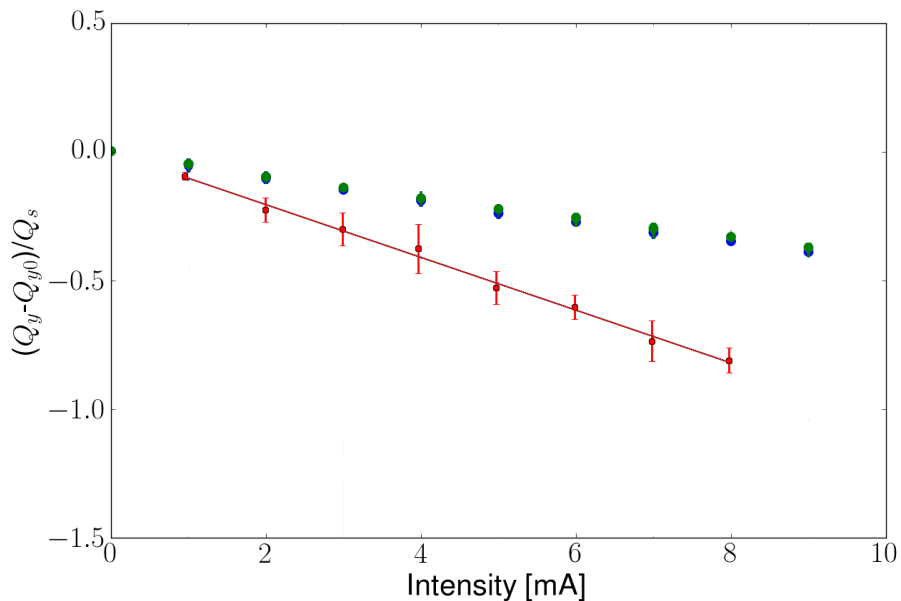


Figure 5.19: Normalized tune shift as predicted with HEADTAIL simulation (green) based on the current impedance model, for HEADTAIL when the 4 injection kickers are included (blue) and as measured (red). The IVUs are closed.

We can observe that the effect of the kickers' impedance in the simulated tune shift is almost negligible, assuming a nominal Ti thickness. An improved model including also the transitions will be required to compare it to measurements.

5.1.3 TMCI measurements at 0 chromaticity to study the effect of the pinger magnet

During the summer of 2014, a new pinger magnet was installed in ALBA, in sector 7. Pictures from the pinger magnet are shown in Figure 5.20.

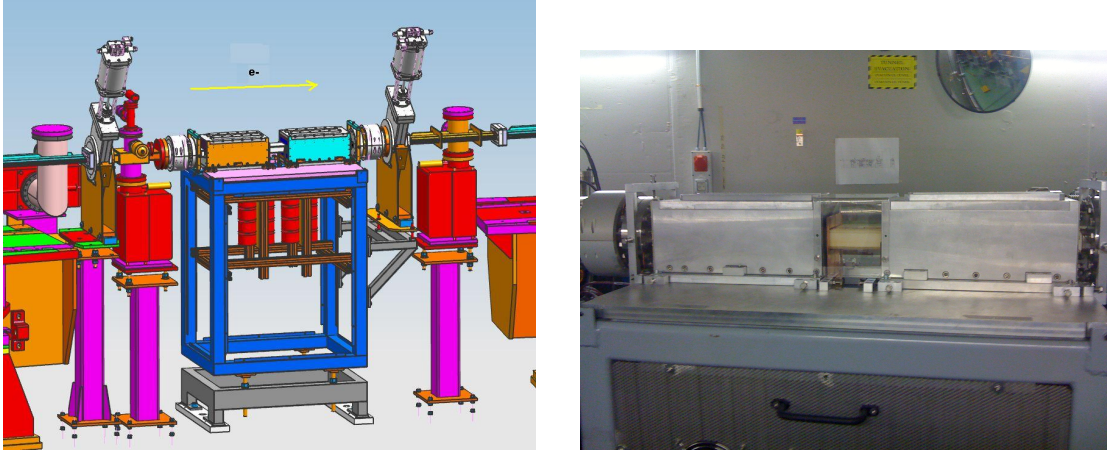


Figure 5.20: Pinger magnet installed in ALBA. The geometry is exactly the same as the injection kickers described in 5.1.2.

The pinger magnet will be powered with a pulse of around $1 \mu\text{s}$ long and will be used to kick the beams far away from the linear region in the magnets. Its purpose is to study the nonlinear characteristics of the machine. The mechanical shape is identical to the injection kickers, but with different electronics.

The suggested measurements for the second MD include single bunch measurements with increasing bunch current. The same conditions were used as in the first MD. The goal is to compare measurements before and after the pinger magnet's installation and therefore extract a direct beam-based impedance measurement of this device. Setting chromaticity to zero and RF voltage to 2.1 MV, the single bunch current was gradually increased till a TMCI occurs at 8.4 mA (8.8 mA was the threshold before the pinger's installation for closed IVUs). A difference of $(4.6 \pm 1)\%$ is observed in the TMCI thresholds, with a lower threshold after the pinger's installation.

The tune shift as a function of single bunch current is plotted in Figure 5.21 before and after the pinger's installation in the ALBA tunnel. The comparison is illustrated in Figure 5.22 after normalizing the tune shift to the synchrotron tune. The slope became steeper by 4.4% after the pinger's installation.

For a Gaussian beam, the complex mode frequency shift is given by Eq.(2.45). The imaginary part of the effective impedance is estimated from the measured tune shift as

$$\text{Im}(Z_{\text{eff}}) = \frac{dQ}{dI_b} 4\sqrt{\pi}(E/e)\omega_0\sigma_z \frac{1}{\langle \beta \rangle}, \quad (5.3)$$

5.1. Single bunch measurements in the ALBA storage ring

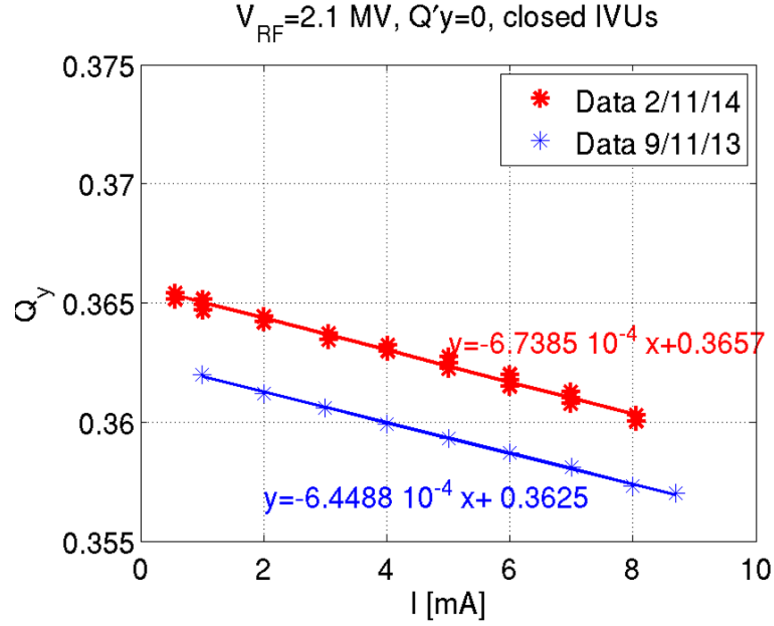


Figure 5.21: Comparison of the vertical tune shift as a function of single bunch intensity before (blue) and after (red) the pinger magnet's installation.

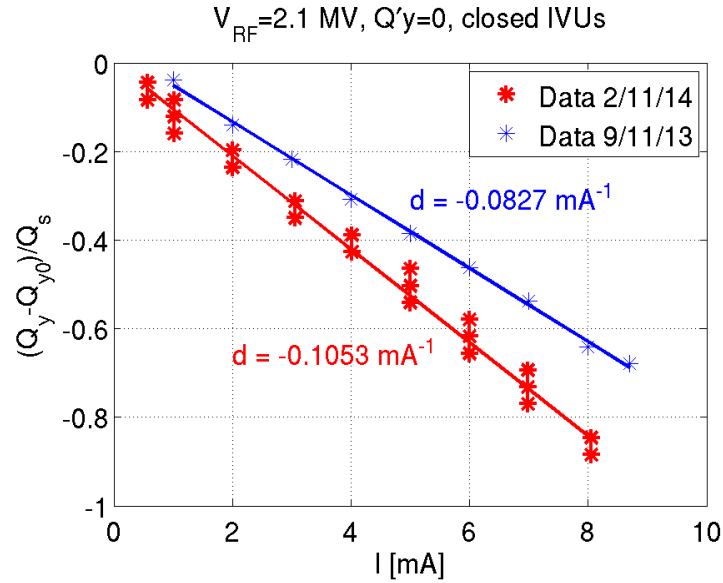


Figure 5.22: Comparison of the normalized vertical tune shift as a function of single bunch intensity before (blue) and after (red) the pinger magnet's installation.

where I_b is the bunch current. Using Eq.(5.3), the imaginary effective impedance is estimated from the measured tune shift as $\text{Im}(Z_{\text{eff}}) = 216$ k Ω /m before the pinger magnet's installation. After installation, the $\text{Im}(Z_{\text{eff}})$ is increased to 224 k Ω /m. The pinger impedance is obtained from the difference between the two values, normalized by the ratio of $\langle \beta \rangle / \beta_p$, where β_p is the beta-function at the pinger. It is calculated that $\text{Im}(Z_{\text{eff}}^{\text{pinger}}) \approx 15$ k Ω /m.

Chapter 5. Studies on existing and future light sources

The computed pinger magnet impedance has $\text{Im}(Z_{\text{eff}})$ of maximum 3.2 k Ω /m for a 0.4 μm Ti thickness. According to resistance measurements in the four injection kickers and the pinger magnet (coated during the same process), the Ti thickness varies between 0.36 and 0.402 μm [83]. The surface roughness and inhomogeneity of the coating are not taken into account. Despite the fact that the effective impedance calculation is quite sensitive to the Ti thickness assumed, measurements indicate that the thickness is very close to the targeted 400 nm. Therefore, the measured effect of the pinger impedance seems to exceed by about a factor of 4-5 the model expectations.

5.2 Impedance studies for the SLS2 upgrade

The Swiss Light Source (SLS) at the Paul Scherrer Institut (PSI) is a third-generation synchrotron light source with energy of 2.4 GeV and 288 m circumference. It provides high brightness photon beams to 18 beam lines for research in materials science, biology and chemistry. A panoramic view is shown in Figure 5.23. SLS was commissioned in 2000 and has been successfully providing $5.5 \text{ nm} \times 5 \text{ pm}$ emittance beams at 400 mA.



Figure 5.23: SLS light synchrotron at PSI.

5.2.1 Motivation

In order to stay competitive with other state-of-the-art machines, an upgrade project, named SLS2, is being discussed targeting at a lower emittance design. The existing building, injector and beam lines will be maintained. Lattices considered have a very low and even negative momentum compaction factor and narrow NEG-coated pipes are foreseen. Collective effects are of great concern due to the narrow beam pipe, the high beam brightness and the small emittances. First studies focus on the transverse plane and the concept lattice with very low and negative momentum compaction factor. The machine and beam parameters are listed in Table 5.6.

Table 5.6: SLS2 parameters for the concept lattice.

Energy [GeV]	2.4
Trans. emitt.(x,y)[pm]	73, 5
Bunch length [mm]	7.4
Momentum spread	0.0011
Bunch population	3.1×10^{10}
Circumference [m]	288
Mom. compact. factor	-5.4×10^{-5}
Tunes (x,y,s)	39.4, 13.17, 0.00037
Average beta (x,y) [m]	6.65, 6.13
Damping times (x,y)[ms]	5.6, 7.5
RF frequency [MHz]	100
RF voltage [MV]	0.7
Harmonic number	96

5.2.2 Transverse resistive wall impedance and instability thresholds at zero chromaticity

The resistive wall is one of the main sources of impedance in synchrotrons and storage rings with very small beam chambers. The first step in analyzing the impedance budget of a future accelerator is to ensure that the nominal intensity is stable under the effect of the resistive wall impedance (which cannot be avoided) and there is still sufficient margin to accommodate the further impedance contributions that will come from the other accelerator devices. Hence, instabilities due to resistive wall should be studied for the nominal parameters.

A round Cu vacuum chamber with 10 mm radius is considered, along with a uniform NEG coating of 1 μm thickness. In order to calculate the resistive wall wake function, required in HEADTAIL simulations, ImpedanceWake2D is used. A 2-layer round structure is considered, with an inner layer of NEG and an infinite layer of Cu. The input parameters are listed in Appendix D.1.

Once the wake function of the RW is calculated, it is inserted in HEADTAIL for the macro-particles simulation at zero chromaticity. The y centroid output as a function of time for various bunch populations is shown in Figure 5.24.

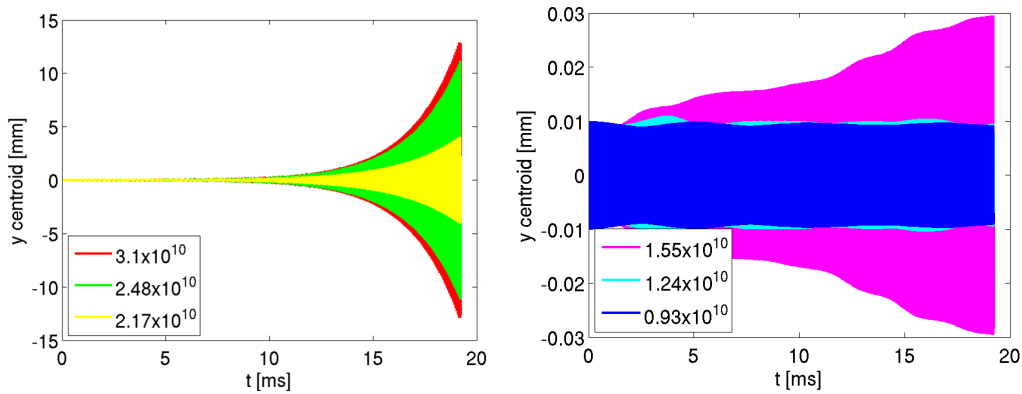


Figure 5.24: Y centroid position as a function of time for various bunch populations in the presence of resistive wall impedance. The nominal bunch population for the concept lattice is 3.1×10^{10} .

These simulations reveal that at least a 2.5 times lower bunch population (1.24×10^{10}) is required for stable operation. In reality, this factor will be much lower due to the presence of other impedance contributors coming from the various machine elements that will be installed. The scenario of using a third harmonic RF cavity (3HC), in order to increase the bunch length, reduce intrabeam scattering and improve Touschek lifetime, was also simulated. The bunch length now is almost 3 times larger than the one without a 3HC, i.e. $\sigma_z=22.2$ mm. The synchrotron tune is recalculated according to the matching condition in Eq.(5.2), as $Q_s=0.00012$, while the momentum spread is assumed constant. The results of HEADTAIL simulations in the presence of a 3HC for various bunch populations are shown in Figure 5.25. The centroid is unstable for the nominal beam intensity and actually the presence of a 3HC

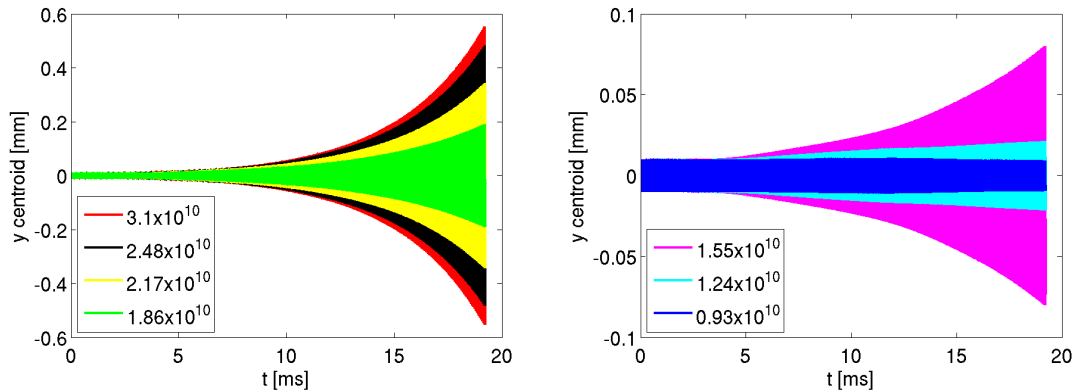


Figure 5.25: Y centroid position as a function of time for various bunch populations for resistive wall impedance with a 3HC. The nominal bunch population for the concept lattice is 3.1×10^{10} .

worsens the instability since the synchrotron tune is even lower. A bunch population of 0.93×10^{10} is required for stable operation.

The above simulations reveal that operation with zero chromaticity is not an option for the particular lattice design. For nominal intensity and only RW, the beam is already unstable due to TMCI. A much lower intensity would allow operation at zero chromaticity, but this would defeat the purpose of achieving higher beam brightness.

5.2.3 Transverse resistive wall impedance and instability thresholds at positive and negative chromaticity

Since operation at zero chromaticity is strongly limited by resistive wall alone, the options of positive or negative chromaticity are investigated.

Positive chromaticity

Various positive chromaticity values are simulated with HEADTAIL for the designed bunch intensity and the y centroid position is shown in Figure 5.26. The increase of chromaticity leads to a faster instability. For non zero chromaticity, when the TMCI instability moves to higher thresholds and head-tail instability occurs, it is necessary to compare the rise time of the instability to the damping time.

For this purpose, the rise time is calculated for each chromaticity by fitting an exponential $y(t) = y_0 e^{t/\tau}$ to the centroid amplitude. The rise time, τ in s, is calculated and compared to the 7.5 ms damping time (Table 5.6). The rise times are gathered in Table 5.7 for various positive chromaticities. Indeed, from Table 5.7, it is observed that the higher the chromaticity, the faster the instability becomes.

The important conclusion is that for all simulated chromaticity values, the rise time is always smaller than 7.5 ms. Hence, the instability is faster than the natural damping mechanism. This

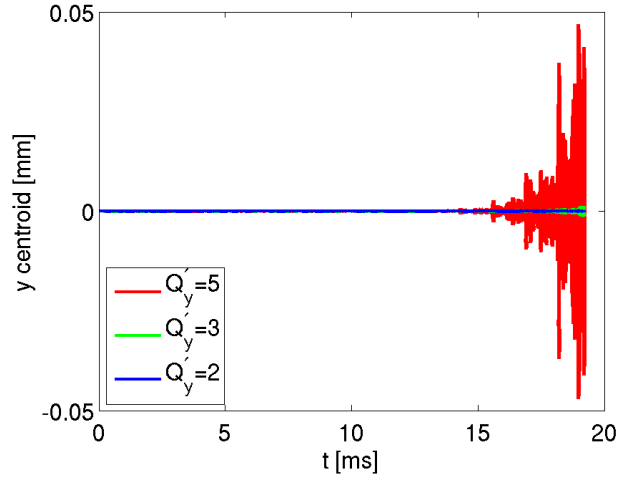


Figure 5.26: Y centroid position as a function of time for various positive chromaticities $Q'_y = 2, 3, 5$.

Table 5.7: Rise time for various positive chromaticities.

Chromaticity Q'_y	Rise time (ms)
1	1.9
2	1.6
3	1.2
5	1

outcome was expected due to the fact that the lattice considered has a negative momentum compaction factor. In this case, single bunch head-tail instability at mode 0 takes place at positive chromaticities [86].

Negative chromaticity

Zero chromaticity operation was excluded due to TMCI and positive chromaticity, as well, due to mode 0 head-tail instability. The negative chromaticity scenario is now examined, for which we expect higher order head-tail modes to be unstable. The simulated y centroid for several negative chromaticities $Q'_y = -0.5, -0.6, -0.7, -0.8, -1, -1.5$ and nominal bunch current is illustrated in Figure 5.27.

After kicking the beam in the vertical plane, the envelope of the betatron oscillation is strongly modulated by the synchrotron frequency. The phenomenon of decoherence and recoherence of the beam oscillation is a combined effect of machine chromaticity and synchrotron motion. Such a phenomenon has been observed in many accelerators and storage rings [87, 88].

Similar to positive chromaticity, the comparison of the rise time to the damping time is required to understand if the beam is stable. When chromaticity is positive, $m = 0$ mode gets unstable, while for negative chromaticity, $m = 0$ is damped and higher modes get unstable.

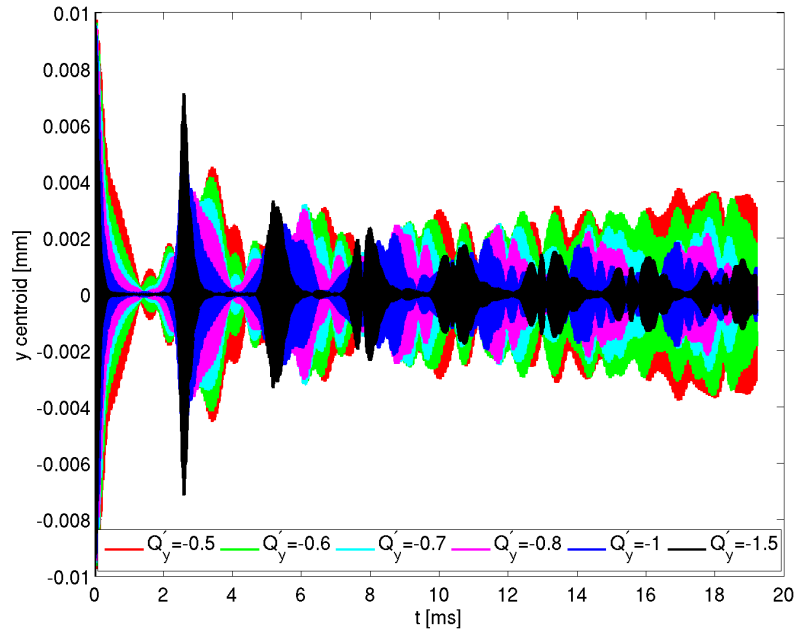


Figure 5.27: Y centroid position as a function of time for various negative chromaticities $Q'_y = -0.5, -0.6, -0.7, -0.8, -1, -1.5$.

Negative momentum compaction factor resembles operation below transition. The rise time was calculated for some chromaticities and results are gathered in Table 5.8.

Table 5.8: Rise time for various negative chromaticities.

Chromaticity Q'_y	Rise time (ms)
-0.5	13.6
-0.6	18.5

As theoretically expected, the beam is stable for nominal intensity and negative machine chromaticity. As shown in Table 5.8, the rise time of the instabilities is larger than 7.5 ms and is increasing for higher negative values. Therefore, the instability is slower than the natural damping and the beam is stable for nominal beam parameters.

Negative chromaticity with resistive wall and broad-band impedance

The previous analysis indicated that operation with negative chromaticity is required for the beam stability. The next question to be addressed is how much is the available transverse impedance budget. To answer this question, the impedance model used in simulations should be enriched with other contributions apart from the resistive wall. As a second step, a broad-band resonator is added to the model.

In order to calculate the frequency of the resonator, equations for a circular waveguide were

used. The cutoff frequency for a particular TE or TM mode in circular waveguide is determined by the following relation

$$\lambda = \frac{2\pi r}{\rho_{mn}} \quad (5.4)$$

$$f = \frac{c}{\lambda}, \quad (5.5)$$

where r is the waveguide radius, $\rho_{mn}=\rho_{10}=1.841$ for the lowest TE mode and $\rho_{mn}=\rho_{00}=2.405$ for the lowest TM mode. The cutoff frequency is calculated at 8.8 GHz for TE₁₀ and 11.5 GHz for TM₀₀. Hence, the chosen frequency of the broad-band resonator is 8 GHz and the quality factor is 1.

The transverse shunt impedance R_s is the parameter scanned in HEADTAIL simulations. Negative chromaticity is chosen, $Q'_y=-1$, in order to investigate the remaining budget when the impedance model consists of a resistive wall and a broad-band contribution. The result is shown in Figure 5.28.

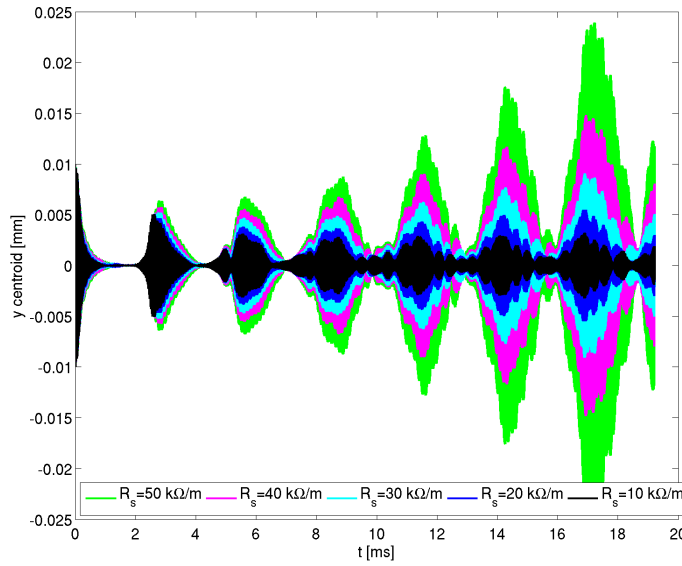


Figure 5.28: Y centroid position as a function of time for various R_s values and $Q'_y=-1$.

By comparing the instabilities' rise time to the damping time, it is concluded that the remaining budget cannot exceed 40 kΩ/m if $Q'_y=-1$. For an electron machine, the transverse impedance is usually few hundreds of kΩ/m. For this reason, the impedance budget was fixed at 500 kΩ/m and chromaticity was scanned. The simulation results are shown in Table 5.9.

By comparing the rise times from Table 5.9 to the 7.5 ms damping time, it becomes evident that only higher negative chromaticity than -6 can allow 500 kΩ/m. For such high chromaticity, dynamic aperture studies will be required.

Table 5.9: Rise time for various negative chromaticities and $R_s=500$ k Ω /m.

Q'_y	Rise time (ms)
-5	5.96
-6	7.67
-7	8

Concept lattice for 500 MHz RF frequency

An alternative scenario is considered for the RF cavity operation at 500 MHz. The machine and beam parameters are listed in Table 5.10.

Table 5.10: SLS2 parameters for the concept lattice at 500 MHz.

Energy [GeV]	2.4
Trans. emitt.(x,y)[pm]	66, 7
Bunch length [mm]	2.36
Momentum spread	0.0011
Bunch population	5×10^9
Circumference [m]	288
Mom. compact. factor	-5.4×10^{-5}
Tunes (x,y,s)	39.4, 13.17, 0.00117
Average beta (x,y) [m]	6.65, 6.13
Damping times (x,y)[ms]	5.6, 7.5
RF frequency [MHz]	500
RF voltage [MV]	1.01
Harmonic number	480

For the transverse resistive wall model and 0 chromaticity, the bunch centroid in the vertical plane is plotted in Figure 5.29. We can observe that the centroid is stable with the nominal bunch population of 5×10^9 .

The centroid however gets unstable if a BBR is added to the model with $R_s=500$ k Ω /m (only up to 300 k Ω /m give stable results). The simulations with a 3HC cavity with rms bunch length of 7 mm and synchrotron tune of 3.8×10^{-4} , gave similar results of a stable centroid under the effect of resistive wall impedance (see Figure 5.30) but unstable if the BBR is added (only up to 50 k Ω /m give stable results).

Although the 500 MHz option gives stable results under the effect of resistive wall impedance (as opposed to the 100 MHz), negative chromaticity operation still has to be considered in order to be able to accommodate a sufficient impedance budget. Fixing $R_s=500$ k Ω /m, the chromaticity is scanned in order to find the value for which the centroid will be stable. Simulation results are shown in Table 5.11. By comparing the computed rise times to the 7.5 ms vertical damping time, we can see that a higher negative chromaticity than -3 is necessary to allow 500 k Ω /m.

Therefore, for the concept lattice, it is required to operate with negative chromaticity, since only then a sufficient impedance budget can be accommodated. Between the 100 and 500

MHz RF frequencies, the 500 MHz option is preferred since it requires a less high chromaticity.

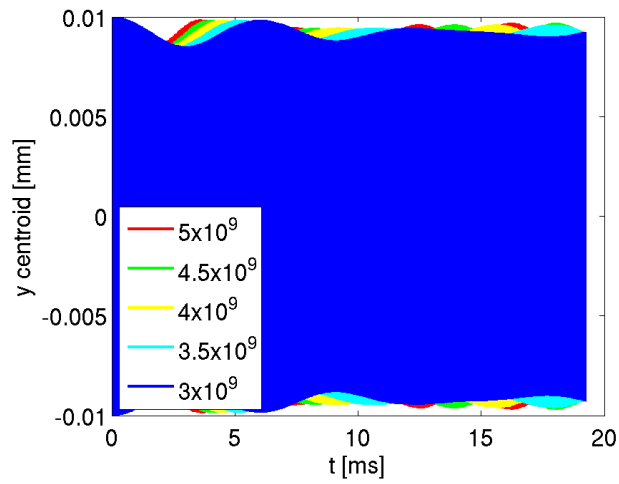


Figure 5.29: Y centroid position as a function of time for various bunch populations and 0 chromaticity under the effect of resistive wall impedance.

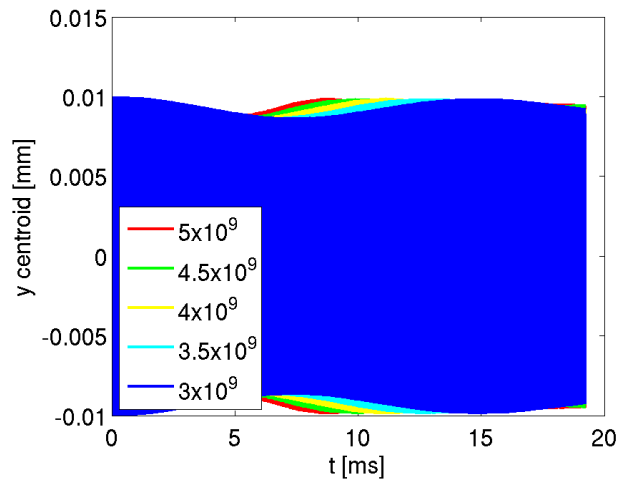


Figure 5.30: Y centroid position as a function of time for various bunch populations and 0 chromaticity under the effect of resistive wall impedance using a 3HC.

Table 5.11: Rise time for various negative chromaticities and $R_s=500$ k Ω /m for 500 MHz.

Q'_y	Rise time (ms)
-2	6.49
-3	8.87

5.2.4 Comparative study with higher negative momentum compaction factor lattice (ca05q)

Several lattices are considered for the SLS2 upgrade. The one presented in 5.2.1 is the most aggressive in terms of emittance reduction. Another lattice that is under study has a higher negative momentum compaction factor, $\alpha_p = -9.6 \times 10^{-5}$. A comparative study follows to demonstrate the performance of the lattice. The machine and beam parameters are listed in Table 5.12.

Table 5.12: SLS2 parameters for the ca05q lattice.

Energy [GeV]	2.4
Trans. emitt.(x,y)[pm]	114, 12
Bunch length [mm]	10.1
Momentum spread	0.00124
Bunch population	2.5×10^{10}
Circumference [m]	288
Mom. compact. factor	-9.6×10^{-5}
Tunes (x,y,s)	37.28, 9.12, 0.00054
Average beta (x,y) [m]	1.23, 5.03
Damping times (x,y)[ms]	4.45, 6.26
RF frequency [MHz]	100
RF voltage [MV]	0.88
Harmonic number	96

5.2.5 Transverse resistive wall impedance and instability thresholds at zero chromaticity for the ca05q lattice

A round Cu vacuum chamber of 10 mm radius is considered with a uniform NEG coating of 1 μm , similarly to 5.2.2. The y centroid output for 0 chromaticity, as a function of time for various bunch populations, is shown in Figure 5.31.

According to Figure 5.31, the vertical position is stable at lower intensities, as well as the nominal one of 2.5×10^{10} particles per bunch. From this result, the ca05q lattice performs better compared to the concept lattice, where at most a 2.5 lower current is required for stability. As a next step, the available impedance budget should be calculated.

Zero chromaticity with resistive wall and broad-band impedance

A broad-band impedance is added to the current model with $f_r=8$ GHz, $Q=1$ and R_s is scanned. The bunch is stable with nominal bunch intensity for a budget of around 10-20 k Ω /m. Thus, operation at zero chromaticity, is not an option since it cannot accommodate a satisfactory impedance budget.

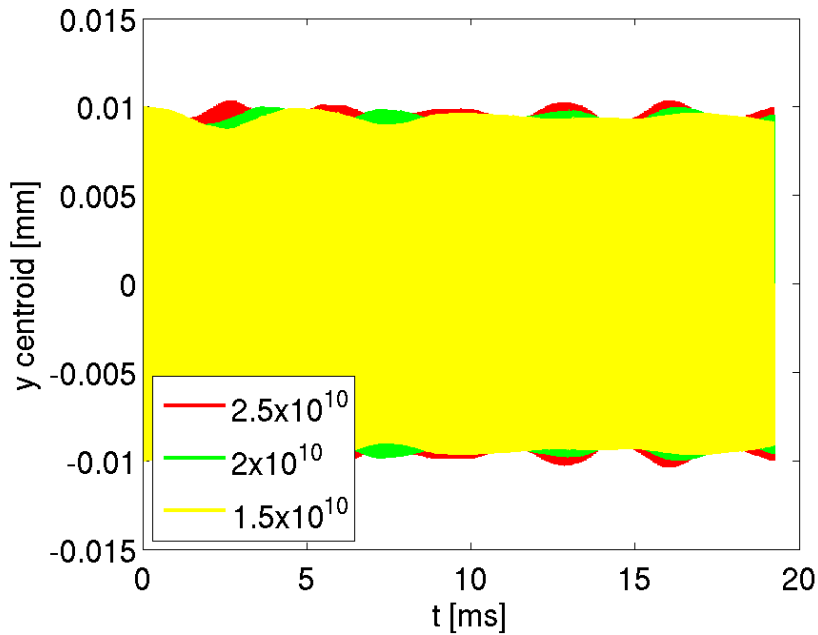


Figure 5.31: Y centroid for various bunch populations at zero chromaticity (only resistive wall impedance). Nominal bunch population is 2.5×10^{10} .

Negative chromaticity with resistive wall

Zero chromaticity operation was excluded due to TMCI, therefore, negative chromaticity simulations are now performed. The y centroid for several negative chromaticities $Q'_y = -0.5, -1, -1.5$ and for nominal bunch current is shown in Figure 5.32. As seen in Figure 5.32, the oscillation is not growing but damping, therefore negative chromaticity results to stable beam since instability is slower than the natural damping.

Negative chromaticity with resistive wall and broad-band impedance model

The following step is to enrich the impedance model with a BBR. The cutoff frequency is 8.8 GHz, the quality factor is 1 and 500 k Ω /m shunt impedance is considered. Simulations with HEADTAIL were done in order to study the beam stability with this impedance model. Chromaticity was scanned and the results are shown in Table 5.13.

Table 5.13: Rise time for various negative chromaticities and $R_s=500$ k Ω /m.

Q'_y	Rise time (ms)
-2	2.4
-3	3.5
-4	6.65
-5	6.7

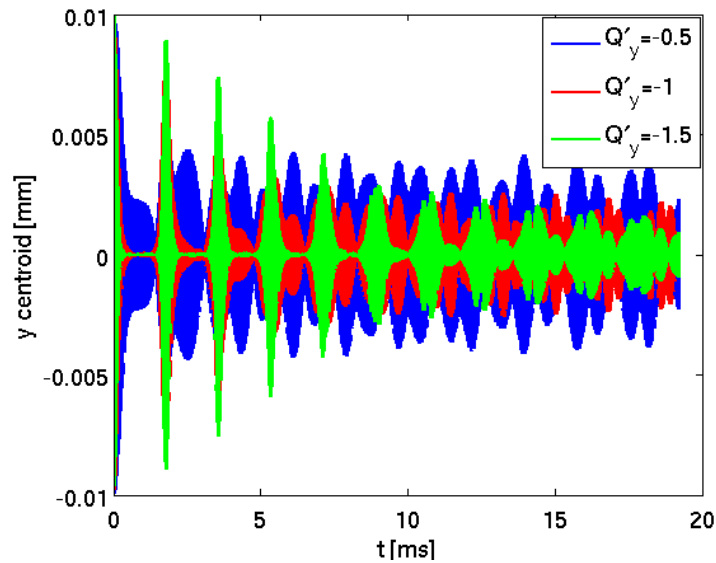


Figure 5.32: Y centroid position as a function of time for various negative chromaticities $Q'_y = -0.5, -1, -1.5$ for the ca05q lattice.

Comparing the rise time to the 6.26 ms damping time, it is concluded that only higher negative chromaticity than -4 can allow a budget of 500 k Ω /m.

ca05q lattice with 500 MHz RF frequency

The performance of the ca05q lattice with 100 MHz is compared to the one with the alternative RF option of 500 MHz. The machine and beam parameters are listed in Table 5.14.

Table 5.14: SLS2 parameters for the ca05q lattice at 500 MHz.

Energy [GeV]	2.4
Trans. emitt.(x,y)[pm]	114, 12
Bunch length [mm]	3.21
Momentum spread	0.00124
Bunch population	5×10^9
Circumference [m]	288
Mom. compact. factor	-9.6×10^{-5}
Tunes (x,y,s)	37.28, 9.12, 0.0017
Average beta (x,y) [m]	1.23, 5.03
Damping times (x,y)[ms]	4.45, 6.26
RF frequency [MHz]	100
RF voltage [MV]	1.2
Harmonic number	480

The results from HEADTAIL are presented in Figure 5.33 for 0 chromaticity and resistive wall

impedance model. The bunch centroid is stable for the nominal population of 5×10^9 .

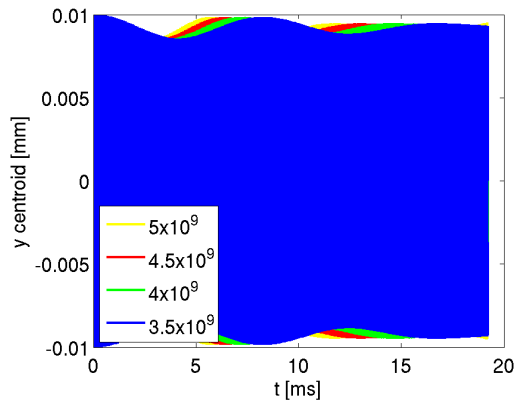


Figure 5.33: Y centroid position as a function of time for the ca05q lattice with 0 chromaticity and 500 MHz.

The impedance model is then enriched by adding a BBR with $f_r=8$ GHz, $Q=1$ and $R_s=500$ k Ω /m. The results are illustrated in Figure 5.34, where we can see that the centroid is stable. This lattice at 500 MHz is the first case where 0 chromaticity operation can be considered since the centroid is stable with $R_s=500$ k Ω /m.

If a 3HC is considered, then the tolerable budget is estimated at ~ 450 k Ω /m. Alternatively, also a negative chromaticity of -3 can result in a stable beam if R_s is assumed to be 500 k Ω /m. From the comparative study, it seems that the ca05q lattice performs better in terms of single bunch thresholds and the 500 MHz frequency can allow operation with zero chromaticity.

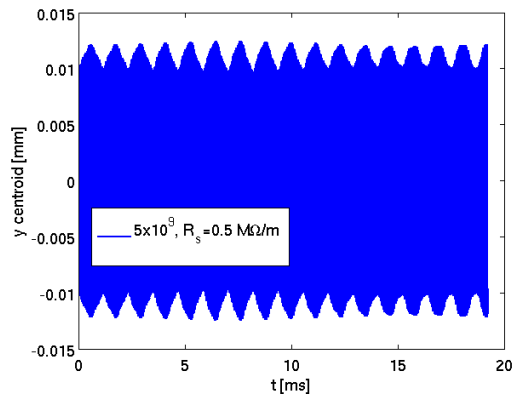


Figure 5.34: Y centroid position as a function of time for the ca05q lattice with 0 chromaticity and 500 MHz. The impedance model consists of the RW and a BBR with $R_s=500$ k Ω /m.

Conclusions

This thesis aimed to study the effect of coatings on beam coupling impedance, with emphasis at high frequencies.

The first new results concern the estimation of the transverse impedance budget of the CLIC DRs. The full ring is modeled with a total impedance made of a broad-band resonator and resistive wall. Operation at zero chromaticity will be preferred since it allows a larger vertical budget of 4 M Ω /m. If the chromaticity cannot be corrected very close to zero and is slightly positive, the budget is reduced to 1 M Ω /m. The design of the devices to be installed in the ring, such as the stripline kickers, has to be such as to stay within the allocated total impedance budget. A computational limitation of 3D codes was encountered for complex structures that require a very small excitation to determine short range wakes, necessary in the regime of the CLIC DRs. The calculation of the wake function with CST Particle Studio requires billions of mesh-cells, which prevents the realization of the simulation even with a cluster. First results of these simulations have been reported here, but further work is required on this subject.

The effect of different coatings was studied, concentrating on the two main candidates for the DRs: NEG and aC. Simulations with ImpedanceWake2D revealed that the coating is transparent up to 10 GHz but seems to have an effect at higher frequencies. It was also demonstrated that making the aC layer as thin as possible would optimize the resistive wall impedance for the DRs. Simulations also indicated that the characterization of material properties at high frequencies is very important since that can affect the correct estimation of the contribution of coatings to the impedance.

A new experimental method was proposed for the characterization of NEG properties at high frequencies. Material properties in this regime were formerly completely unexplored. The method is based on the use of rectangular waveguides made of known materials (stainless steel and copper) and was first benchmarked in X-band. The NEG conductivity was extracted from measurements and CST simulations between 10 and 11 GHz. The value found was $\sigma_{\text{NEG}} = (1 \pm 0.2) \times 10^6$ S/m, which is in good agreement with the measured DC value. The same method was then applied for frequencies above 200 GHz, and up to 750 GHz, for the first time. The extracted conductivity is about 20% lower compared to the DC value (between 0.5 and 0.7×10^6 S/m from resistance measurements), which can be explained partially by the effect of roughness, the non-uniformity of the profile and the measurement accuracy itself. The appearing conductivity drop, as frequency increases, is attributed to the incapability of the simulation to consider the real 3D profile of the coating, resulting in a systematic error during

the intersection. This was verified with a CST simulation using different thickness values of NEG, in order to mimic the non-uniformity of the coating. The extracted conductivity is around 0.35×10^6 S/m from 220 up to 330 GHz with a 15% error, while no dependency is observed with frequency. For frequencies between 500 and 750 GHz, the extracted conductivity is around 0.2×10^6 S/m, which still lies within the accuracy limit of the method. As NEG properties were characterized for the first time at such high frequencies, an important conclusion is that the effective NEG conductivity, to be considered in beam dynamics simulations, can be significantly lower than the DC conductivity, especially at high frequencies (hundreds of GHz), even if relaxation effects are still not important in this frequency range.

The simulation tools applied so far in the CLIC DRs, were used for benchmarking beam measurements realized in the ALBA light source. Single bunch measurements with increasing bunch current provided information on the TMCI thresholds. The developed transverse impedance model can explain around 40% of the measured coherent tune shift and TMCI threshold, and a missing impedance of 1.6 M Ω /m is predicted from HEADTAIL simulations. The current effective impedance of ALBA was also estimated around 224 k Ω /m. The first efforts to find the missing impedance were concentrated on the injection kickers. The effect of the pinger magnet was estimated by repeating the single bunch measurements after its installation. An additional impedance of 15 k Ω /m was found, while more impedance sources have to be found in order to complete the impedance model.

The simulation tools were also applied to study transverse impedance effects for the SLS upgrade, for which a small beam chamber with NEG coating is being considered. In order to achieve the desired emittance reduction, lattices with negative momentum compaction factor are considered. Two lattices with negative momentum compaction factor have been studied in terms of transverse single bunch instabilities and for two different RF frequencies, 100 and 500 MHz. For both lattices, zero chromaticity operation does not allow a sufficient impedance budget if the RF frequency is 100 MHz. For the prototype lattice, the threshold is 2.5 times lower than the nominal bunch population, under the effect of resistive wall only. However, negative chromaticity operation can be considered. For the prototype lattice, $Q'_y = -6$ is required for 500 k Ω /m impedance to be accommodated and $Q'_y = -3$ for the ca05q lattice at 100 MHz. From the comparative study, it seems that the ca05q lattice performs better in terms of single bunch thresholds and an RF frequency of 500 MHz is preferable due to the lower negative chromaticity required for beam stability. Moreover, if a frequency of 500 MHz is chosen, then operation with zero chromaticity can be considered for the ca05q lattice, since it permits beam stability and a sufficient impedance budget.

A HEADTAIL simulations parameters for the CLIC DR

A.1 Broad-band resonator model with 0 chromaticity

CLIC DR parameters used in HEADTAIL simulations for a BBR and 0 chromaticity.

Flag for bunch particles (1->protons 2->positrons 3,4->ions):	2
Number of particles per bunch:	4.1e+09
Machine:	DR
Observation points:	NONE
Interaction points:	NONE
Custom impedance:	BB
Bunch length (rms value) [m]:	0.0018
Normalized horizontal emittance (rms value) [um]:	0.456
Normalized vertical emittance (rms value) [um]:	0.0048
Longitudinal momentum spread:	0.001074
Synchrotron tune:	0.00578
Relativistic gamma:	5597.
Number of turns:	20000
Horizontal semiaxis of beam pipe [m]	0.031
Vertical semiaxis of beam pipe [m]	0.021
Longitudinal extension of the bunch (+/-N*sigma z)	2.
Horizontal tune:	48.35
Vertical tune:	10.4
Horizontal chromaticity [Q'x]:	0.
Vertical chromaticity [Q'y]:	0.
Flag for synchrotron motion:	1
Number of macroparticles per bunch:	1000000
Number of bunches:	1
Number of slices in each bunch:	500
Spacing between consecutive bunches centroids	5

Appendix A. HEADTAIL simulations parameters for the CLIC DR

Switch for bunch table:	0
Switch for wake fields:	1
Number of turns for the wake:	1
Conductivity of the resistive wall [1/Ohm/m]:	0
Length of the resistive wall [m]:	0.
Switch for wake table:	0
Flag for the space charge:	0
Smoothing order for longitudinal space charge:	3
Switch for initial kick:	1
x-kick amplitude at t=0 [sigmas]:	1e-5
y-kick amplitude at t=0 [sigmas]:	1e-5
z-kick amplitude at t=0 [m]:	0.
Switch for amplitude detuning:	0
Linear coupling switch(1->on 0->off):	0
Linear coupling coefficient [1/m]:	0.0015
Average dispersion function in the ring [m]:	0.0
Sextupolar kick switch(1->on 0->off):	0
Sextupole strength [$1/m^2$]:	-0.254564
Dispersion at the sextupoles [m]:	2.24
Switch for losses (0->no losses 1->losses):	2
Second order horizontal chromaticity (Q_x''):	0.
Second order vertical chromaticity (Q_y''):	0.
Number of turns between two bunch shape acquisitions:	250
Start turn for bunch shape acquisitions	1
Last turn for bunch shape acquisitions	20000
Main rf voltage [V]:	5.1e06
Main rf harmonic number:	1465

A.2 Broad-band resonator model with positive chromaticity

CLIC DR parameters used in HEADTAIL simulations for a BBR and positive chromaticity.

Flag for bunch particles (1->protons 2->positrons 3,4->ions):	2
Number of particles per bunch:	4.1e+09
Machine:	DR
Observation points:	NONE
Interaction points:	NONE
Custom impedance:	BB
Bunch length (rms value) [m]:	0.0018
Normalized horizontal emittance (rms value) [μm]:	0.456
Normalized vertical emittance (rms value) [μm]:	0.0048
Longitudinal momentum spread:	0.001074
Synchrotron tune:	0.00578
Relativistic gamma:	5597.
Number of turns:	20000
Horizontal semiaxis of beam pipe [m]	0.031
Vertical semiaxis of beam pipe [m]	0.021
Longitudinal extension of the bunch (+/-N*sigma z)	2.
Horizontal tune:	48.35
Vertical tune:	10.4
Horizontal chromaticity [Q'x]:	0.87
Vertical chromaticity [Q'y]:	0.19
Flag for synchrotron motion:	1
Number of macroparticles per bunch:	1000000
Number of bunches:	1
Number of slices in each bunch:	500
Spacing between consecutive bunches centroids	5
Switch for bunch table:	0
Switch for wake fields:	1
Number of turns for the wake:	1
Conductivity of the resistive wall [1/Ohm/m]:	0
Length of the resistive wall [m]:	0.
Switch for wake table:	0
Flag for the space charge:	0
Smoothing order for longitudinal space charge:	3
Switch for initial kick:	1
x-kick amplitude at t=0 [sigmas]:	1e-5
y-kick amplitude at t=0 [sigmas]:	1e-5
z-kick amplitude at t=0 [m]:	0.
Switch for amplitude detuning:	0

Appendix A. HEADTAIL simulations parameters for the CLIC DR

Linear coupling switch(1->on 0->off):	0
Linear coupling coefficient [1/m]:	0.0015
Average dispersion function in the ring [m]:	0.0
Sextupolar kick switch(1->on 0->off):	0
Sextupole strength [$1/m^2$]:	-0.254564
Dispersion at the sextupoles [m]:	2.24
Switch for losses (0->no losses 1->losses):	2
Second order horizontal chromaticity (Q_x''):	0.
Second order vertical chromaticity (Q_y''):	0.
Number of turns between two bunch shape acquisitions:	250
Start turn for bunch shape acquisitions	1
Last turn for bunch shape acquisitions	20000
Main rf voltage [V]:	5.1e06
Main rf harmonic number:	1465

B ImpedanceWake2D parameters

B.1 Wigglers: 2 μm NEG coating on StSt chamber

Machine: DR

Relativistic Gamma: 5597.

Impedance Length in m: 1.

Number of upper layers in the chamber wall: 2

Layer 1 inner half gap in mm: 6.

Layer 1 DC resistivity (Ohm.m): 1e-6

Layer 1 relaxation time for resistivity (ps): 0.

Layer 1 real part of dielectric constant: 1

Layer 1 magnetic susceptibility: 0

Layer 1 relaxation frequency of permeability (MHz): Infinity

Layer 1 thickness in mm: 0.002

Layer 2 DC resistivity (Ohm.m): 6.9e-7

Layer 2 relaxation time for resistivity (ps): 0

Layer 2 real part of dielectric constant: 1

Layer 2 magnetic susceptibility: 0

Layer 2 relaxation frequency of permeability (MHz): Infinity

Layer 2 thickness in mm: Infinity

Top bottom symmetry (yes or no): yes

start frequency exponent in Hz: 0

stop frequency exponent in Hz: 13

linear (1) or logarithmic (0) or both (2) frequency scan: 0

sampling frequency exponent in Hz (for linear): 8

Number of points per decade (for log): 20

when both, fmin of the refinement (in THz): 5.5

when both, fmax of the refinement (in THz): 7

when both, number of points in the refinement: 100

B.2 Arcs: 2 μm NEG coating on StSt chamber

Machine: DR
Relativistic Gamma: 5597.
Impedance Length in m: 1.
Number of layers: 2
Layer 1 inner radius in mm: 9.
Layer 1 DC resistivity (Ohm.m): 1e-6
Layer 1 relaxation time for resistivity (ps): 0.
Layer 1 real part of dielectric constant: 1
Layer 1 magnetic susceptibility: 0
Layer 1 relaxation frequency of permeability (MHz): Infinity
Layer 1 thickness in mm: 0.002
Layer 2 DC resistivity (Ohm.m): 6.9e-7
Layer 2 relaxation time for resistivity (ps): 0
Layer 2 real part of dielectric constant: 1
Layer 2 magnetic susceptibility: 0
Layer 2 relaxation frequency of permeability (MHz): Infinity
Layer 2 thickness in mm: Infinity
linear (1) or logarithmic (0) or both (2) frequency scan: 1
sampling distance in m for the linear sampling: 0.5e-5
zmin in m of the linear sampling: 0.5e-5
zmax in m of the linear sampling: 1.0
Number of points per decade for the logarithmic sampling: 100
exponent of zmin of the logarithmic sampling: -2
exponent of zmax of the logarithmic sampling: 6
Yokoya factors long, xdip, ydip, xquad, yquad: 1 1 1 0 0
factor weighting the longitudinal impedance error: 1.
tolerance (in wake units to achieve): 1.e13
frequency above which the mesh bisecting is linear [Hz]: 1.e11

B.3 Rest: 2 μm NEG coating on StSt chamber

Machine: DR
Relativistic Gamma: 5597.
Impedance Length in m: 1.
Number of layers: 2
Layer 1 inner radius in mm: 9.
Layer 1 DC resistivity (Ohm.m): 1e-6
Layer 1 relaxation time for resistivity (ps): 0.
Layer 1 real part of dielectric constant: 1

B.4. Wigglers: 1 μm or 2 μm NEG coating on StSt chamber

Layer 1 magnetic susceptibility: 0
Layer 1 relaxation frequency of permeability (MHz): Infinity
Layer 1 thickness in mm: 0.002
Layer 2 DC resistivity (Ohm.m): 6.9e-7
Layer 2 relaxation time for resistivity (ps): 0
Layer 2 real part of dielectric constant: 1
Layer 2 magnetic susceptibility: 0
Layer 2 relaxation frequency of permeability (MHz): Infinity
Layer 2 thickness in mm: Infinity
linear (1) or logarithmic (0) or both (2) frequency scan: 1
sampling distance in m for the linear sampling: 0.5e-5
zmin in m of the linear sampling: 0.5e-5
zmax in m of the linear sampling: 1.0
Number of points per decade for the logarithmic sampling: 100
exponent of zmin of the logarithmic sampling: -2
exponent of zmax of the logarithmic sampling: 6
Yokoya factors long, xdip, ydip, xquad, yquad: 1 1 1 0 0
factor weighting the longitudinal impedance error: 1.
tolerance (in wake units to achieve): 1.e13
frequency above which the mesh bisecting is linear [Hz]: 1.e11

B.4 Wigglers: 1 μm or 2 μm NEG coating on StSt chamber

Machine: DR
Relativistic Gamma: 5597.
Impedance Length in m: 1.
Number of upper layers in the chamber wall: 2
Layer 1 inner half gap in mm: 6.
Layer 1 DC resistivity (Ohm.m): 1e-6
Layer 1 relaxation time for resistivity (ps): 0.
Layer 1 real part of dielectric constant: 1
Layer 1 magnetic susceptibility: 0
Layer 1 relaxation frequency of permeability (MHz): Infinity
Layer 1 thickness in mm: 0.001 (or 0.002)
Layer 2 DC resistivity (Ohm.m): 6.9e-7
Layer 2 relaxation time for resistivity (ps): 0
Layer 2 real part of dielectric constant: 1
Layer 2 magnetic susceptibility: 0
Layer 2 relaxation frequency of permeability (MHz): Infinity
Layer 2 thickness in mm: Infinity

Appendix B. ImpedanceWake2D parameters

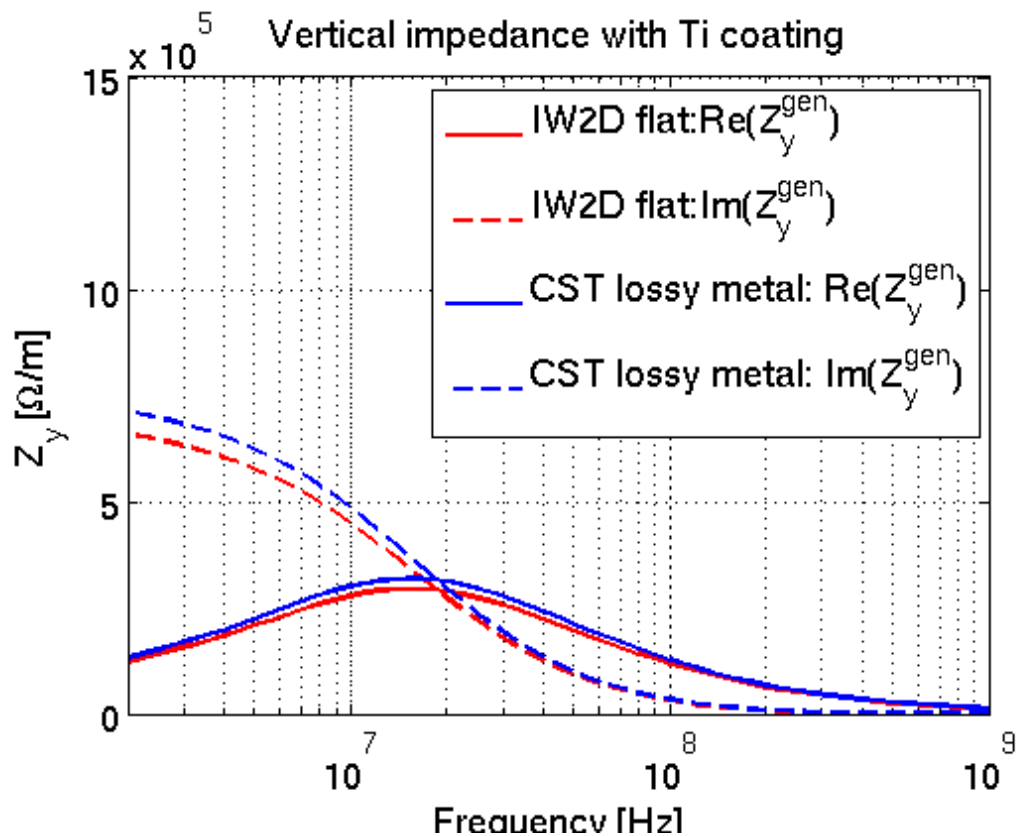
Top bottom symmetry (yes or no): yes
start frequency exponent in Hz: 0
stop frequency exponent in Hz: 13
linear (1) or logarithmic (0) or both (2) frequency scan: 0
sampling frequency exponent in Hz (for linear): 8
Number of points per decade (for log): 20
when both, fmin of the refinement (in THz): 5.5
when both, fmax of the refinement (in THz): 7
when both, number of points in the refinement: 100

B.5 Wigglers: 0.5 μm or 1 μm aC coating on StSt chamber

Machine: DR
Relativistic Gamma: 5597.
Impedance Length in m: 1.
Number of upper layers in the chamber wall: 2
Layer 1 inner half gap in mm: 6.
Layer 1 DC resistivity (Ohm.m): 6e-4
Layer 1 relaxation time for resistivity (ps): 0.
Layer 1 real part of dielectric constant: 1
Layer 1 magnetic susceptibility: 0
Layer 1 relaxation frequency of permeability (MHz): Infinity
Layer 1 thickness in mm: 0.0005 (or 0.001)
Layer 2 DC resistivity (Ohm.m): 6.9e-7
Layer 2 relaxation time for resistivity (ps): 0
Layer 2 real part of dielectric constant: 1
Layer 2 magnetic susceptibility: 0
Layer 2 relaxation frequency of permeability (MHz): Infinity
Layer 2 thickness in mm: Infinity
Top bottom symmetry (yes or no): yes
start frequency exponent in Hz: 0
stop frequency exponent in Hz: 13
linear (1) or logarithmic (0) or both (2) frequency scan: 0
sampling frequency exponent in Hz (for linear): 8
Number of points per decade (for log): 20
when both, fmin of the refinement (in THz): 5.5
when both, fmax of the refinement (in THz): 7
when both, number of points in the refinement: 100

C CST and ImpedanceWake2D comparison

C.1 Compare coating feature for a lossy substrate



Comparison of the generalized impedance for a flat multilayer structure with CST (blue) and ImpedanceWake2D (red). A lossy metal is used as a substrate material (Cu) and a Ti coating of $0.4 \mu\text{m}$ is considered. A good agreement between the codes is found, indicating that the lossy metal coating feature works properly when the required conditions are fulfilled.

D Simulations parameters for SLS2

D.1 Resistive wall impedance calculation of SLS2 with Impedance-Wake2D

Resistive wall calculation for SLS2: input file for ImpedanceWake2D.

Number of layers:	2
Layer 1 inner radius in mm:	10
Layer 1 DC resistivity (Ohm.m):	9.1e-7
Layer 1 relaxation time for resistivity (ps):	0
Layer 1 real part of dielectric constant:	1
Layer 1 magnetic susceptibility:	0
Layer 1 relaxation frequency of permeability (MHz):	Infinity
Layer 1 thickness in mm:	0.001
Layer 2 DC resistivity (Ohm.m):	1.68e-8
Layer 2 relaxation time for resistivity (ps):	0
Layer 2 real part of dielectric constant:	1
Layer 2 magnetic susceptibility:	0
Layer 2 relaxation frequency of permeability (MHz):	Infinity
Layer 2 thickness in mm:	Infinity

Bibliography

- [1] S. Glashow. *Partial symmetries of weak interactions*. Nucl.Phys., 22:579-588, 1961.
- [2] S. Weinberg. *A Model of Leptons*. Phys.Rev.Lett., 19:1264-1266, 1967.
- [3] A. Salam. *Weak and electromagnetic interactions*. In *Elementary particle theory*, 367-377. Almquist & Wiksell, 1968.
- [4] Georges Aad et al. *Observation of a new particle in the search for the Standard Model Higgs boson with the ATLAS detector at the LHC*. Phys.Rev.Lett., B716:1-29, 2012.
- [5] N. Toge, N. Walker and N. Phinney. *ILC Reference Design Report*. Vol.3, 2007.
- [6] P. Lebrun, L. Linssen, A. Lucaci-Timoce, D. Schulte, F. Simon, S. Stapnes, N. Toge, H. Weerts and J. Wells. *The CLIC program: Towards a staged e^+e^- linear collider exploring the terascale. CLIC conceptual design report*. CERN-2012-005, Geneva, 2012.
- [7] N. Leros, D. Schulte. CERN/PS 2001-029 (AE), Proceedings of PAC2001.
- [8] Y. Papaphilippou et al. *Conceptual design of the CLIC damping rings*. TUPPCO86, Proceedings of IPAC2012, New Orleans, Louisiana, USA.
- [9] <http://vadiodes.com/VDI/pdf/waveguidechart200908.pdf>
- [10] H. Wiedemann. *Particle Accelerator Physics*. Springer, Third Edition, 2007.
- [11] S.Y. Lee. *Accelerator Physics* (2nd Edition). World Scientific, 2004.
- [12] <http://www.cst.com>
- [13] K. Wille. *The Physics of Particle Accelerators*. Oxford.
- [14] <http://twiki.cern.ch/twiki/bin/view/CLIC/DampingRings>
- [15] S. Heifets, A. Wagner and B. Zotter. *Generalized impedances and wakes in asymmetric structures*. SLAC/AP110, 1998.

Bibliography

- [16] C. Zannini. *Electromagnetic Simulation of CERN Accelerator Components and Experimental Applications*. CERN-THESIS-2013-076.
- [17] B. W. Zotter. *The effective coupling impedance for instabilities of Gaussian bunches*. CERN-ISR-TH-80-03, 1980.
- [18] B. W. Zotter. *The effective coupling impedance for bunched beam instabilities*. CERNISR-TH-78-16, 1978.
- [19] A. W. Chao. *Physics of collective beam instabilities in high energy accelerators*. New York: Wiley, 1993.
- [20] N. Mounet. *ImpedanceWake2D manual*.
http://impedance.web.cern.ch/impedance/Codes/ImpedanceWake2D/user_manual_todate.txt
- [21] E. Métral, B. Zotter, and B. Salvant. *Resistive-wall impedance of an infinitely long multi-layer cylindrical beam pipe*. 22nd Particle Accelerator Conference, Albuquerque, USA, pages 4216–4218, 2007.
- [22] B. Zotter. *Transverse oscillations of a relativistic particle beam in a laminated vacuum chamber, 1969*. Report No. CERN-69-15.
- [23] B. Zotter. *Longitudinal instabilities of charged particle beams inside cylindrical walls of finite thickness*. Part. Accel., 1:311–326, 1970.
- [24] B. Zotter. *New results on the impedance of resistive metal walls of finite thickness, 2005*. Report No. CERN-AB-2005-043.
- [25] E. Keil and B. Zotter. *The impedance of layered vacuum chambers*. In 6th European Particle Accelerator Conference, Stockholm, Sweden, pages 963–965, 1998.
- [26] N. Mounet and E. Métral. *Electromagnetic fields created by a macroparticle in an infinitely long and axisymmetric multilayer beam pipe, 2009*. Report No. CERN-BE-2009-039.
- [27] N. Mounet. *The LHC Transverse Coupled-Bunch Instability*. CERN-THESIS-2012-055.
- [28] G. Rumolo and F. Zimmermann. *Practical User Guide for HEADTAIL*. CERN-SL-Note-2002-036 (2002).
- [29] B. Zotter and S. Kheifets. *Impedances and Wakes in High-Energy Particle Accelerators*. World Scientific.
- [30] E. Métral. *Wake fields and impedances*. USPAS 2009, Course on Collective Effects in Beam Dynamics for Particle Accelerators, Albuquerque, NewMexico, USA.
<http://impedance.web.cern.ch/impedance/USPAS/WakeFieldsAndImpedances.pdf>

-
- [31] E. Koukovini-Platia, K. Li, N. Mounet, G. Rumolo and B. Salvant. *Impedance effects in the CLIC Damping Rings*. TUPC050, IPAC 2011, San Sebastian, Spain.
- [32] CLIC DR collaboration page.
<http://twiki.cern.ch/twiki/bin/view/CLIC/DampingRings>
- [33] Y. Papaphilippou, H.H. Braun and M. Korostelev. *Parameter scan for the CLIC Damping Rings*. MOPP060, Proceedings of EPAC08, Genoa, Italy.
- [34] A. Grudiev. *Conceptual Design of the CLIC Damping Ring RF System*. TUPPR026, Proceedings of IPAC2012, New Orleans, Louisiana, USA.
- [35] B. Zotter. *Transverse Mode Coupling and Head-Tail Turbulence*. CERN/ISR-TH/82-10 (1982).
- [36] G. Rumolo et al. *Collective effects in the CLIC damping rings and transfer line*. CLIC Workshop, 15 October 2008.
- [37] R. Bartolini, L.H.A. Leunissen, Y. Papaphilippou, F. Schmidt, and A. Verdier. *Measurement of resonance driving terms from turn-by-turn data*. CERN-SL-Note-98-017-AP (1998).
- [38] R. Bartolini and F. Schmidt. *Normal form via tracking or beam data*. Part. Accel. 59 (1998) 93-106. CERN-LHC-PROJECT-REPORT-132.
- [39] J. Laskar. *Frequency analysis for multi-dimensional systems, global dynamics and diffusion*. Physica D 67 257-281, 1993.
- [40] F. Roncarolo, F. Caspers, T. Kroyer, E. Métral, N. Mounet, B. Salvant and B. Zotter. *Comparison between laboratory measurements, simulations and analytical predictions of the transverse wall impedance at low frequencies*. Phys. Rev. ST Accel. Beams, 12(084401), 2009.
- [41] N. Mounet and E. Métral. *The six electromagnetic field components at low frequency in an axisymmetric infinitely thick single-layer resistive beam pipe*. IPAC, Kyoto, Japan, 2010.
- [42] J. D. Jackson. *Classical Electrodynamics*. JohnWiley and Sons, 3rd edition, 1998.
- [43] S. Calatroni, P. Chiggiato, P. Costa Pinto, D. Hynds, M. Taborelli and C. Yin Vallgren. *Amorphous-carbon thin films for the mitigation of electron clouds in particle accelerators*. Final CARE-HHH Workshop on Scenarios for the LHC Upgrade and FAIR, HHH 2008 proceedings, Chavannes-de-Bogis, Switzerland.
- [44] C. Yin Vallgren et al. *Amorphous carbon coatings for mitigation of electron cloud in the CERN SPS*. TUPD048, IPAC 2010, Kyoto, Japan.

Bibliography

- [45] C. Yin Vallgren et al. *Low secondary electron yield carbon coatings for electron cloud mitigation in modern particle accelerators*. CERN-THESIS-2011-063.
- [46] P. Manini, A. Bonucci, A. Conte and S. Raimondi. *Deposition of Non Evaporable Getter (NEG) Films on Vacuum Chambers for High Energy Machines and Synchrotron Radiation Sources*. TUPCH178, Proceedings of EPAC 2006, Edinburgh, Scotland.
- [47] F. Antoniou. *Optics design of Intrabeam Scattering dominated damping rings*. CERN-THESIS-2012-368 CLIC-Note-989.
- [48] D. Schoerling et al. *Design and system integration of the superconducting wiggler magnets for the Compact Linear Collider damping rings*. PHYSICAL REVIEW SPECIAL TOPICS - ACCELERATORS AND BEAMS 15, 042401, 2012. DOI: 10.1103/PhysRevSTAB.15.042401
- [49] Y. Papaphilippou. *CLIC Damping Ring Beam Transfer Systems*. 2010.
- [50] M. J. Barnes, L. Ducimetière, J. Uythoven. *CLIC Pre-Damping and Damping Ring Kickers: Initial Ideas to Achieve Stability Requirements*. WEPD089, Proceeding of IPAC 2010, Kyoto, Japan.
- [51] J. Holma, M. Barnes, C. Belver-Aguilar, A. Faus-Golfe, F. Toral. *Present status of development of damping ring extraction kicker system for CLIC*.
- [52] C. Belver-Aguilar, A. Faus-Golfe, M.J. Barnes, G. Rumolo, C. Zannini, F. Toral. *Striplines for CLIC Pre-Damping and Damping Rings*. TUPC011, Proceedings of IPAC2011, Spain.
- [53] C. Belver-Aguilar et al. *Final Cross-section Design of the Stripline Kicker for the CLIC Damping Rings*. TUPPR016, Proceedings of IPAC2012, USA, May 2012.
- [54] C. Belver-Aguilar et al. *Design Study of the Striplines for the Extraction Kicker of the CLIC Damping Rings*. MOPA01, IBIC'12, Japan, October 2012.
- [55] C. Belver-Aguilar, A. Faus-Golfe, M.J. Barnes, F. Toral, J. Gómez, D. Gutiérrez. *Design and manufacturing description of the prototype striplines for the extraction kicker of the CLIC damping rings*. MOPWO022, Proceedings of IPAC2013, Shanghai, China.
- [56] N. Bundaleski, S. Candeias, A. Santos, O. M. N. D. Teodoro and A. G. Silva. *Study of SEY degradation of amorphous carbon coatings*. DOI: 10.5170/CERN-2013-002.149.
- [57] A. Hershcovitch et al. *Recent RHIC in-situ coating technology developments*. DOI: 10.5170/CERN-2013-002.251.

- [58] Y. Vallgren et al. *Performance of Carbon Coatings for Mitigation of Electron Cloud in the SPS*. TUPS028, IPAC 2011, San Sebastian, Spain.
- [59] Y. Vallgren, P. Chiggiato, P. Costa Pinto, H. Neupert, G. Rumolo, E. Shaposhnikova, M. Taborelli and S. Kato. *Characterization of Carbon Coatings with Low Secondary Electron Yield*. TUPS027, IPAC 2011, San Sebastian, Spain.
- [60] C. Benvenuti, P. Chiggiato, P. Costa Pinto, A. Escudeiro Santana, T. Hedley, A. Mongelluzzo, V. Ruzinov and I. Wevers. *Vacuum properties of TiZrV non-evaporable getter films*. CERN EST/99-007.
- [61] P. Costa Pinto. *NEG coating of the non-standard LSS vacuum chambers*. CERN TS-Note-2005-030.
- [62] E. Maxwell. *Conductivity of metallic surfaces at microwave frequencies*. Journal of Applied Physics, Vol. 18, No. 7, 629-638, July, 1947.
- [63] W. Kruppa. *An explicit solution for the scattering parameters of a linear two-port measured with an imperfect test set*. IEEE Trans. On Micr. Theory and Tech., vol. 19.
- [64] <http://www.agilent.com>
- [65] J. Ph. Rigaud. *Metrology report of surface roughness on a stainless steel waveguide*. CERN EDMS report, 1338969.
- [66] N. Narayana Rao. *Elements of Engineering Electromagnetics*. Fourth Edition, 1994.
- [67] <http://www.microwaves101.com/encyclopedias/676-rectangular-waveguide-dimensions>
- [68] Waveguide Loss. <http://www.microwaves101.com/encyclopedia/waveguideloss.cfm>
- [69] J. Ph. Rigaud. *Metrology report of surface roughness on a copper waveguide*. CERN EDMS report, 1338969.
- [70] E. Koukovini-Platia, G. De Michele, C. Zannini and G. Rumolo. *Electromagnetic characterization of materials for the CLIC damping rings*. ICAP, Warnemünde, Germany, 2012.
- [71] <http://vadiodes.com>
- [72] <http://www.cells.es/en/>
- [73] U. Iriso, F. Pérez, A. Salom. *Tune measurement system at the ALBA Booster*. TUPSM073, Proceedings of BIW10, New Mexico, US.

Bibliography

- [74] U. Iriso, M. Álvarez, F. Fernández, F. Pérez, A. Olmos. *Diagnostics during the ALBA storage ring commissioning*. TUOA02, Proceedings of DIPAC2011, Hamburg, Germany.
- [75] T. F. Günzel, U. Iriso, F. Pérez, E. Koukovini-Platia, G. Rumolo. *Analysis of single bunch measurements at the ALBA storage ring*. TUPRI052, Proceedings IPAC 2014, Dresden, Germany.
- [76] U. Iriso, L. Torino, T. Mitsuhashi. *First Transverse Beam Size Measurements Using Interferometry at ALBA*. MOPF01, Proceedings of IBIC2013, Oxford, UK.
- [77] U. Iriso, et al. *Diagnostics during the ALBA SR commissioning*. Proceedings of DIPAC'11, Hamburg, Germany.
- [78] U. Iriso and F. Fernandez. *Streak Camera Measurements at ALBA: Bunch Length and Energy Matching*. Proceedings of IBIC'2012, Tsukuba, Japan.
- [79] Y. Cai et al. *Potential-well distortion, microwave instability, and their effects with colliding beams at KEKB*. Physical Review Special Topics, Accelerators and Beams 12, 0601002, 2009.
- [80] G. Rumolo et E. Métral. *Collective effects in the longitudinal plane*. USPAS course on Collective Effects, 2009.
- [81] T. F. Günzel, F. Pérez. *Impedance and instabilities for the ALBA storage ring*. EPAC2008, p.1622.
- [82] T. F. Günzel. *Transverse instabilities studies at the ALBA Storage Ring*. IPAC2011, p.751.
- [83] M. Pont, R. Nunez, E. Huttel. *Septum and kicker magnets for the ALBA booster and storage ring*. WEPO013, Proceedings of IPAC 2011, San Sebastián, Spain.
- [84] G. Benedetti, D. Einfeld, E. Huttel, M. Muñoz, M. Pont, E. Huttel. *Injection into the ALBA storage ring*. WEPC068, Proceedings of EPAC08, Genoa, Italy.
- [85] L. Palumbo, V.G. Vaccaro, M. Zobov. *Wake Fields and Impedance*. CAS Advances School on Accelerator Physics. Rhodes, Greece, Sept. 1994.
- [86] M. Zobov et al. *DAΦNE operation and plans for DAΦNE2*. SLAC-PUB-11655.
- [87] A. Sargsyan, K. Manukyan. *A method of beam energy spread and synchrotron tune measurement based on decoherence signal analysis*. THPE056, Proceedings of IPAC10, Kyoto, Japan.
- [88] Ian C. Hsu. *The decoherence and recoherence of the betatron oscillation signal and an application*. Particle Accelerators, 1990, Vol.34, pp. 43-52.

Curriculum Vitae

EIRINI KOUKOVINI-PLATIA

Address: Rue de Geneve 43, 01630, Saint Genis Pouilly, France
Mobile Phone: +41 76 27 68 265
Email: eirini.koukovini.platia@cern.ch

Current Position

2011 – present: Ph.D. student at the Swiss Federal Institute of Technology, EPFL, and CERN. Thesis title: “High Frequency Effects of Impedances and Coatings in the CLIC Damping Rings” under the joint supervision of Prof. Leonid Rivkin from EPFL and Dr. Giovanni Rumolo from CERN.

Education/Training/Tutoring

- **September 2013 - January 2014:** Teaching Assistant of Prof. Leonid Rivkin for the EPFL master course “Introduction to Accelerator Physics”.
- **2011 - present:** Trained guide for CERN visitors.
- **June 2010 - July 2011:** CERN Technical Student Program. Study of collective effects for the Compact Linear Collider (CLIC) damping rings and especially wake fields and impedances in case of different coatings in the wigglers and the vacuum pipe.
- **2009:** 6-month master thesis at the B-Physics group at CERN. Study of the meson decay $\chi_{b0} \rightarrow J/\psi + J/\psi \rightarrow \mu^+ \mu^- \mu^+ \mu^-$ and searches of the background in the ATLAS detector.
- **June 2008 - August 2008:** CERN Summer Student Program. Joined the B-Physics group of ATLAS. Study of the meson decay $\chi_{b0} \rightarrow J/\psi + J/\psi \rightarrow \mu^+ \mu^- \mu^+ \mu^-$.
- **November 2007 - December 2007:** Practical training at the Institut Laue-Langevin (ILL), Grenoble. Measurement of the residual stresses in a steel laser weld and plates of ferritic steel, using neutron beam. The project was included in the annual report 2008 of the ILL, amongst the scientific highlights.
- **September 2003 - March 2010:** Diploma and Master of the School of Applied Mathematical and Physical Sciences, National Technical University of Athens. Specialized courses in: Nuclear and Elementary Particle Physics, Physics of Materials, Optoelectronics and Lasers. Grade: 7.82/10 - Very good.
- **September 2000 – September 2003:** High school of Othisi, Athens. Grade: 18.8/20 – Excellent.

Courses Attended

- **June 2013:** U.S. Particle Accelerator School (USPAS). Colorado State University, Colorado. Courses on Design of Electron Storage and Damping Rings and Linear Accelerator Design for Free Electron Lasers.
- **January 2013:** USPAS. Duke University, Durham, North Carolina. Course on Accelerator Physics.

- **September 2011:** CERN Accelerator School (CAS), intermediate level. Chios, Greece.
- **February 2011:** Two-week participation in the Join Universities Accelerator School (JUAS). Archamps, France.

Computer Skills

- Operating systems: Windows, Linux.
- Java, C++, Python, Bash shell.
- Mathematica, Matlab, ROOT, LaTeX.

Language Skills

- Certificate of Proficiency in English, the University of Michigan.
- Diplome d'etudes en langue Francaise, B2.
- Greek, native language.

Conferences & Workshops Talks

- “Study of the decay $\chi_{b0} \rightarrow J/\psi + J/\psi \rightarrow \mu^+ \mu^- \mu^+ \mu^-$ in the ATLAS detector”. Annual workshop 2009, Greek HEP Society, NCRS “Demokritos”. Athens, May 2009.
- “Collective instabilities simulations for the CLIC damping rings”. International Workshop on Linear Colliders. Geneva, October 2010.
- “Impedance budget and effect of chamber coating on CLIC Damping Ring beam stability”. Low Emittance Rings Workshop (LowERing2011). Crete, October 2011.
- “Electromagnetic characterization of materials for the CLIC Damping Rings and high frequency issues”. 11th International Computational Accelerator Physics Conference (ICAP). Rostock-Warnemünde, August 2012.
- “Impedance budget and effect of chamber coating on CLIC Damping Rings beam stability”. LCWS workshop, Texas, October 2012 and the CLIC workshop, CERN, Geneva, January 2013.
- “Impedance budget and effect of chamber coating on CLIC Damping Rings beam stability”. ECFA Linear Collider Workshop. Hamburg, May 2013.
- “Effect of impedance and coatings in the CLIC damping rings”. 3rd Low Emittance Ring workshop (LER2013). Oxford, July 2013.
- “High frequency effects of impedance and coatings in the CLIC Damping Rings”. TWIICE workshop at SOLEIL. Paris, January 2014.

List of Publications

Articles

- D.J. Hughes, E. Koukovini-Platia, E.L.Heeley. “Residual stress in a laser welded EUROFER blanket module assembly using non-destructive neutron diffraction techniques”. Elsevier, Fusion Engineering and Design, Volume 89, Issue 2, February 2014, Pages 104–108. doi:10.1016/j.fusengdes.2013.12.041.

Conference Proceedings

- G. Rumolo et al. "Electron cloud observation in the LHC". IPAC 2011, San Sebastian, Spain.
- E. Koukovini Platia, K. Li, N. Mounet, G. Rumolo and B. Salvant. "Impedance effects in the CLIC damping rings". IPAC 2011, San Sebastian, Spain.
- Y. Papaphilippou et al. "Conceptual Design of the CLIC damping rings". IPAC 2012, New Orleans, Louisiana, USA.
- E. Koukovini Platia, G. De Michele, C. Zannini and G. Rumolo. "Electromagnetic characterization of materials for the CLIC damping rings". 11th International Computational Accelerator Physics (ICAP) conference 2012, Rostock- Warnemünde, Germany.
- E. Koukovini-Platia and G. Rumolo. "Review of the Transverse Impedance Budget for the CLIC Damping Rings". IPAC 2014, Dresden, Germany.
- E. Koukovini-Platia, G. De Michele, G. Rumolo, C. Zannini. "High Frequency Electromagnetic Characterization of NEG properties for the CLIC Damping Rings". IPAC 2014, Dresden, Germany.
- T.F. Günzel, U.Iriso, E. Koukovini-Platia, G. Rumolo. "Analysis of single bunch measurements at the ALBA storage ring". IPAC 2014, Dresden, Germany.
- E.Koukovini-Platia, G. Rumolo, C. Zannini. "Electromagnetic characterization of NEG properties above 200 GHz for the CLIC damping rings". IPAC 2015, Richmond, VA, USA.
- T.F. Günzel, H.Bartosik, U.Iriso, E. Koukovini-Platia, G. Rumolo. "Beam-based impedance characterization of the ALBA pinger magnet". IPAC 2015, Richmond, VA, USA.

Internal Reports

- "Managing weld distortions in thin steel plates". C. M. Davies, K. M. Nikbin, R. C. Wimpory, M. Beres, D. Dye, D. J. Hughes, E. Koukovini-Platia. ILL Annual Report 2008.
http://www.ill.eu/fileadmin/users_files/Annual_Report/AR-08/page/pg.htm?rub=3_6
- "High Frequency Studies for the CLIC Damping Rings". E. Koukovini-Platia, G. Rumolo
ICFA, Beam Dynamics Newsletter No.62.

Special Awards

- "Young scientist award". ICAP August 2012, Rostock- Warnemünde, Germany.
- "Low Emittance Rings prize". 3rd Low Emittance Ring Workshop, July 2013, Oxford.
- "School certificate of excellence". 1999-2000, yearly awarded.

Memberships

- B-physics group, ATLAS experiment, CERN.
- BE-ABP-LAT group, CERN.

Other Interests

- Diploma in piano and the theory of music.
- 2004 - 2006: Piano instructor, private lessons.
- 6-years of Latin dances. 2011 - 2013: Salsa instructor.
- Horse-riding.